NASA Contractor Report 185144

Precipitation Strengthened High Strength, High Conductivity Cu-Cr-Nb Alloys Produced by Chill Block Melt Spinning

David L. Ellis and Gary M. Michal
Case Western Reserve University
Cleveland, Ohio

September 1989

Prepared for
Lewis Research Center
Under Grant NGT-50087

National Aeronautics and
Space Administration

(NASA-CR-185144) PRECIPITATION STRENGTHENED N90-11853
HIGH STRENGTH, HIGH CONDUCTIVITY Cu-Cr-Nb
ALLOYS PRODUCED BY CHILL BLOCK MELT SPINNING
Final Report Ph.D. Thesis (Case Western Unclas
Reserve Univ.) 231 p CSCL 11F G3/26 0237060

PRECIPITATION STRENGTHENED HIGH STRENGTH, HIGH CONDUCTIVITY CU-CR-NB ALLOYS PRODUCED BY CHILL BLOCK MELT SPINNING

ABSTRACT

by

DAVID LESLIE ELLIS

There are many potential applications for materials that possess a combination of high strength, high conductivity, and good long term stability at elevated temperatures.

In an effort to achieve this combination of properties a series of Cu-based alloys containing 2 to 10 a/o Cr and 1 to 5 a/o Nb were produced by chill block melt spinning (CBMS). The melt spun ribbons were consolidated and hot rolled to sheet for testing. The desire was to produce a supersaturated Cu-Cr-Nb solid solution from which the high melting point intermetallic compound Cr_2Nb could be preferentially precipitated to precipitation strengthen the Cu matrix. By using the intermetallic phase, it was hoped that the precipitates would not coarsen readily and lose their strength as with Cu-Cr alloys do when exposed to elevated temperatures, particularly above 500°C.

The results show that the materials possess electrical conductivities in excess of 90% that of pure Cu at 200°C and above. This implies that the thermal conductivities of these alloys are near that of pure Cu at temperatures above 200°C.

The strengths of the Cu-Cr-Nb alloys were much greater than Cu, Cu-0.6 Cr, NARloy-A, and NARloy-Z in the as-melt spun condition. The strengths of the consolidated materials were less than Cu-Cr and Cu-Cr-Zr below 500°C and 600°C respectively, but were significantly better above these temperatures. The strengths of the consolidated materials were greater than conventional wrought NARloy-Z, the material currently used in rocket nozzles, at all temperatures. GLIDCOP possessed similar strength levels up to 750°C when the strength of the Cu-Cr-Nb alloys begins to degrade.

The long term stability of the Cu-Cr-Nb alloys was measured by the microhardness of aged samples and the growth of precipitates. The microhardness measurements indicate that the alloys overage rapidly, but do not suffer much loss in strength between 10 and 100 hours which confirms the results of the electrical resistivity measurements taken during the aging of the alloys at 500°C. The loss in strength from peak strength levels is significant, but the strength remains exceptionally good.

TEM of the as-melt spun samples revealed that the Cr_2Nb precipitates formed in the liquid Cu during the chill block melt spinning, indicating a very strong driving force for the formation of the precipitates. TEM of the aged and consolidated materials indicates that the precipitates do coarsen considerably, but remain in the submicron size range.

ACKNOWLEDGEMENTS

I would like to thank NASA Lewis Research Center for supporting my work through the NASA Graduate Student Fellowship Program. I would like to extend special thanks to Hugh Gray, Norman Orth, John King, Ivan Locci, Mohan Hebsur, Gordon Watson, James Knight, John Juhaus, David Hull, Todd Leonhardt, Robert Dreshfield, Ralph Garlick, David Plumer, Chuck Boros, Adrienne Veverka, Peggy Yancer, and Ted Bloom.

I would also like to thank Professors Mark DeGuire, John Lewandowski, and Robert Savinell for kindly consenting to sit on my committee. And finally a special thanks to my advisor Gary Michal for all of his help.

Table of Contents

1 Introduction

There are many potential applications for materials that combine high strength, high conductivity, and good microstructural and mechanical stability at elevated temperatures. They range from common applications such as resistance welding electrodes (1), lead wires (1,2), relay blades (1), contact supports (1), commutators (1), X-ray tube studs (2), and connectors (2) to exotic applications such as fusion reactor first walls (1), water-cooled gas turbine blades (3), and targets for neutron irradiation (4).

One application that is of particular interest to the National Aeronautics and Space Administration (NASA) is rocket nozzles for use in the space shuttle main engine and the new Orbital Transfer Vehicle (OTV) now under development. This craft will be used to ferry payloads in low earth orbit to geosynchronous orbit, retrieve old satellites, and service the space station. Missions will last many months with the OTV engines potentially firing hundreds of times. The primary considerations for the material from which the thrust chamber is made are the heat transfer and cycle life under the operating conditions of the OTV engine (5). Current materials used in similar rocket nozzles such as NARLoy-Z can fail after even a single mission (6). A better material is needed.

1.1 Outline of Problem

Figure 1 shows a typical rocket nozzle. The OTV engine produces 7,500 pounds of thrust (5). To generate this large thrust efficiently the engine burns a combination of liquid hydrogen and liquid oxygen. The combustion results in a chamber pressure of 1210 psia. Design conditions require that the thrust chamber has a life of at least 25 missions.

Heat transfer for materials used in the thrust chamber is important since the material is exposed to the rocket flame on one side and the liquid oxygen and liquid hydrogen flowing through cooling ducts on the other side. By transferring the heat from the rocket flame to the cryogenic propellents rapidly, the part is kept below the melting point of the material. If the part could not be cooled sufficiently through conduction of heat through the material, high melting point alloys such as molybdenum- and tungsten-based alloys would be required. These alloys have high densities which are not desirable for these types of applications since weight is a major concern.

Thermal fatigue of the material limits cycle life (6). By increasing the strength of the materials used for the rocket nozzles, the thermal fatigue resistance should be increased to an acceptable value.

Figure 1 - Rocket Nozzle

1.2 Purpose of Study

The purpose of this study is to produce a high strength, high conductivity material which has good long term microstructural and mechanical stability.

1.3 Alloy Selection

There are many problems associated with achieving the desired combination of properties. High strength at elevated temperatures can be achieved by a variety of materials such as γ' (Ni_3Al) strengthened nickel-based alloys (7). Cu, Au, Ag, and to a lesser extent Al have high conductivities (8). Unfortunately alloys of these elements which have the required high strengths have greatly reduced conductivities in most cases (9,10). A variety of materials such as oxide dispersion strengthened (ODS) alloys have good long term stability (1). The problems occur when one tries to combine all three in one material.

Some successes have occurred. Using Cu as a base metal, it is possible to develop dispersion strengthened or precipitation strengthened alloys that have significantly higher strengths than pure copper, retain much of this strength at elevated temperatures for long times, and still have more than 50% of the electrical and thermal conductivity of pure Cu (1).

Figure 2 taken from Shapiro and Crane (11) shows how the various strengthening mechanisms affect the tensile strength and electrical conductivity as measured against the International Annealed Copper Standard (IACS) for a variety of alloys. As can be seen, alloy systems that are solid solution strengthened have the worst combination of strength and conductivity. Dispersion strengthened alloys have a good combination of properties, but the best combination occurs for alloys that are precipitation strengthened when they are fully hardened. Based on this information, precipitation strengthening was selected for the strengthening mechanism.

The next decision was to determine the best precipitate to use to maximize strength and conductivity. A high melting point intermetallic was chosen for the precipitates based on the generally high strength of the intermetallics and the stability of the phases as evidenced by their high melting points. Since the conductivity of the alloys would be greatly decreased by solute atoms in solution, elements with minimal solid solubility in copper were explored.

Analysis of the available data showed that Cr and Nb have minimal solubility in solid copper and form an intermetallic compound Cr_2Nb which melts congruently at 1733°C (3151°F). These two elements also have complete solubility in liquid copper at temperatures above the liquidus temperature.

Rapid solidification technology (RST) was chosen in an attempt to increase the limits of solid solubility of Cr and Nb in solid Cu. The desire was to produce a supersaturated solid solution from which very fine Cr_2Nb particles could be precipitated with a subsequent thermal treatment. It was also known that RST would produce a fine microstructure with minimal segregation, an important consideration in these alloys. The fine grain size would also strengthen the alloys at temperatures where grain boundary sliding does not occur.

This combination of material properties and processing advantages led to the decision to use RST to produce precipitation strengthened Cu-Cr-Nb alloys.

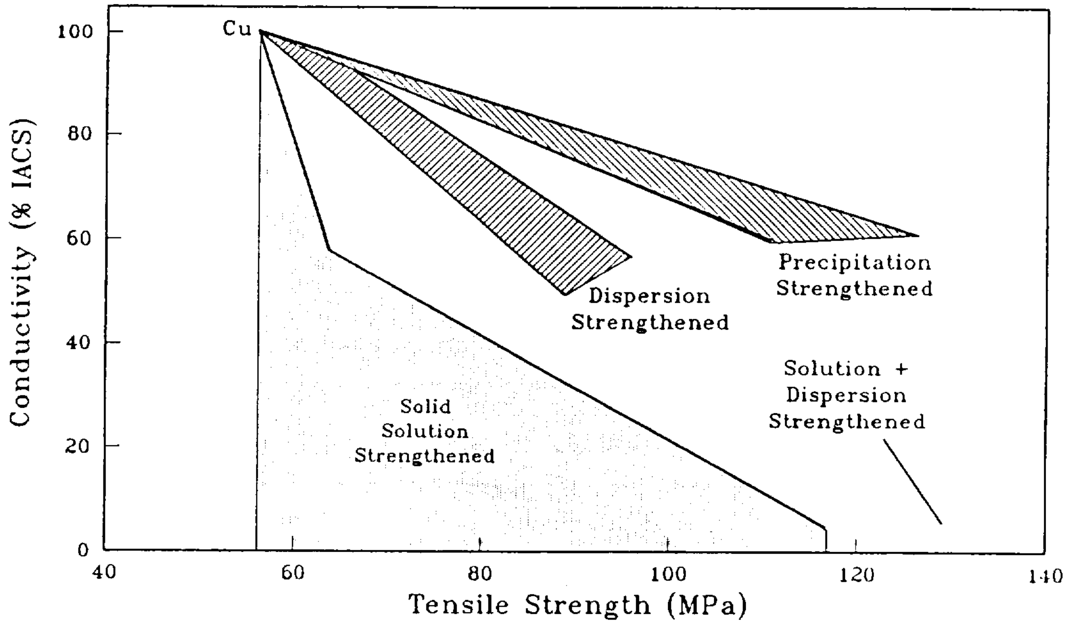

Figure 2 - Correlation of Electrical Conductivity and Tensile Strength for Various Strengthening Mechanisms in Cu-Based Alloys
From Shapiro and Crane (11)

2 Literature Review

Since the alloys examined are new materials, there is no literature available on the Cu-Cr-Nb alloy system. Instead a more general review of the various aspects of the study such as precipitation hardening, rapid solidification technology, electrical resistivity and thermal conductivity, and precipitation and growth of secondary phases will be presented. In addition, various relevant properties for other Cu-based alloys, particularly Cu-Cr and Cu-Nb alloys will be presented.

2.1 Phase Diagrams

No ternary phase diagram exists for the Cu-Cr-Nb system, but binary phase diagrams for the Cu-Cr, Cu-Nb, and Cr-Nb systems do exist. In addition there has been some work done on the substitution of Cu for Cr in Cr_2Ta. From these some suppositions can be drawn for the Cu-Cr_2Nb pseudo-binary phase diagram.

2.1.1 Cu-Cr Phase Diagram

The first mention of Cu-Cr alloys was by Guillet (12) in 1906 with Hindrichs presenting early information on the Cu-Cr binary phase diagram in 1908 (13). The first reference to mechanical properties found in the literature review was a paper by Hunter and Sebast (14) published in 1917.

The phase diagram originally showed a feature not accepted today. Figure 3 shows an example taken from Hensel and Larsen (15). This phase diagram shows an immiscibility gap in the liquid phase occurring between 43 a/o Cr and 95 a/o Cr above 1470°C (2678°F).

The currently accepted phase diagram proposed by Chakrabati and Laughlin (16) is shown in Figure 4. More recent work has established that there is no immiscibility gap in the liquid phase. The values for the eutectic and maximum solubility have also changed slightly. The primary reason for these changes is the higher purity of materials available to researchers today. Contaminants, primarily oxygen, have been dramatically reduced since the original work was done.

The Cu rich portion of the phase diagram shows that Cr has limited solubility in solid Cu but high solubility in liquid Cu. Maximum solubility of Cr in solid Cu is 0.85 a/o at the eutectic temperature. The solubility rapidly decreases with decreasing temperature below the eutectic temperature.

The phase diagram shows that hypereutectic alloys have a large difference in temperature between their solidus and liquidus. The value increases rapidly until a plateau is reached at approximately 25 a/o.

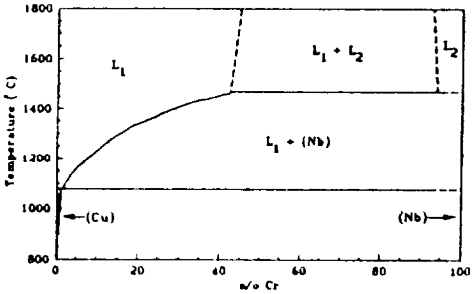

Figure 3a - Old Cu-Cr Phase Diagram
From Hensel and Larsen (15)

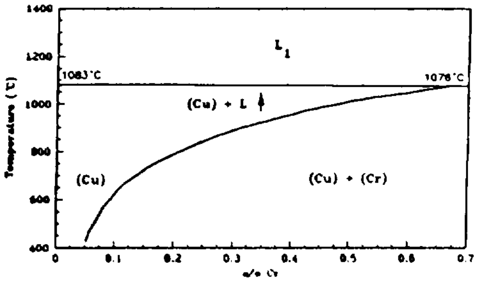

3b - Old Cu-Cr Phase Diagram, Detail of
Low Cr Region
From Hensel and Larsen (15)

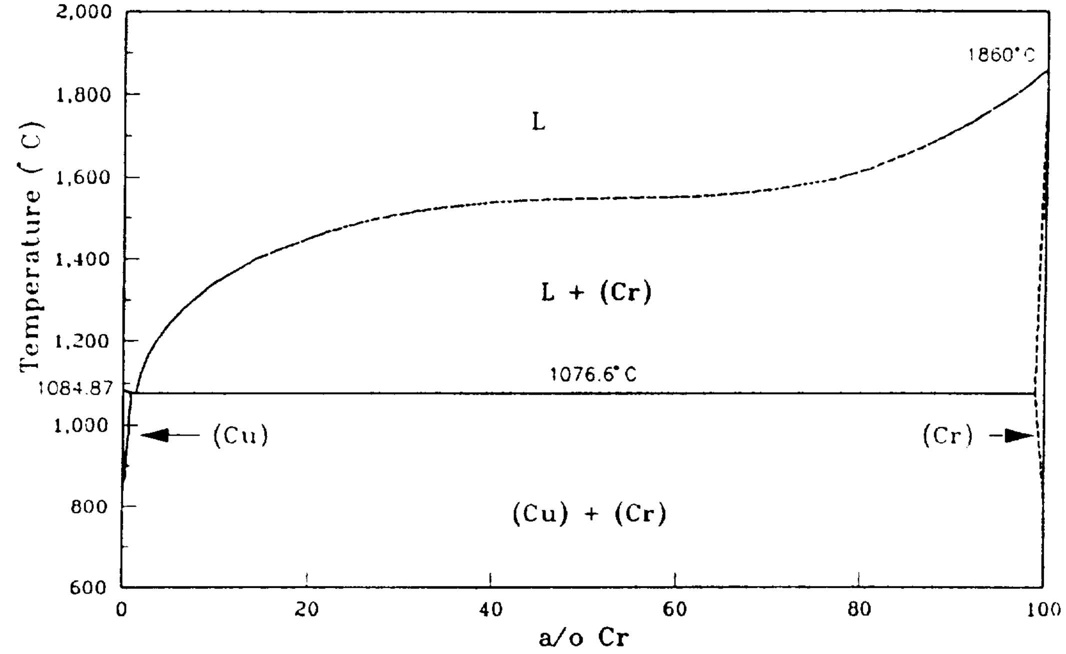

Figure 4 - Currently Accepted Cu-Cr Phase Diagram
From Chakrabati and Lauglin (16)

2.1.2 Cu-Nb Phase Diagram

The earliest reference found to the Cu-Nb phase diagram was a paper by Elliott (17) published in 1954. Examination of a material with the composition corresponding to Cu_2Nb after aging for 10 minutes at 800° C showed the presence of only FCC Cu and BCC Nb. From the segregated structure similar to a eutectic, the conclusion was made that the system was a simple eutectic.

The Cu-Nb phase diagram is very similar in shape to the Cu-Cr phase diagram. Like the Cu-Cr system, an immiscibility gap in the liquid phase was reported in the original phase diagram presented by Popov and Shiryaeva (18) as shown in Figure 5. Verhoeven and Gibson (19) showed that the immiscibility gap was a result of the use of alloys with high O contents. The oxygen was incorporated in the alloys through attack of the Al_2O_3 crucibles by the molten metal. Alloys cast in ZrO_2 and Y_2O_3 crucibles had much lower O contents and did not exhibit the spheroidal microstructure associated with the monotectic reaction and immiscibility gap.

Popov and Shiryaeva also showed a peritectic reaction at 1100°C for a liquid with 0.1 a/o Nb as depicted in Figure 6. Again, the high impurity content seems to be the cause of this peritectic reaction. More recent work by Petrensko, Tikhonovskii, Berdnik, Somov, Oleeksienko, and Arzhavitin (20) has produced the accepted eutectic reaction at 1080°C for liquid with 0.2 a/o Nb shown in Figure 6b.

The currently accepted phase diagram for the Cu-Nb system proposed by Chakrabati and Laughlin (21) is presented in Figure 7.

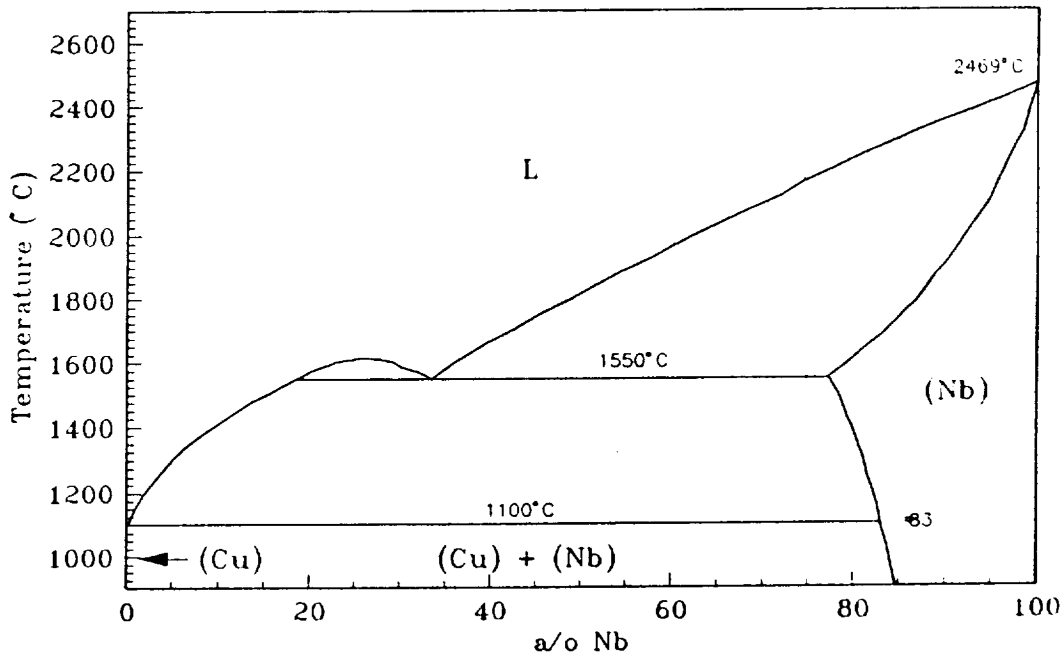

Figure 5 - Old Cu-Nb Phase Diagram From Popov and Shiryaeva (18)

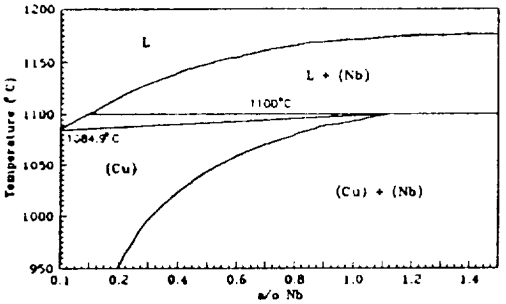

Figure 6a - Peritectic Reaction Proposed by Popov and Shiryaeva (18)

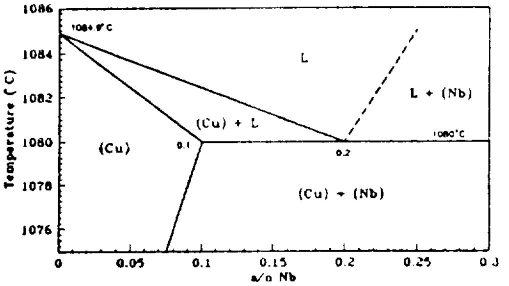

6b - Eutectic Reaction Proposed by Petrensko, Tikhonovskii, Berdnik, Somov, Oleeksienko, and Arzhavitin (20)

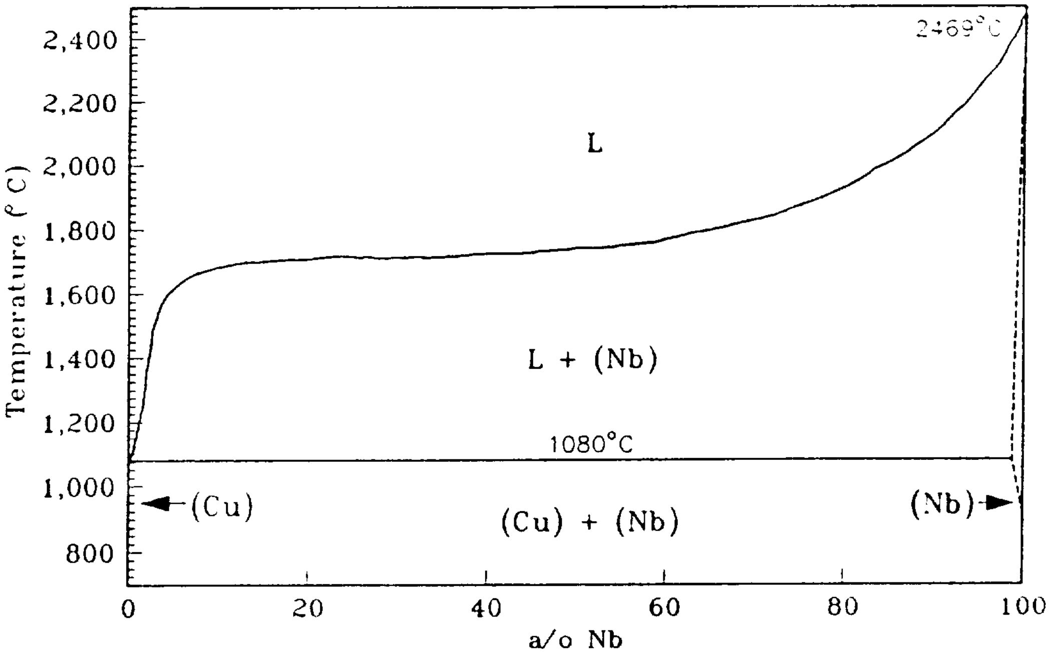

Figure 7 - Currently Accepted Cu-Nb Phase Diagram From Chakrabati and Laughlin (21)

2.1.3 Cr-Nb Phase Diagram

Like the Cu-Cr and Cu-Nb phase diagrams, the Cr-Nb phase diagram has undergone revision from the one originally proposed.

The early work on the Cr-Nb system such as that done by Kubaschewski and Schneider (22) indicated the existence of the intermetallic compound Cr_3Nb_2. The work, done with low purity alloys, also implied that the phase had a large range of stoichiometry. Later work by Eremko, Zudilova, and Gaevskaya (23) suggested that there was in fact only a single intermetallic compound, Cr_2Nb, and two eutectics as shown in the modified phase diagram proposed by Goldschidt and Brand (24) presented in Figure 8.

The intermetallic phase Cr_2Nb melts congruently at 1733°C (3151°F). Cr_2Nb undergoes a phase transformation below 1588°C (2890°F) from the high temperature hexagonal phase to the low temperature FCC phase. From the kinetics for the transformation of Cr_2Ta, the isomorphic intermetallic compound formed by Cr and Ta, observed by Duwez and Marten (25) and the great similarity between the Cr-Nb and Cr-Ta system, the transformation of Cr_2Nb from the hexagonal phase to the FCC phase is inferred to be sluggish. Results of this study confirm this inference.

Cr_2Nb has the *C14* or $MgZn_2$ structure above 1588°C (26). The lattice parameters for this hexagonal phase are $a_o = 0.488$ nm and $c_o = 0.794$ nm. The lower temperature phase has the FCC *C15* or $MgCu_2$ structure with a lattice parameter of $a_o = 0.699$ nm (25).

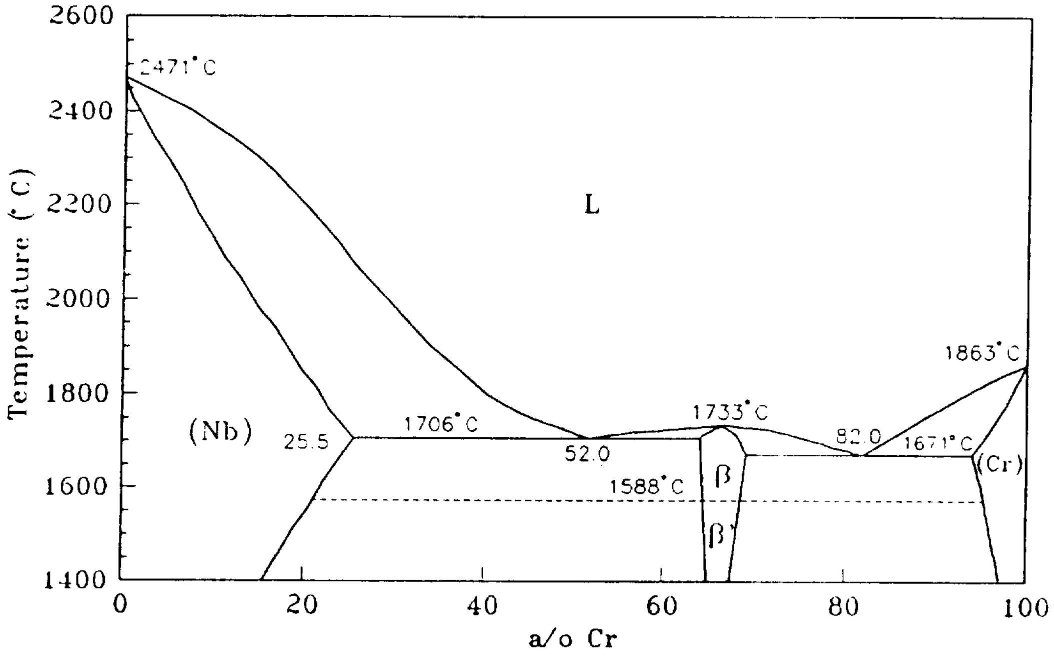

Figure 8 - Current Cr-Nb Phase Diagram
From Goldschidt and Brand (24)

2.1.4 Cu-Cr_2Nb Pseudo-Binary Phase Diagram

While there has been no work done on the complete Cu-Cr-Nb phase diagram, one study looked at the substitution of transition elements in ternary σ and Laves phases. The work done by Kuo (27) included the substitution of Cu for Cr in the Cr_2Ta Laves phase. The results indicated that Cu could substitute for the Cr in the Cr_2Ta up to at least the composition equivalent to the intermetallic phase $Cr_{3/2}Cu_{1/2}Ta$. Given the identical size of the Nb and Ta atoms, their similar electron shell configurations, and the observed similarities between the Cr-Nb and Cr-Ta systems, it is reasonable to assume that the Cr_2Nb can also accommodate considerable amounts of Cu in the Cr_2Nb.

Kuo's results from X-ray diffraction analysis of the samples allowed for the determination of the space groups and lattice parameters of the Cr_2Ta with and without Cu. The space groups and lattice parameters for Cr_2Ta and the

$Cr_{3/2}Cu_{1/2}Ta$ composition are identical. The observed structure types of the $Cr_{3/2}Cu_{1/2}Ta$, the high temperature hexagonal form of Cr_2Ta, and the high temperature hexagonal form of Cr_2Nb are all *C14* or $MgZn_2$ structures.

No data was given for melting point or phase transformations of the ternary alloys.

2.2 Precipitation and Dispersion Strengthening

Precipitation and dispersion strengthening have very similar mechanisms for increasing the strength of a material. In precipitation strengthening, a second phase precipitates from a supersaturated solid solution. One of the classic examples of this type of system is the precipitation strengthening of Ni-based alloys by γ' (Ni_3Al) (7). In dispersion strengthening, the second phase is either added through processing or formed through a chemical reaction. The mechanical alloying technique is common for the oxide dispersion strengthened (ODS) alloys. The formation of a dispersion through a chemical reaction is exemplified by the oxidation of Al in Cu-Al alloys to form a very fine dispersion of Al_2O_3 particles (1).

Strengthening of a material by precipitation or dispersion strengthening occurs through the interaction of dislocations moving through the matrix with the particles. To calculate the increase in strength, one can begin with the general theory that interrelates the obstacle strength, F, the effective particle spacing, L, and the flow stress, τ, required to move the dislocation past the particle as done by Lloyd (28). Williams and Thompson also give an excellent review of the strengthening mechanisms in metals (29).

Figure 9 shows a dislocation pinned by three particles. The particles are spaced a distance L apart. The dislocation forms an angle of ϕ between the two arms of the dislocation at the particles. The arc of the dislocation is defined by the angle θ.

From the force balance of the system,

[1] $$F = 2T\cos\left(\frac{\phi_C}{2}\right)$$

where

T = dislocation line tension

ϕ_C = critical angle where forces are in equilibrium

The applied stress causes the dislocation to bow into an arc with a radius of curvature R. If one assumes T is independent of the character of the dislocation (edge, screw, or mixed), then

[2] $$\tau b = \frac{T}{R}$$

where

τ = flow stress

b = Burgers vector of dislocation

From Figure 9, geometry gives us the relationship

[3] $$R = \frac{L}{2\sin\left(\frac{\theta}{2}\right)}$$

Substituting Equation [3] into Equation [2] yields

[4]
$$\tau b = \frac{2T\sin\left(\frac{\theta}{2}\right)}{L}$$

Geometry also shows that

[5]
$$\frac{\theta}{2} = \left(90 - \frac{\phi}{2}\right)$$

and trigonometry tells us that $\sin\left(\frac{\theta}{2}\right) = \cos\left(90 - \frac{\theta}{2}\right)$, so combining Equations [1], [4], and [5] gives the final desired equation relating τ, F, and L

[6]
$$\tau = \frac{F}{bL}$$

To predict the value of τ, the values of F and L must be calculated. The determination of these two values depends of the precipitates, volume fraction, and strengthening mechanisms.

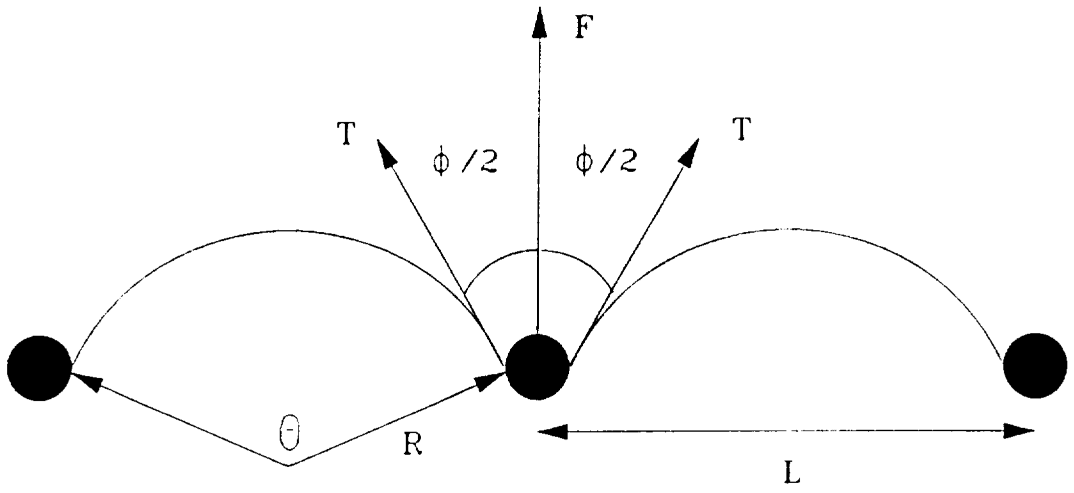

Figure 9 - Dislocation Pinned by Precipitates

2.2.1 Effective Particle Spacing

Friedel (30) determined the spacing for a regular square array of particles interacting with a dislocation. Friedel assumed that the dislocation, after breaking free of a particle, will bow out until it meets one and only one particle. Under these conditions the effective particle spacing L is given by the equation

[7] $$L = \frac{L_S}{\left[\cos\left(\frac{\phi}{2}\right)\right]^{1/2}}$$

where

L_S = spacing between particles

= $N_S^{-1/2}$ where N_S is number of obstacles per unit area in the glide plane

The Friedel spacing implies that the dislocation is essential straight, a good assumption for weak obstacles. Substituting this value of L into Equation [4] and rearranging appropriately yields the equation

[8]
$$\tau = \frac{2T\left[\cos\left(\frac{\phi}{2}\right)\right]^{3/2}}{bL_S}$$

This equation allows a comparison between experimental measurements of ϕ and τ to be made. The results are shown in Figure 10. There is good agreement when ϕ is greater than 140° which corresponds with weak obstacles. For strong obstacles the agreement is poor at best.

For strong obstacles where $\phi < 100°$ and Orowan looping occurs, Brown and Ham (31) have proposed the equation

[9]
$$\tau = \frac{0.8}{bL_S}\left[2T\cos\left(\frac{\phi}{2}\right)\right]$$

For this study Equation [9] is more likely to apply given the expectation that the particles will act as strong obstacles to the movement of dislocation through the Cu matrix.

For the Orowan looping process, it is often necessary to take into account the size of the particles. This is particularly applicable when the volume fraction of the precipitates or the size of the precipitates is large. Under these conditions the effective particle spacing becomes

[10]
$$L_S = N_S^{-1/2} - 2r_s$$

where

r_S = the average planar particle radius in the glide plane

r_s is related to the average particle radius and the volume fraction of the particles, f, by the equations

[11] $$r_s = \frac{\pi r}{4}$$

[12] $$f = \frac{\pi r_s^2}{L_s^2}$$

Combining Equations [10], [11], and [12] yields

[13] $$L_s = \left(\frac{32}{3\pi}\right)^{1/2} r_s = \left(\frac{2\pi}{3f}\right)^{1/2} r$$

These equations are based on the assumption that the particles are spherical. Ellipsoidal, needle, and plate shapes are also common for many precipitates and irregular shapes often occur for dispersoids. The random orientation of these particles and irregularities in shape result in the inability to generalize r_s in these systems.

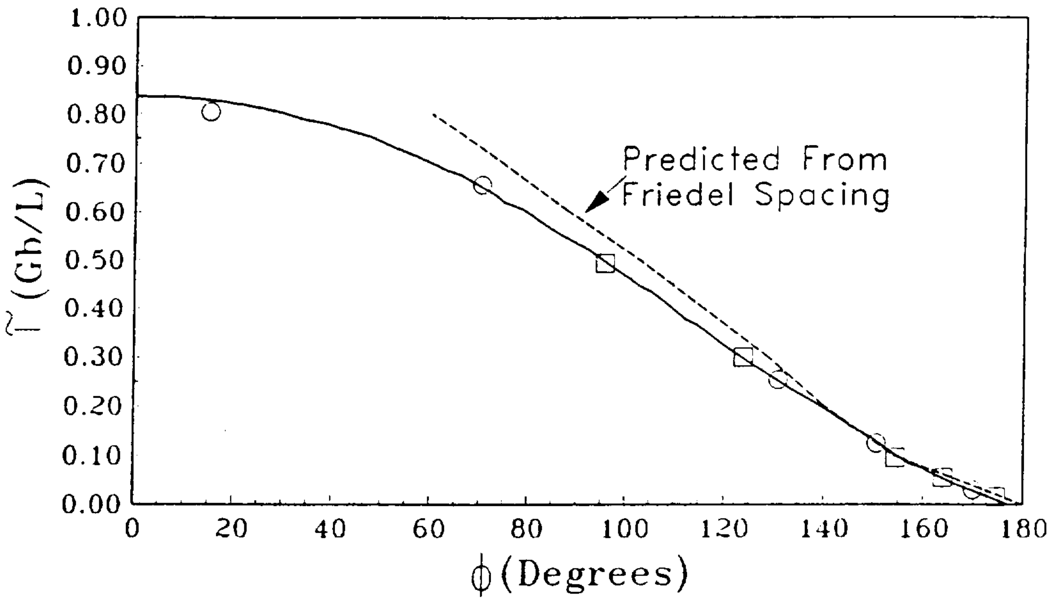

Figure 10 - Comparison Between Experimentally Measured Shear Stresses and Dislocation Bend Angle And Predicted Values
From Lloyd (28)

2.2.2 Obstacle Strengths

The strength of the obstacles, here the particles, depends on the way that the dislocations interact with the obstacles. There are six ways that the obstacles can strengthen the material; chemical or surface strengthening, stacking fault energy strengthening, modulus strengthening, coherency strengthening, order strengthening, and Orowan strengthening.

2.2.2.1 Chemical Strengthening

Chemical strengthening occurs when the dislocations penetrate the particles. The movement of a dislocation through the particle produces a ledge of size b. This ledge has an energy associated with it since it creates a new matrix/particle interface. If the interfacial energy is γ_S, the maximum force acting on a dislocation is

[14] $$F_{Max} = 2\gamma_S b$$

Appropriate substitution of this value of F into Equation [1] and the result into Equation [8] yields

[15] $$\tau_{CS} = \frac{2\gamma_S^{3/2} b^{1/2}}{T^{1/2} L_S}$$

Assuming a square lattice of particles spaced a distance L_S apart for determining the Friedel spacing, the values for τ_{CS} become

[16] $$\tau_{CS} = \left[\frac{6\gamma_S^3 b f}{\pi T}\right]^{1/2} \frac{1}{r}$$

In most materials, the strength of the material increases with increasing particle size in the early stages of aging (28). This observation differs with Equation [16]. This implies that the only time chemical strengthening would be a major contribution to the strength of the alloy would be when nucleation is easy but growth hard. Under those conditions f would increase while r would be almost constant. Harkness and Hren (32) have attributed this strengthening mechanism to the Al-Zn system, but Gerold (33) disputes this conclusion.

2.2.2.2 Stacking Fault Energy Strengthening

If the matrix and particles have dislocations that form stacking faults, the differences in the stacking fault energies of the dislocations in the matrix and particle results in a force acting on the dislocations. The maximum force from this mechanism is given by the equation

$$F_{\mathrm{Max}} = \Delta\sigma r_s B \tag{17}$$

where

$\Delta\sigma$ = the difference in the stacking fault energies

B = a parameter that is a complex function of $\Delta\sigma$, T, and r_s

If r_s is less than the partial dislocation separation in the matrix, Equation [17] becomes

$$\tau_{SF} = \Delta\sigma^{3/2}\left[\frac{3\pi^2 f r}{32 T b^2}\right]^{1/2} \tag{18}$$

Gerold and Hartman (34) showed that dilute Al-Ag alloys follow this type of behavior while Kovacs et al. (35) had good agreement with Equation [18] for GP zones in Al-Mg-Zn alloys.

The dependency of strength on the quantity $(fr)^{1/2}$ is not unique to stacking fault strengthening. It also occurs in modulus and coherency strengthening as will be shown.

2.2.2.3 Modulus Strengthening

The energy of a dislocation is a function of the shear modulus of the material. Knowles and Kelly (36) have derived the expression for r > 2b

[19]
$$\tau_G = \frac{\Delta G}{4\pi^2}\left(\frac{3\Delta G}{G_M b}\right)^{1/2}\left[0.8 - 0.143\ln\left(\frac{r}{b}\right)\right]^{3/2} r^{1/2} f^{1/2}$$

where

G_M = shear modulus of the matrix

ΔG = difference in shear stress between the matrix and precipitate

for r > 2b. Melander and Persson (37) for a computer simulation based on the work by Hanson and Moris (38) derived the expression

[20]
$$\tau_C = 0.9(fr)^{1/2}\frac{T}{b}\left(\frac{\Delta G}{G_M}\right)^{3/2}\left[2b\ln\left(\frac{2r}{f^{1/2}b}\right)\right]^{-3/2}$$

Ungar et al. (39) have found that the aged strength of Al-Mg-Zn alloys are linear when plotted against $(fr)^{1/2}$, but again this dependency is not unique to modulus strengthening.

Experimental confirmation of this mechanism is difficult since in most cases the shear stress of the precipitates is not known.

2.2.2.4 Order Strengthening

For order strengthening the particles must have an ordered structure. An example of this would be γ' in Ni-Al alloys. Order strengthening is very similar to stacking fault energy strengthening. Instead of the dislocations having to overcome the energy barrier associated with a stacking fault, the dislocations must overcome the energy of the antiphase boundary.

For a single dislocation moving through an ordered particle, the maximum force acting on the dislocation is given by

[21]
$$F_{max} = 2\sigma_{APB} r_s$$

where

σ_{APB} = antiphase boundary energy

Appropriate substitutions for Equations [1], [8], and [13] yields the flow stress required to move the dislocation through the particle which is defined by the equation

[22]
$$\tau_o = \frac{\sigma_{APB}}{b}\left[\frac{4\sigma_{APB} f r}{\pi T}\right]^{1/2}$$

However dislocations move through ordered materials in pairs, so the effect of ordering must be applied to a pair of dislocations. If one assumes that $r_s = (2/3)^{1/2} r$, a slightly inaccurate value used by Brown and Ham (31) and that the leading dislocation is bowed out while the trailing dislocation is essential straight, the flow stress can be determined using the expressions

[23]
$$\tau_o = \frac{\sigma_{APB}}{2b}\left[\left(\frac{4\sigma_{APB} r f}{\pi T}\right)^{1/2} - f\right]$$

for $r < \frac{T}{\sigma_{APB}}$ and

[24] $$\tau_o = \frac{\sigma_{APB}}{2b}\left[\left(\frac{4f}{\pi}\right)^{1/2} - f\right]$$

for $r > \frac{T}{\sigma_{APB}}$.

Noble, Harris, and Dinsdale (40) examined the strengthening of Al-Li alloys by the δ' phase. The misfit between the matrix and the precipitates is only about 0.1% for these alloys, so there should be little contribution from coherency strengthening. Using Equation [23] they were able to explain the strengthening of the alloys accurately.

2.2.2.5 Coherency Strengthening

The four strengthening mechanisms discussed up to now; chemical strengthening, stacking fault energy strengthening, modulus strengthening, and order strengthening; require that the dislocations travelling through the matrix penetrate the particles. In the case of very hard particles and a soft matrix, typical of dispersion strengthened Cu alloys, the dislocations will probably not be able to shear the particles. Under this condition coherency strengthening and Orowan strengthening become the primary strengthening mechanisms.

Coherency strengthening is caused by the accommodation of particles with a different specific volume than the matrix through the generation of an internal stress in the matrix. The misfit parameter, ϵ, is defined as

[25] $$\epsilon = \frac{1}{3}\left(\frac{1+\nu}{1-\nu}\right)\frac{\Delta a}{a} \approx \frac{2\delta}{3}$$

where

a = lattice parameter of the matrix

Δa = difference in lattice parameters of the matrix and precipitate

ν = Poissons ratio for the matrix

δ = fractional difference in lattice parameters for the matrix and particles

Assuming a spherical, coherent precipitate interacting with a straight dislocation, Gerold and Haberkorn (41) developed the equations

[26] $$F = \left(\frac{3}{2}\right)^{3/2}\frac{Gb|\epsilon|r^3}{z^2}$$

for $\frac{z^2}{r^2} > \frac{3}{4}$ where z is defined as the distance of the glide plane of the dislocation from the center plane of the particle and

[27] $$F = 8Gb|\epsilon|z\left(1 - \frac{z^2}{r^2}\right)^{1/2}$$

for $\frac{z^2}{r^2} < \frac{3}{4}$. The maximum force developed occurs when $\frac{z^2}{r^2} = \frac{1}{2}$. The value for F_{Max} is given by the equation

[28]
$$F_{\mathrm{Max}} = 4Gb|\epsilon|r$$

To determine the value of τ_{CS}, the appropriate value for F to be substituted into Equation [1] and [8] must be determined. This value must also take into account the interactions of the dislocations a distance away from the glide plane. The result is some type of statistical averaging with equation for τ_{CoS} having the general form

[29]
$$\tau_{CoS} = k(\epsilon G)^{3/2}\left(\frac{r f b}{T}\right)^{1/2}$$

where

k = a constant dependent on the averaging technique

Gerold and Haberkorn (41) used values of k=3 for edge dislocations and k=1 for screw dislocations. Gleiter (42) used a value of 11.8 for k. The equation is good for systems with small particle sizes, straight dislocations, and small breakaway angles for the dislocations.

Comparison of the results with experimental results is difficult since the values of the constant k are very approximate at best. Witt and Gerold (43) examined the Cu-Co system and determined that the coherency strengthening mechanism grossly overestimates the strength of the materials.

Oblak, Paulonis, and Duvall (44) during their examination of coherency strengthening examined the effect of ellipsoidal particles. For particles with an aspect ratio and volume given by the equations

[30] $$A = \frac{h}{r}$$

[31] $$V = \frac{4\pi r^2 h}{3}$$

where

A = aspect ratio

h = long axis radius

r = short axis radius

V = volume of particle

they determined that the force was given by the equation

[32] $$F = \frac{4\pi G b \epsilon h}{3\lambda}$$

with λ equal to 2.2 for edge dislocations. The effective obstacle spacing for these particles is given by

[33] $$L = \frac{4\pi h T}{\sqrt{6 F f}}$$

and the dislocation line tension is given by

[34] $$T = \frac{G b^2}{2}$$

Using these values and substituting appropriately, the value of τ_{CoS} was calculated to be

[35]
$$\tau = 1.7 G \epsilon^{3/2} \left(\frac{h^2 f}{2br} \right)^{1/2}$$

Oblak, Duvall, and Paulonis (45) found that this equation underestimated the strength of Inconel 718 by about 10% while Chaturvedi and Chung (46) found that the equation underestimated the strength of a cobalt-based alloy by 50%.

2.2.2.6 Orowan Strengthening

Orowan strengthening occurs when the particles cannot be sheared by a dislocation. In this case the breakaway angle ϕ approaches 0°. The force of the obstacle when ϕ is 0° is given by the equation

[36]
$$F = 2T$$

Substituting Equation [36] into Equation [6] yields the expression

[37]
$$\tau_o = \frac{2T}{bL}$$

In the simplest form, the dependency of the dislocation line tension on the shear modulus of the material is given by the equation

[38]
$$T = \frac{Gb^2}{2}$$

Substitution yields

[39]
$$\tau_o = \frac{Gb}{L}$$

This simple analysis neglects the interaction between the two arms of the dislocation moving around the obstacle which must be taken into account. These two arms form a dislocation dipole with a separation width of 2r. The effective dislocation line tension for the dislocation is given by the expression

[40]
$$T = \frac{Gb^2}{4\pi}\left[\frac{1 + \nu - 3\sin^2\xi}{1 - \nu}\right]\ln\left(\frac{2r}{r_o}\right)$$

where

r_0 = inner cutoff radius of the dislocation, normally taken as equal to b

ξ = angle between the Burgers vector and the dislocation line tension

The actual spacing of the dislocation dipole depends on the nature of the dislocation, but the differences in character tend to balance out with the change in separation (28). As a result the flow stress needed is virtually independent of the nature of the dislocation and is given by the equation

[41]
$$\tau = \frac{0.8Gb}{2\pi(1 - \nu)^{1/2}L}\ln\left(\frac{2r}{r_o}\right)$$

Bacon, Harris, and Dinsdale (47) have developed an alternative expression for Orowan strengthening of a material with a random dispersion of impenetrable particles. Their expression for flow stress

[42]
$$\tau = \left[\frac{\ln(2r)}{\ln(L)} \right]^{1/2} \frac{Gb}{2\pi L} \ln\left(\frac{2r}{r_o} \right)$$

gives values that are close to the values for Equation [41] and are normally well within the experimental error of the measurements.

Overaging occurs for alloys strengthened by Orowan strengthening because for growing particles with a constant total volume fraction, the increase in size results in an increase in the particle spacing with a corresponding decrease in strength as predicted by Equations [41] and [42].

Work by Hansen (48) on fully recrystallized Al-Al_2O_3 alloys showed that the system gave good correlation with the predicted values.

Ashby later expanded on the Orowan model to develop the Ashby-Orowan model.

2.2.2.7 Ashby-Orowan Model

The Ashby-Orowan model (49) predicts the effect of precipitates on the strength of a material. The model uses the realistic random particle distribution model of Kocks (50) to model the distribution of precipitates in the matrix.

The Ashby-Orowan model predicts

[43]
$$\tau_{AO} = \frac{1.2Gb}{2.36\pi L} \ln\left(\frac{x}{2b} \right)$$

where

τ_{AO} = resolved shear stress to overcome obstacle strength of precipitates

G = shear modulus

b = Burgers vector of the material in the slip direction

L = spacing between precipitates

x = mean planar intercept diameter of the precipitates

The effect of particle size and volume fraction of the precipitates can be calculated by assuming the precipitates are spherical. The volume fraction of precipitates, V_f, is given by

[44] $$V_f = \frac{n_S \pi x^2}{4}$$

where

n_S = number of precipitates per unit area of the slip plane

The spacing of the precipitates is then given by

[45] $$L = x\left[\left(\frac{\pi}{4V_f}\right)^{1/2} - 1\right]$$

which can be reduced to

[46] $$L = x\left(\frac{\pi}{4V_f}\right)^{1/2}$$

if the spacing of the particles is much greater than the size of the particles (L>>x), a simplification that may not be applicable to alloys forming large volume fractions of precipitates. Substituting Equation [46] into Equation [43] gives

$$\sigma = K\left(\frac{V_f^{1/2}}{r}\right)\ln\left(\frac{r}{b}\right) \quad [47]$$

where

σ = yield strength of the material = 2 τ

K $= \frac{2.4\ G\ b}{2.36\ \pi^{3/2}} = 0.1826\ Gb$

r = average radius of the precipitates

From this, two important points can be immediately seen. The yield strength of the material increases as the volume fraction of precipitate increases and the average precipitate radius decreases. Since the yield strength increases only as the square root of the volume fraction of the precipitates, the more effective method for increasing the yield strength is to decrease the size of the precipitates. Rapid solidification has the advantage that both methods of increasing strength, increasing the volume fraction and decreasing the size of the precipitates, can be accomplished.

2.2.3 Multiple Precipitate Phases

Often multiple types of precipitates are present in alloys. Under this condition it is necessary to understand how the precipitates act to combine their strengthening effects.

For a system with two different types of particles with N_{S1} particles of type 1 and N_{S2} particles of type 2, the flow stress required to move a dislocation past each individual type of particle is given by

[48]
$$\tau_1 = \frac{\tau_1^* T N_{S1}}{b}$$

and

[49]
$$\tau_2 = \frac{\tau_2^* T N_{S2}}{b}$$

where

$$\tau^* = 2\left[\cos\left(\frac{\phi}{2}\right)\right]^{3/2}$$

τ^*_1 and τ^*_2 are functions representing the dependency of the flow stress on the angle between the dislocation and the direction of the force acting on the dislocation.

There are four basics means for combining the effects of the two types of precipitates; linear superposition, Pythagorean addition, law of mixtures, and an adjustable parameter approach.

For the linear superposition case, the flow stress for the material is given by a sum of the flow stress from the individual precipitates or

[50]
$$\tau_C = \tau_1 + \tau_2$$

In terms of the fraction of each type of particle present and the total number of particles present,

[51] $$\tau_c^* = \tau_1^* X_1^{1/2} + \tau_2^* X_2^{1/2}$$

where

$X_1 = \frac{N_{S1}}{N_S}$

$X_2 = \frac{N_{S2}}{N_S}$

N_S = total number of particles present in the material

The Pythagorean addition rule proposed by Koppenaal and Wilsdorf (51) states that the sum of the squares of the flow stress for the strengthening by the individual types of particles is equal to the square of the flow stress of the material or

[52] $$\tau_c^2 = \tau_1^2 + \tau_2^2$$

and after appropriate substitution

[53] $$(\tau_c^*)^2 = (\tau_1^*)^2 X_1 + (\tau_2^*)^2 X_2$$

The law of mixtures predicts that the flow stress for a material would be given by the expression

[54] $$\tau_c = \tau_1 X_1^{1/2} + \tau_2 X_2^{1/2}$$

or

[55] $$\tau_C^* = \tau_1^* X_1 + \tau_2^* X_2$$

In addition, Buttner and Newbach (52) and Neite et al. (53) have proposed the adjustable parameter law

[56] $$\tau_C^q = \tau_1^q + \tau_2^q$$

where q is an adjustable parameter for the system. Comparison to the computer generated flow stresses generated by the simulations of Foreman and Makin (54) for various values of τ^*_1 and τ^*_2shows that the best results are given by the Pythagorean addition rule though the adjustable parameter rule with $q \approx 2$ could also explain the results.

The effect of multiple precipitates is important to remember since the Cu-Cr-Nb system has the potential to form precipitates of elemental Cr and elemental Nb as well as the intermetallic phase Cr_2Nb depending on the kinetics and composition.

2.3 Nucleation and Growth of Precipitates

When a single phase material is quenched from an elevated temperature into a two phase region, a supersaturated solid solution can be produced. The supersaturated solid solution can form precipitates during ensuing aging. The fine dispersion of precipitates produced greatly increase the strength of the material as outlined in the previous section. Several alloys make use of quenching and aging to achieve their good mechanical properties. Among them are the γ' strengthened superalloys, Cu-Be alloys, and Al-Cu alloys.

2.3.1 Nucleation of Precipitates

Nucleation of precipitates in the supersaturated solid solution can occur either homogeneously or heterogeneously. In homogeneous nucleation, the precipitates form spontaneously due to small local fluctuations in the composition of the material (55). Homogeneous nucleation is difficult with a large driving force such as a large undercooling required to drive the precipitation reaction (55). Heterogeneous nucleation is easier and more common.

During heterogeneous nucleation, the precipitates form at defects in the crystal such as dislocations, impurity particles, and grain boundaries (55). These imperfections lower the energy required to form the matrix-precipitate interface by at least 1/2. As a result the energy barrier for the formation of the precipitates is greatly lowered and precipitation can occur with less undercooling or a lower magnitude of compositional fluctuation.

For homogeneous nucleation of a solid in the liquid phase, large undercoolings are required to drive the reaction (56). The presence of solids such as inclusions and the mold walls promote heterogeneous nucleation by lowering the energy barrier for the formation of the solid phase (55).

2.3.2 Growth of Precipitates

Once the nuclei form in the solid, the precipitates undergo growth. The size of the precipitates during the growth stage depends on the nuclei size, the diffusivity of the elements in the matrix, the degree of supersaturation, and the time into the growth stage. Quantatively the size of the B precipitates forming in the supersaturated matrix is given by the equation (57)

[57] $$r^2 - r_o^2 = \frac{\Delta X_o^2}{(X_B - X_{Eq})^2} Dt$$

where

r^2 = radius of precipitate squared

r_o^2 = radius of nuclei squared (typically taken to be zero)

ΔX = Concentration of alloy minus equilibrium solubility of B in α at the temperature

X_B = Equilibrium concentration of B in β at the temperature

The growth of the precipitates thus follows a parabolic growth rate. Growth continues until the supersaturation approaches zero when the precipitates begin to undergo coarsening.

2.3.3 Coarsening of Precipitates

Coarsening of precipitates is caused by the difference in chemical potential between particles of different radii. This phenomena was first described by Ostwald and is called Ostwald ripening (58).

The driving force for coarsening of precipitates can be expressed as

[58] $$\mu_P = 2\gamma_S V\left(\frac{1}{r_1} - \frac{1}{r_2}\right) = \frac{k_B T \Delta C_B}{C_B}$$

where

μ_P = difference in chemical potential

V = atomic volume

r_1, r_2 = radii of the two particles

k_B = Boltzmann's constant

T = absolute temperature

ΔC_B = solute concentration gradient between particle 1 and 2

C_B = average concentration of solute in the matrix

γ_S = surface energy of precipitates

Lifshitz and Wagner (57) expanded this idea to give the Lifshitz-Wagner Law

[59]
$$r^3 - r_o^3 = \frac{D_B \gamma_S C_B V^2 t}{k_B T}$$

where

r = average precipitate radius

r_o = initial precipitate radius at end of growth stage

D_B = diffusivity of the solute in the matrix

t = time

The Lifshitz-Wagner Law allows for the calculation of the average precipitate size at any time knowing the initial precipitate size when conventional growth has concluded and some physical constants. More importantly the relationship and its first derivative with respect to time can be used to qualitatively examine the effect of several diverse factors on the coarsening of precipitates. The growth rate of the precipitates is directly proportional to the diffusivity of the solute in the matrix. As such, the use of slowly diffusing elements for the precipitates will decrease the coarsening kinetics. Frequently elements with atomic diameters much greater than the matrix atoms will diffuse slowly.

The coarsening kinetics and the precipitate size are also directly proportional to the solubility of the solute in the matrix. Low solubility of a solute in the matrix results in a lower flux of atoms to the growing precipitates compared with a system with a higher solubility of solute with all else being equal. The lower flux results in a smaller average precipitate size.

The dependency of the growth kinetics and the precipitate size on temperature arises from the dependency of diffusivity, maximum solute concentration in the solid, and surface energy on temperature. The diffusivity of the solute and the maximum solid solubility of the solute depend exponentially on temperature (59,60) while the surface energy has a linear dependency (61). To a first approximation, the dependency of coarsening on temperature is proportional to $e^{\frac{-2}{T}}$. The aging temperature thus has the greatest influence on the growth of precipitates.

2.4 Mechanical Properties of Cu-Based Alloys

The mechanical properties of Cu-based alloys vary greatly. Fully annealed Cu has a yield strength of only 48 Mpa (7.0 ksi) (10) while Cu-Be alloys such as C 172 can obtain a yield strength of 1410 MPa (204 ksi) (62) at room temperature in the fully hardened condition. Cold working of the materials can also greatly increase the strength of these alloys. The yield strength of hot rolled Cu can be doubled from 242 MPa (35 ksi) to 483 MPa (70 ksi) by cold working the material 90 per cent (63).

The problem with many of these alloys is the decrease in strength experienced by the alloys when the temperature increases above room temperature. Figure 11 taken from Crosby and Desy (64) shows the loss in strength experienced by Cu with even small increases in temperature. At 500°C the strength of Cu has dropped to less than 35 MPa (5 ksi) from the initial 414 MPa (60 ksi) room temperature value.

To combat this problem and also prevent relaxation in the cold worked Cu, alloys were developed that allowed the operating temperature of the materials to be increased by increasing the softening temperature of the materials. While some solid solution strengthening alloys do have elevated softening temperatures (10), most of the high temperature alloys are either precipitation or dispersion strengthened. Recently some Cu-Nb composites have been shown to have good elevated temperature mechanical properties (65).

Table 1a briefly summarizes the mechanical properties of some of the available precipitation strengthened Cu-based alloys and Cu at room temperature and elevated temperatures near 500°C. The values for Cu-Nb *in situ* composites are also included. Table 1b summarizes the room temperature yield strength of some rapidly solidified precipitation strengthened Cu-based alloys in the as-melt spun and aged conditions.

Table 1a
Strengths of Conventional Cu and Cu-Based Alloys at
Room Temperature and Elevated Temperatures

Alloy/Element	Temperature (°C)	Condition	Yield (MPa)	UTS (MPa)	Ref.
Cu	20	O	48	263	65
		H	265	314	
	204	N/A	70	159	
Cu - 0.05 Ag	20	O	54	224	10,69
		H	263	316	
	500	N/A		107	
Cu - 14.3 Nb	20	η = 8.16		900	70
		η = 10.05		1400	
	500	η = 8.16		325	
		η = 10.05		515	
Cu - 0.6 Cr	20	O	54	232	10,69
		H	479	541	
		P	324	448	
	550	O		148	
		P		210	
Cu - 1.85 Be - 0.25 Co	20	O	224	479	10
		H	1205	1313	
		P	1066	1205	
GLIDCOP (Cu-Al_2O_3)	20			394*	66
	500			222	

O = Fully annealed
H = Fully work hardened
P = Fully precipitation hardened
η = Draw ratio (See Section 2.4.3, Equation [60])
* - Extrapolated from higher temperature data

Table 1b
Room Temperature Yield Strengths of Rapidly Solidified Cu-Based Alloys

Alloy	Aging Treatment	Yield (MPa)	Ref.
Cu - 0.5 Mn - 1 B	None	268	67
	500° C / 30 min	248	
Cu - 1 Mn - 2 B	None	359	67
	500° C / 30 min	386	
Cu - Mn - 2 B	None	402	67
	500° C / 30 min	402	
Cu - 2 Mn - 2 B	None	559	67
	500° C / 30 min	505	
Cu - 4 Mn - 6 B	None	652	67
	500° C / 30 min	644	
Cu - 1 Si 4 B	None	387	67
	500° C / 30 min	426	
Cu - 1 Si - 6 B	None	497	67
	500° C / 30 min	486	
Cu - 2 Si - 8 B	None	576	67
	500° C / 30 min	549	
Cu - 2 Cr	None	200	68
	500° C / 1 hr	493	
Cu - 5 Cr	None	346	68
	500° C / 1 hr	673	

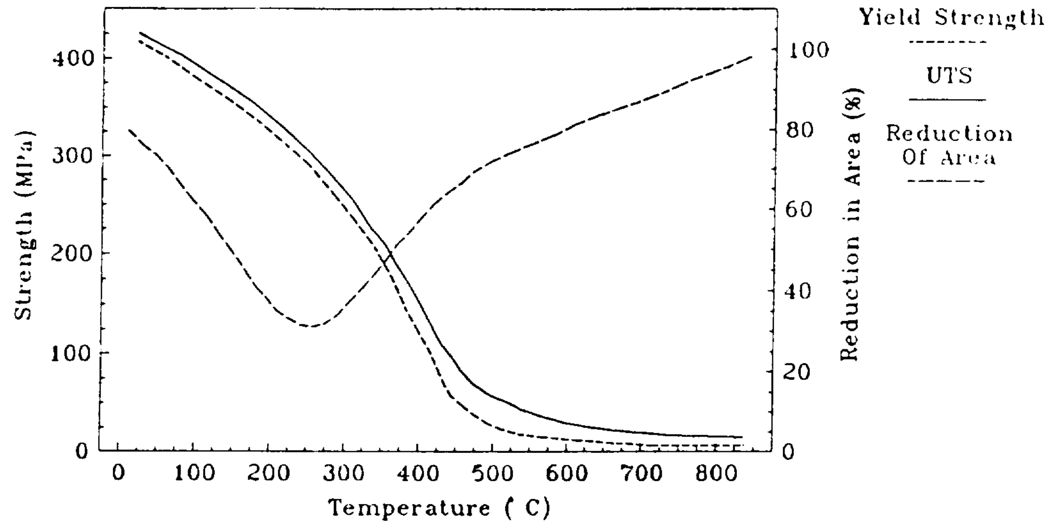

Figure 11 - Tensile Strength and Reduction of Area for Cu as a Function of Temperature From Crosby and Desy (64)

2.4.1 Precipitation Strengthened Cu-Based Alloys

Many Cu-based alloys derive their strength from the precipitation of a second phase. Some of these alloys are Cu-Be (10), Cu-Zr (69), Cu-Cr-Zr (70), Cu-B (71), Cu-Mn-B (67), Cu-Si-B (67), and Cu-Cr (10). These alloys exhibit good strength while retaining good ductility. These alloys also have higher softening temperatures than pure copper.

Cu-Be is one of the strongest Cu-based alloys at room temperature (72). Overaging of the material limits its use above room temperature. The strength of the alloys rapidly decreases above room temperature with the strengths dropping rapidly above 260°C (500°F).

Cu-Zr alloys such as AMZIRC derive their strength from the precipitation of the Cu_3Zr intermetallic phase (73). Cu-Cr-Zr also gains strength from the precipitation of elemental Cr precipitates like those seen in Cu-Cr alloys (68).

Cu-B derives its strength from elemental B precipitates. The B particles studied by Batawi, Morris, and Morris (71) were initially amorphous and resistant to coarsening. After aging the B precipitates crystallize and coarsen quickly. Enhanced solute diffusion along the high-density regions of the grain boundaries contributes to the rapid coarsening. The coarse precipitates cannot pin the grain boundaries and coarsening of the Cu matrix grains occurs. As the B precipitates coarsen, the ability of the precipitates to strengthen the material decreases.

The addition of Mn and Si to these alloys allows the formation of MnB_x and SiB_x precipitates that coarsen less quickly than the elemental B precipitates. The Cu-Mn-B alloys studied by Morris, Batawi, and Morris (67) retained their room temperature yield strength after aging for 30 minutes up to 500°C. The Cu-Si-B alloys had even better strength retention with loss in the room temperature yield strength occurring only after aging at temperatures above 600°C for 30 minutes. Morris, Batawi, and Morris attributed the good strength of these alloys to the pinning of the Cu grain boundaries to give a Hall-Petch strengthening effect plus an Orowan strengthening mechanism for the precipitates.

The precipitation strengthened Cu alloy most closely associated with this study is Cu-Cr.

2.4.1.1 Cu-Cr Alloys

The Cu-Cr alloys are strengthened by the precipitation of elemental Cr precipitates from the supersaturated solid solution (74). The maximum Cr content of conventional alloys is limited to approximately 0.6 w/o, the limit of solid solubility of Cr in Cu (24).

The precipitation of Cr in Cu has been studied by both X-ray diffraction and electron microscopy. The earlier X-ray diffraction study by Williams (75) and Gruhl and Fischer (76) detected the precipitation by <111> streaking of the Laue patterns of the alloys. Because of this streaking, William, Gruhl, and Fischer suggested that the Cr was precipitating as a metastable FCC or CPH phase. The more recent electron microscopy work by Lynch (77) on a 0.4% Cr alloy has shown that the precipitates are rod shaped and have the equilibrium BCC structure. Only when these rods are large is there significant streaking of the Laue pattern.

The Cr precipitates have been reported to form a Kurdjumov-Sachs type of orientation relationship with the Cu matrix (78,79). This relationship has parallel close packed planes and directions at the precipitate/matrix interface. In addition, for Cu-Cr alloys containing P, Witcomb, Dahmen, and Westmacott (80) have shown that an additional precipitate, Cr_3P, coprecipitates on the Cr precipitates with a definite relationship to both the Cr precipitates and Cu matrix. However, Kamijo, Furukawa, and Watanabe (81) have shown that theoretically FCC Cr particles could form based on the free energy for the precipitation process.

Clarke and Stobbs (82) have also investigated the orientation relationship between Cu and Cr in directionally solidified Cu-1.9 w/o Cr alloy. By obtaining the Kikuchi lines for both Cu and Cr simultaneously, they were able to determine the orientation of both the precipitates and matrix. Their results indicate that the orientation is intermediate between the Kurdjumov-Sachs and Nishiyama-Wasserman relations.

The effect of the fine dispersion of Cr precipitates is a significant increase in strength and the temperature at which the material losses its good strength. At room temperature the yield strength of Cu-0.6 Cr increases from 54 MPa to 324 MPa when fully precipitation hardened (10). Non-equilibrium processing such as melt spinning has the potential to extend the solid solubility of Cr significantly and therefore increase the amount of precipitate and strength of the material. The increase in hardness for a variety of melt spun Cu-Cr alloys with Cr contents ranging from 0.52% to 6.4% studied by Tenwick and Davies (83) is evidence of this. The Vickers hardness of the melt spun ribbons and ribbons aged at 450° C for a variety of times up to 24 hours showed that the 6.4% Cr alloy achieved a peak hardness of nearly 350 VPN while the peak hardness of the 0.52% Cr alloy was only 110 VPN.

The resistance to softening of Cu-Cr alloys was studied by Horn and Lewis (84). For a Cu-0.7 Cr alloy with 84% cold work age hardened at 450°C (840°F), the results showed that the material retained over 50% of the ultimate tensile strength after aging at 500°C (932°F) for 30 minutes. In contrast, electrolytic tough pitch Cu cold worked 84% had lost 60% of its yield strength after aging at 204°C (400°F) for the same length of time.

The primary problem with the Cu-Cr alloys is the overaging of the material. This is particularly evident in the work by Tenwick and Davies (83) where the room temperature hardness of the materials decreased significantly after only 1 to 2 hours of aging at temperatures between 400°C and 500°C. The high diffusivity of Cr in Cu (85) which should lead to quick coarsening of the particles and overaging is probably the reason for this problem.

2.4.2 Dispersion Strengthened Cu-Based Alloys

Several dispersion strengthened Cu-based alloys have been studied. GLIDCOP (Cu-Al_2O_3) alloys, Cu-ZrO_2 alloys and Cu-ThO_2 alloys are examples of these alloys.

Oxide dispersion strengthened Cu-based alloys are generally produced by powder metallurgy (P/M) techniques. Often the reactive element such as Al or Zr is internally oxidized under carefully controlled conditions to produce a fine dispersion of oxide particles with minimal residual oxygen dissolved in the Cu matrix. Often this is done during the powder production stage though it is possible to introduce the oxygen into a consolidated part. Mechanical alloying is also used to achieve the oxide dispersion. For the GLIDCOP Al_2O_3 dispersion strengthened alloys, the oxide particles are reported to be 8.0 nm in diameter (66) though there is some dispute that they are that fine (86).

ODS Cu-based alloys are the only alloys that retain significant strengths above 649°C (1200°F). ThO_2 dispersion strengthened Cu has an ultimate tensile strength of more than 104 MPa (15 ksi) up to a temperature of 982°C (1800°F) (87). GLIDCOP alloy has an ultimate strength of 138 MPa (20 ksi) at 649°C that decreases to 69 MPa (10 ksi) at 871°C (1600°F) (66). In comparison, NARloy-Z has an ultimate tensile strength of only 69 MPa (10 ksi) at 649°C (88,89).

The creep behavior of these alloys are also exceptional. The 100-hour stress rupture strength of Cu-Cr alloys above 315°C (600°F) ranges from 148 MPa (22 ksi) at 315°C to 38 MPa (5.5 ksi) at 500°C (932°F) (90). In contrast GLIDCOP 15 and GLIDCOP 35 have 100 hour rupture stresses of more than 207 MPa (30 ksi) (66,91) in the temperature range of 426°C (800°F) to 482°C (900°F). P/M Cu-Cr-ZrO_2-Zr alloys also have good rupture strengths. The rupture strength decreases from 193 MPa (28 MPa) at 316°C (600°F) to 124 MPa (18 ksi) at 482°C with isolated values as high as 331 MPa (48 ksi) being reported in the temperature range (92).

This combination of excellent elevated temperature strength, resistance to softening, and high electrical and thermal conductivities make dispersion strengthened alloys one of the better candidates for rocket nozzle applications.

2.4.3 Cu-Nb In Situ Composites

Recently there has been considerable interest in Cu-Nb composites because of their very high strengths and good conductivities (93). Cu-Nb composites came from work originally done with Cu-Nb_3Sn superconducting composites (94). The Cu-Nb wire bundles or fine grained castings are drawn to the desired size. Sn is diffused into the material to form the superconducting Nb_3Sn phase in a bronze matrix (95). These composites exhibit good strength and high critical currents (94).

The observation of the strength of the composites lead to research on the Cu-Nb system. The desire was to develop a high strength, high conductivity material. Results showed that the initial material has an unexceptional tensile strength that is dramatically increased by the drawing of the material to finer and finer diameters (96).

Spitzig, Pelton, and Laabs (97) examined several Cu-Nb *in situ* composites formed by rod rolling and wire drawing material produced by consumable arc melting. The resulting microstructure was a very fine grained material with long, thin Nb filaments parallel to the drawing direction. Spitzig et al. showed that the ultimate tensile strength showed an anomalous increase with increasing draw ratio, η, where

[60]
$$\eta = \ln\left(\frac{A_o}{A}\right)$$

Spitzig et al. determined from analysis of the results that the primary strengthening mechanism for the material was the introduction of many closely spaced barriers to dislocation movement in the Cu matrix, specifically the Nb filaments. The strengthening behavior follows a Hall-Petch relationship between the filament spacing and the ultimate tensile strength. Maximum strengths were obtained for Cu-20% Nb wires with a draw ratio of 11.9. Deviation from linearity in the true stress-true strain curves was observed near 1000 MPa with the true ultimate tensile strength near 1850 MPa. Elongations for these heavily cold worked materials were approximately 2%.

Karasek and Bevk (65) examined the high temperature strength of Cu-Nb *in situ* composites. The ultimate tensile strengths for a Cu-14.8% Nb material with values of η varying from 8.16 to 10.05 was examined over a temperature range of 300 K to 768 K (80° F to 923° F). The results indicate good strength even at 768 K. The strength of the material ranged from approximately 100 MPa to 520 MPa (14.5 ksi to 75.4 ksi) at 768 K.

2.5 Rapid Solidification Technology

Rapid solidification processes are characterized by very fast cooling rates, high solidification rates, and fine microstructures. Rapid solidification processes can produce a wide range of product sizes and shapes ranging from submicron powders to continuous filaments many meters long.

2.5.1 Rapid Solidification Techniques

There are many methods for producing rapidly solidified materials. The various methods can be subdivided into two categories. The first group relies on dispersing the molten material as fine droplets to achieve conductive and radiative cooling of the molten material (atomization techniques). The second group removes heat from the melt by conductive cooling to a solid substrate (chill techniques). Tables 2 and 3 lists a variety of techniques from both categories with the cooling rates and typical product sizes.

Among the various techniques, powder atomization is one of the more commercially common techniques (98). Gas atomization produces fine particulates suitable for powder processing to desired shapes. Cooling rates for inert gas atomization are usually only 10^2 to 10^3 K/s (99), but the newer supersonic gas atomization and close coupled gas atomization techniques have increased cooling rate to as high as 10^6 K/s (100,101), comparable to the chill techniques. Other high cooling rate techniques such as twin roll atomization are becoming increasingly more accepted as economical alternatives to produce rapidly solidified materials in quantity (99).

Among the chill techniques, laser glazing can achieve the highest cooling rate. Micron thick pools of liquid metal can be self-quenched by the substrate at rates of more than 10^{10} K/s (102). For producing rapidly solidified materials more suitable for consolidation, centrifugal atomization processing and drum splat processing which combine chill and atomization techniques have the ability to produce fine particles with cooling rates as high as 10^5 K/s (103,104). Other techniques such as chill block melt spinning and crucible melt extraction can produce long lengths of materials that can be subsequently chopped up to produce particulates suitable for P/M processing techniques (99,105).

Chill methods can also produce material that are suitable for use in the as-rapidly solidified condition. Melt extraction can produce long lengths of thin sheet material with uniform width and thickness (106). Plasma spray deposition can be used to build up a near-net-shape piece and offers the advantage of being usable with almost any material, even high melting point ceramics (107).

For this study, chill block melt spinning was selected from the available methods because of its high cooling rate and the availability of the facilities at NASA Lewis Research Center.

Table 2
Atomization RST Methods

Method	Product Form and Dimensions	Cooling Rate (K/s)	Refs.
Inert Gas Atomization	50 to 100 μm spherical powder	$10^2 - 10^3$	99,108
Supersonic Gas Atomization	10 to 50 μm spherical powder	$10^5 - 10^6$	100
Ultrasonic Gas Atomization	<30 μm smooth spherical powder	10^5	109,110
Water Atomization	75 to 200 μm irregular particles	$10^2 - 10^4$	111,112
Soluble Gas Atomization	40 to 150 μm spherical powder	$10^4 - 10^5$	101,113
Drum Splat	Flakes 50 to 100 μm thick and 1 to 3 mm in diameter	$10^4 - 10^5$	104
Rotating Electrode Process (REP)	150 to 200 μm spherical powder	10^2	114
Centrifugal Atomization Process (CAP)	25 to 80 μm spherical powder	10^5	103,115
Twin Roll Atomization	Powder or flake up to 200 μm thick	$10^5 - 10^6$	116,117
Electro-Hydrodynamic Atomization (EHDA)	0.01 to 100 μm diameter powder or flake	up to 10^7	118
Spark Erosion	0.5 to 30 μm diameter spherical to irregular powder	$10^5 - 10^6$	119

Table 3
Chill RST Methods

Method	Product Form and Dimensions	Cooling Rate (K/s)	Refs.
Chill Block Melt Spinning	20 to 100 μm thick ribbon	10^5 - 10^7	120,121, 122
Planar Flow Casting	20 to 100 μm thick wide ribbon	10^5 - 10^7	123,124
Crucible Melt Extraction	20 to 100 μm thick filaments	10^5 - 10^6	106,125
Melt Drag or Overflow	Foils or filaments up to 3 mm thick	10^4 - 10^6	126,127
Pendant Drop	Filaments and fibers	10^5 - 10^6	128
Rapid Spinning Cup	50 μm thick flakes up to 50 mm diameter	10^6	129,130
Laser Glazing	Surface treatment up to 1000 μm thick	10^5 - 10^{12}	102
Twin Piston	50 to 300 μm thick discs	10^4 - 10^6	131,132

2.5.2 Chill Block Melt Spinning

Figure 12 shows a schematic of the chill block melt spinning technique along with some of the additional instrumentation used on the melt spinning rigs at NASA Lewis Research Center. The material is heated in a crucible to the desired temperature by induction heating. Some recent advances have allowed for the modification of the apparatus to allow arc melting of higher melting point materials (133). Typical crucibles used for this technique include quartz, alumina, zirconia, and graphite. The molten material is ejected from the orifice in the bottom of the crucible by pressurizing the crucible with a gas. The stream of molten metal impinges on a rotating metal wheel. The wheel is usually copper or another high thermal conductivity material. Typical wheel surface speeds used range between 5 m/s and 40 m/s. Heat is extracted from the molten metal primarily through conduction into the wheel substrate and convection into the gas surrounding the wheel when an atmosphere is present. Some radiative cooling also occurs.

The melt spinning technique can regularly produce long lengths of filaments ranging from a few micrometers thick to several millimeters thick. Width is determined by the material and the orifice size and shape. The use of planar flow techniques and multiple orifices has allowed the casting of widths many centimeters wide (123,124).

Cooling rates for melt spinning techniques are between 10^6 and 10^7 K/s (120,121,122). From analysis of the dendrite arm spacings at known slower cooling rates, the solidification rates can be extrapolated to these higher cooling rates. Analysis suggests that solidification rates are on the order of 1 to 10 m/s for some Al-Cu alloys (134).

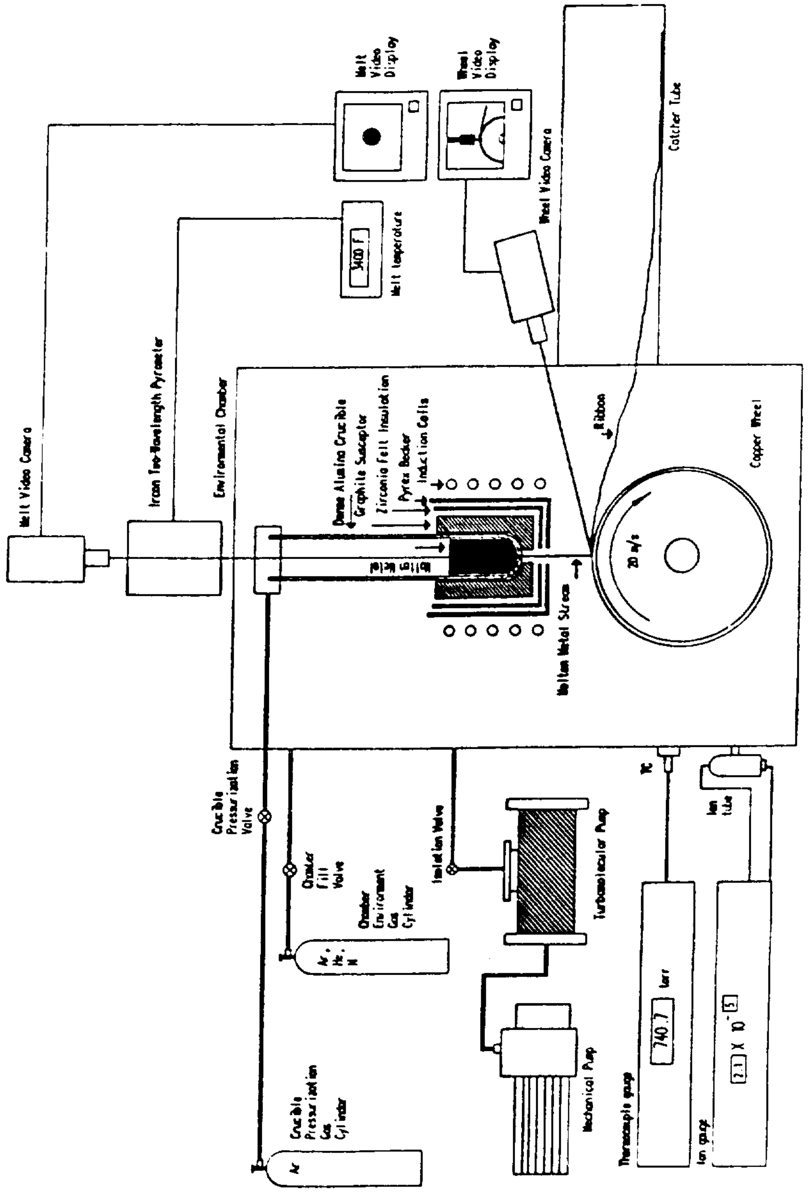

Figure 12 - Schematic Diagram of NASA Lewis Research Center Chill Block Melt Spinning (CBMS) Facility

2.5.3 Advantages of RST Processing

Rapid solidification offers many advantages over conventional casting technology. In some cases, such as metallic glasses, RST is the only way to produce certain unique microstructures. For more conventional alloys, RST offers the advantages of lowered segregation, increased solute in supersaturated solid solutions, and improved mechanical properties.

Fleming (134) examined the segregation of Cu in Al-4.5% Cu alloys at cooling rates ranging from 10^{-6} K/s up to 10^9 K/s. For materials cooled at 10^6 K/s or higher, a cooling rate typical of chill block melt spinning, Fleming observed no segregation of the Cu in the alloy compared with severe segregation in slower cooling rates typical of conventional casting techniques, i.e. 1 K/s.

Rapid solidification also offers the advantage of extending the limits of solid solubility for many systems. The increased concentration of solute allows for the formation of more precipitates during subsequent aging heat treatment. The increased volume fraction of precipitates leads to significantly higher strengths as explained in Section 2.2.2. Table 4 shows the extent to which the solid solubility of elements in a variety of Al-based alloy systems can be increased.

Better mechanical properties are also obtained for many materials produced through rapid solidification. Besides increased strength through an increased volume fraction of precipitates, the alloys benefit from decreased segregation and finer grain sizes. The refinement in grain size greatly increases the material's properties through a Hall-Petch type of relationship. Table 5 lists the improvements in mechanical properties of several Al-Li alloys achievable through rapid solidification. Table 6 lists some improvements in elevated temperature properties of Al-based alloys achieved through rapid solidification.

Table 4
Increased Solid Solubility Limits For A Variety of Binary Al-Based Alloy Systems Achievable Through RST Processing

Solute	Equilibrium Solubility Limit (a/o)	Extended Solubility Limit (a/o)	Ref.
Cu	2.5	17-18	135
Fe	0.025	4-6	
Mn	0.7	6-9	
Ni	0.023	1.2-7.7	

Table 5
Improved Mechanical Properties For a Variety of Materials Achieved Through RST Processing

Alloy	Processing Technique	Yield Strength (MPa)	Elongation (%)	Ref.
Al-1 Li-0.6 Mn	I/M	342	1.4	136
	P/M	437	4.0	
Al-1 Li-1 Cu-0.1 Zr	I/M	503	4.0	137
	P/M	443	7.3	
	F/M	490	4.2	
Al-9.7 Li	F/M	296	5.5	138
Al-10.6 Li-0.3 Co	F/M	296	8.3	138

I/M - Conventional ingot processing
P/M - Powder metallurgy processing
F/M - Flake processing

Table 6
Improved Mechanical Properties For a Variety of Materials Achieved Through RST Processing

Alloy	Temperature (°C)	Yield Strength (MPa)	Elongation (%)	Refs.
Al-8 Fe-4 Ce	24	457	8	139
	150	449	N/A	
	230	391	N/A	
Al-8 Fe-2 Mo	24	415	>2.7	139
	150	374	N/A	
	230	331	N/A	
2024 - T8*	24	400	5	139
	150	324	N/A	
	230	331	N/A	

* - Produced by conventional casting

2.5.4 Consolidation Techniques

Normally rapid solidification processing produces material forms that are not suitable for use as is. Instead the material must be consolidated into a useful form, often through P/M processing.

The atomization and some of the chill methods produce fine particulates suitable for consolidation. Other techniques such as chill block melt spinning produce product forms that require further processing. Often these large pieces of material are chopped up into flake product. Several methods are available, but some type of rotating cutting mill is frequently employed (99,106).

Once the materials are in suitable form, a variety of P/M processing techniques can be used to produce the desired shape. Hot pressing, cold pressing and sintering, hot isostatic pressing (HIPing), and extrusion are some of the more common techniques used to consolidate the materials (140).

The primary problem with the various consolidation processes are the degradation of the rapidly solidified microstructure brought on by thermomechanical processing during consolidation. Heating of the material can lead to devitrification of metallic glasses into crystalline materials. Working the material with a heating step can produce recrystallization and grain growth. Precipitate coarsening in some materials can also degrade mechanical properties significantly.

2.6 Electrical Resistivity and Thermal Conductivity

One characteristic common to all metals is their good electrical and thermal conductivity compared with most materials at room temperature. These good conductivities are a manifestation of the electron cloud within the material. The comparatively easy movement of the electrons through the material allows the electrons to move both thermal and electrical energy through the material rapidly.

For this study it is important to understand the relationship between electrical resistivity and thermal conductivity since the thermal conductivity is the desired value but the electrical resistivity is the more easily measured experimental value. Using the Wiedmann-Franz Law one can convert between these two values easily.

It is also important to understand the effect additions to the alloy have on the electrical resistivity and thermal conductivities. Of particular interest are the relation between solute atoms in solution, precipitates, and the effect of aging on conductivity.

Finally, temperature plays a major role in determining the conductivity of a material. The role of temperature will be examined to show the interrelationship between electrical resistivity and temperature.

2.6.1 Wiedmann-Franz Law

Thermal conduction through a metal occurs by one of two means; propagation of phonons through the metal or movement of free electrons. While the contribution of phonons to conduction is significant in insulators and semiconductors, the contribution in metals with their highly mobile free electrons tends to be minimal and can be ignored. Geiger and Poirier (141) detail the development of the equations defining quantitatively the thermal conductivity of metals and the Wiedmann-Franz Law which relates the thermal conductivity to electrical resistivity.

In metals with high conductivity the electrons form an electron gas that transfers heat through the metal. The electron gas obeys the laws of quantum mechanics, so the electronic contribution to the total heat capacity of the metal can be calculated using the equation

[61]

$$C_{v,el} = \frac{\pi^2 n_e \kappa_B^2 T}{2\epsilon_F}$$

where

$C_{V,el}$ = electronic heat capacity (J/cm^3)

n_e = number of free electrons per cm^3

κ_B = Boltzmann's constant (1.38062 X 10^{-23} J/K)

T = temperature (K)

ϵ_F = Fermi energy of the metal

The average velocity of an electron is related to the Fermi energy of the metal by the equation

[62]
$$\overline{V}_F = \sqrt{\frac{2\epsilon_F}{m_e}}$$

where

$\overline{V}_F$ = average velocity of the electrons

m_e = electron mass (9.1096 X 10^{-31} kg)

Knowing the heat capacity of the material and the average velocity of the electrons, the contribution of the electrons to the total thermal conductivity of the metal can be calculated using the general equation for thermal conductivity

[63]
$$k = \frac{\sum_{x=1}^{n} C_v \overline{V} l}{3}$$

where

n = number of components transferring heat

$\overline{V}$ = average velocity of component transferring heat in direction of heat flow (in this analysis equal to $\overline{V}_F$)

l = mean free path

Substituting appropriately, the conductivity of a metal due to the electrons is given by the equation

[64]
$$k_{el} = \frac{\pi^2 n_e \kappa_B^2 T \lambda_{el}}{3\sqrt{2m_e\epsilon_F}}$$

or

[65]
$$k_{el} = \frac{\pi^2 n_e \kappa_B^2 T \lambda_{el}}{3 m_e \bar{V}_F}$$

Since the most of the conductivity of a good metallic conductor such as copper comes from the electrons, there should be a proportional relationship between the thermal and electrical conductivities of a metal. The relationship is given by the Wiedmann-Franz Law. The constant of proportionality is the Lorentz number, L. L is given by the equation

[66]
$$L = \frac{k_{el}}{\sigma T} = \frac{\pi}{3}\left(\frac{\kappa_B}{e}\right) = 2.45 \times 10^{-8} Watt - ohm/deg^2$$

where

σ = electrical conductance of the material (Siemens/cm)

The Lorentz number varies from metal to metal, but in the ideal case the calculated value of L is equal to 2.45 X 10^{-8} Watt ohm/deg^2. The deviation from this ideal Lorentz number is an indication of the contribution of phonons and other thermal energy carriers to the thermal conductivity of a metal. Pure copper is closest to the ideal Lorentz number with a measured value of 2.23 X 10^{-8} watt ohm/deg^2 (141). Tungsten has the greatest deviation from the ideal Lorentz number with a measured Lorentz number of 3.04 X 10^{-8} watt ohm/deg^2 (141)

The Wiedmann-Franz Law ignores the effects of microstructure. As such, it is best applied directly to single crystals. For more complex microstructures, a combination of thermal conductivity and electrical resistivity measurements are required to determine the Lorentz numbers of the materials. If one knows the Lorentz number for samples with similar microstructures the values calculated for the thermal conductivity are valid. Otherwise there is a certain amount of uncertainty in the conversion between the electrical resistivity and thermal conductivity values.

2.6.2 Experimental Measurement of Electrical Resistivity and Thermal Conductivity

One method of measuring the thermal conductivity of a material is to induce a thermal gradient across a length of the material and observe the size of the gradient for known input levels of thermal energy. Siu, Carroll, and Watson (142) used such a device to measure the thermal conductivity of six copper alloys.

Unfortunately, this method requires a moderately large sample with a uniform cross-section. The utilization of melt spinning to produce the material for this study precluded the use of this type of direct measurement. Instead electrical resistivities can be measured and the Wiedmann-Franz Law applied to convert the values into thermal conductivities.

Resistance measurements are done using the four point probe resistance measurement technique. Two probes are attached to the ends of the sample. These probes provide a controlled amount of current through the sample. Two other probes are placed a specific distance apart between the probes supplying the current. These probes are used to determine the voltage drop across the length of material. The voltage drop and current measurements are converted into resistance using Ohm's Law (143)

[67]

$$R = \frac{V}{I}$$

where

R = resistance (ohms)

V = voltage drop (volts)

I = current (amps)

The four point resistance measurement method has a major advantage for work involving small resistances. The method is insensitive to the resistance of the leads. This is a critical point since the resistance of the probe leads tends to be orders of magnitude greater than the resistance of the samples, particularly for long probes such as those used in this study.

The measured electrical resistance values are normalized to take into account the cross sectional area of the sample and distance between the probes to calculate the resistivity of the material to give the electrical resistivities of the samples. The resistance is also converted into electrical conductivity, the reciprocal of resistivity, using the formula

[68]
$$\sigma_e = \frac{l}{Rwt}$$

where

σ_e = electrical conductivity (Siemens)

l = distance between probes measuring voltage drop (cm)

w = width of sample (cm)

t = thickness of sample (cm)

for samples with rectangular cross-sections. For other geometries, the cross-sectional area must be substituted for wt.

The resistivities for metals and other good conductors are on the order of μohm • cm. These values of conductivity can then be used in the Wiedmann-Franz Law to determine the thermal conductivity of the metal.

2.6.3 Effect of Solute Atoms on Electrical Resistivity and Thermal Conductivity

The role of solute atoms on the electrical resistivity of alloys depends on whether the atoms are present in solid solution or have precipitated out as a second phase. For dilute (<3 at. % solute) alloys that form a solid solution, the effect of alloying on electrical resistivity follows Matthiessen's Rule. The effect of higher concentrations of solute atoms in binary alloys depends on the formation of second phases and ordering phenomena.

Matthiessen and Vogt (144) investigated the effect of additions of small amounts of impurity solute atoms to metals in 1864. The results, similar to those shown in Figure 13, showed that the effect of the solute atoms was to introduce a temperature independent increase in the resistivity of the alloys. The amount of this increase was directly proportional to the concentration of the solute atoms.

Matthiessen expressed this generality as Matthiessen's Rule

$$\rho = \rho_I + \rho_L \tag{69}$$

where

ρ = resistivity of the alloy

ρ_I = portion of resistivity due to the impurities, also known as residual resistivity

ρ_L = portion of resistivity due to electron-phonon (lattice) interactions

This equation suggests that the resistivity of an alloy can be expressed as the sum of the electron scattering effects of the two factors. They also indicate that the addition of impurities has no effect on the temperature coefficient of the base material since ρ_I is independent of temperature. It also suggests that the residual resistivity of the material at absolute zero is only a function of the impurity content. The measurement of electrical resistivity near absolute zero and a higher temperature allows for the measurement of the impurity content of the alloy.

Deviations from Matthiessen's Rule are often observed. Bass (145) reviewed the observed deviations from Matthiessen's Rule and the explanations offered by various investigators. Andrew (146) determined that the observed deviations were dependent on the size of the samples. Surface effects lead to larger deviations from Matthiessen's Rule for thin wires compared with bulk samples.

Below 90 K, plastic deformation leads to deviations from Matthiessen's Rule. The resistivity of dislocations was originally assumed to be temperature independent. Rutter and Reekie (147) showed that in actuality the resistivity of dislocations is temperature dependent between 20 K and 90 K. This leads to deviations from Matthiessen's Rule as ρ_L is no longer a constant value. For these low temperatures, the deviation is generally between 10% and 20% of ρ_L, but for noble metals it can approach ρ_L at 77 K.

For more highly alloyed materials, the manner in which the solute is present in the alloy determines the effect of the solute atoms on electrical resistivity. If the solute atoms remain in solid solution, the resistivity of the alloys are determined by the concentrations of the solute and solvent as given by (148)

$$\rho \propto c_A \times c_B = c_A(1 - c_A) \qquad [70]$$

where

c_x = concentration of element x

because the number of scattering events from atomic disorder is proportional to the concentration of the solute.

Disordered Cu-Au alloys tend to follow this relationship well at room temperatures as shown in Figure 14. Many transition elements form extended solid solutions at elevated temperatures. Analysis of the resistivity of these solid solutions shows that the actual resistivities have unsymmetric resistivity-composition dependencies. A typical example taken from Mott and Jones (149) is shown in Figure 15 for Pd-Cu, Pd-Ag, and Pd-Au alloys. The deviation from expected behavior is often explained by energy band models (150).

If the alloys form an ordered phase such as Cu-Au alloys, the resistivity can show large deviations from the resistivity of the unordered alloys of the same compositions. Figure 16 shows the example of the ordered Cu-Au alloys at room temperature. In this a particular case the ordering of the alloys decreases the resistivity of the alloy.

For the more general case of a two phase alloy, the resistivity of the alloys in the two phase region is determined by the resistivity of the alloys with the compositions of the phase boundaries. The resistivity of the two phase alloy is given by (151)

$$\rho = X_A\rho_A + X_B\rho_B \tag{71}$$

where

X_x = volume fraction of component x

ρ_x = resistivity of component x

An example of this type of alloy system is given in Figure 17.

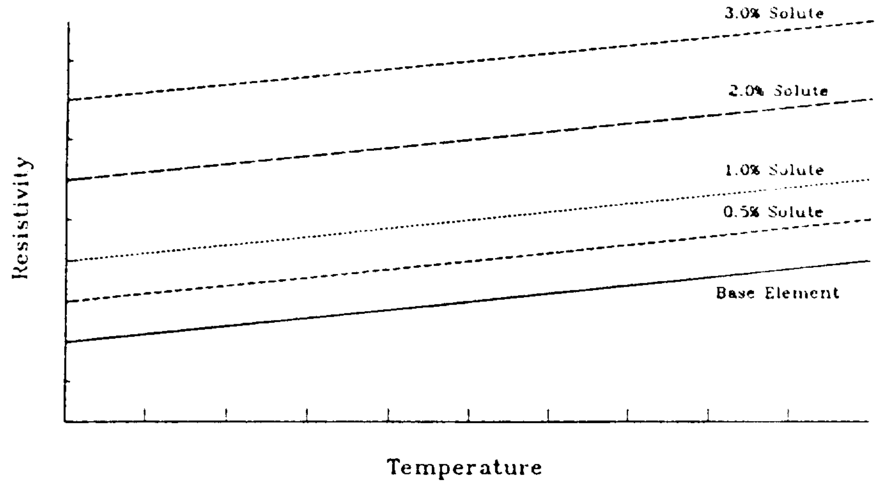

Figure 13 - Schematic Effect of Solute Atoms on Electrical Resistivity for Dilute Alloys - General Case According to Matthiessen's Law
After Matthiessen and Vogt (144)

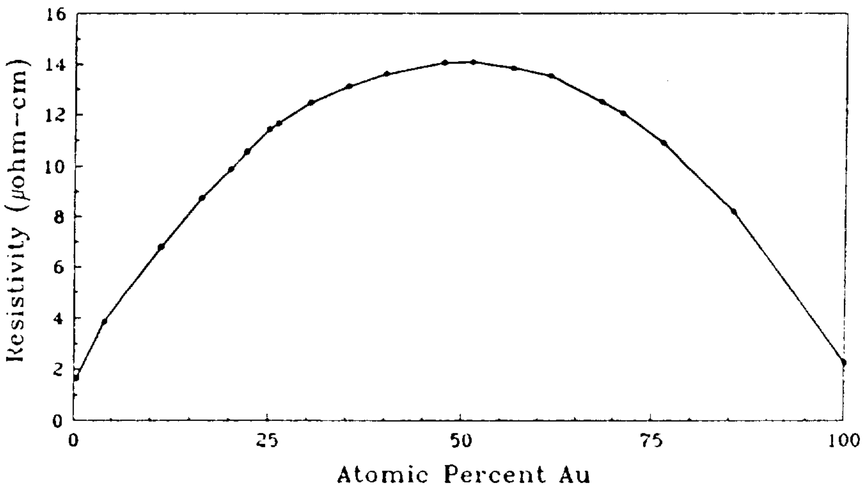

Figure 14 - Room Temperature Electrical Resistivity of Disordered Cu-Au Alloys
From Johannsson and Linde (148)

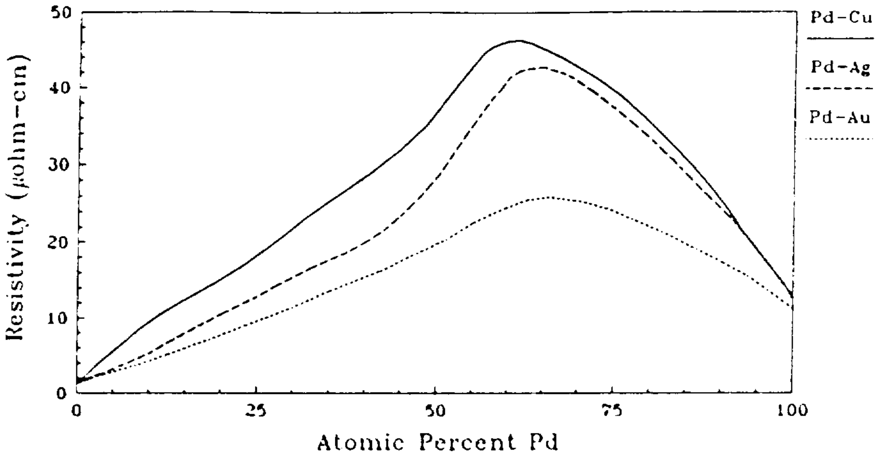

Figure 15 - Room Temperature Electrical Resistivities of Three Pd-Based Alloys From Mott and Jones (149)

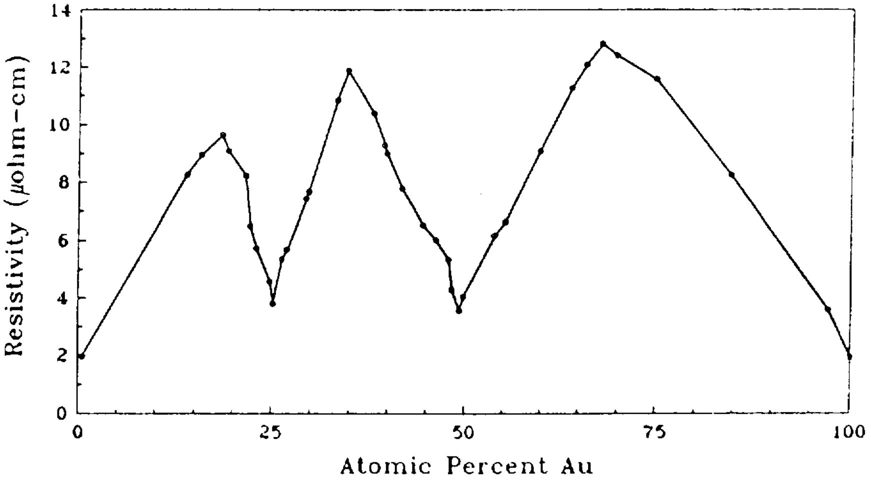

Figure 16 - Room Temperature Electrical Resistivity of Ordered Cu-Au Alloys From Johannsson and Linde (148)

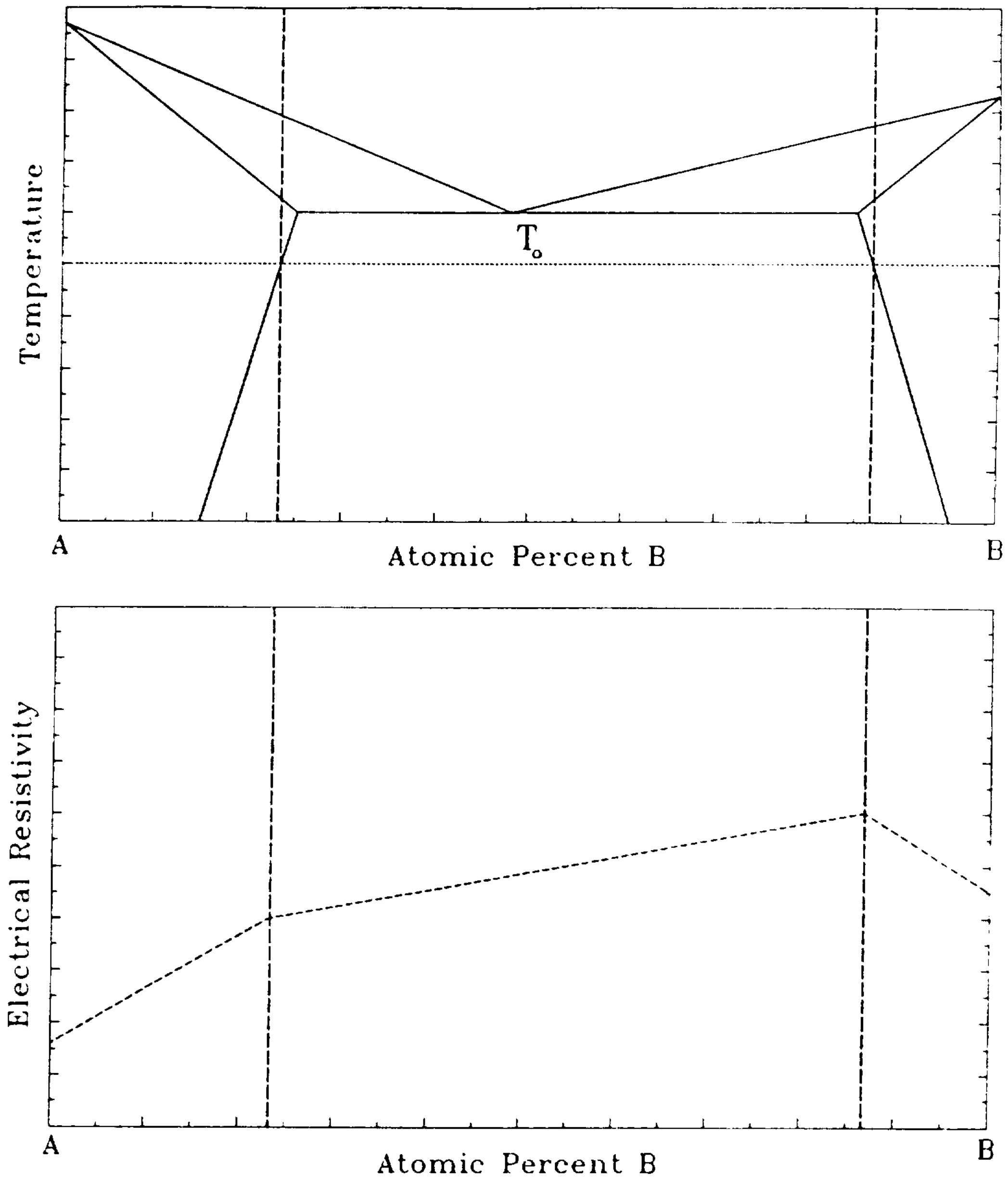

Figure 17 - Resistivity For A Simple Two Phase Eutectic As A Function Of Composition At Temperature T_0 In The Two Phase Region
After Pollock (151)

2.6.4 Effect of Temperature on Electrical Resistivity

In general, the electrical resistivity of an element or alloy increases with increasing temperature. The specifics of the dependency of the resistivity of materials on temperature is given by the Bloch-Grüneisen formula for the phonon-limited electrical resistivity case.

Bloch derived the high temperature case in 1928 (152) and the low temperature in 1930 (153). Grüneisen (154) derived empirically that the low and high temperature forms could be matched to provide the electrical resistivity of materials at all temperatures.

The Bloch-Grüneisen formula is often expressed as

[72]

$$\rho_{BG}(T) = \frac{c_1}{T}\int_0^{q_D} \frac{q^5 \mathrm{d}q}{\left[e^{\frac{\hbar C q}{k_B T}} - 1\right]\left[1 - e^{-\frac{\hbar C q}{k_B T}}\right]}$$

where

c_1 = a constant specific to the metal

q = phonon wave number lying between 0 and the Debye value q_D

C = velocity of sound in the metal

$\hbar C q$ = a long-wavelength phonon energy

If z is set equal to $\frac{\hbar C q}{k_B T}$, the Bloch-Grüneisen formula becomes

[73]

$$\rho_{BG}(T) = \frac{c_2}{\theta_D}\left(\frac{T}{\theta_D}\right)^5 \int_0^{\frac{\theta_D}{T}} \frac{z^5 \mathrm{d}z}{[e^z - 1][1 - e^{-z}]} = \frac{c_2}{\theta_D}\left(\frac{T}{\theta_D}\right)^5 J_5\left(\frac{\theta_D}{T}\right)$$

where

c_2 = another constant specific to the metal

J_5 = the Debye integral of order 5

θ_D = Debye temperature of the metal

At low temperatures, J_5 is equal to 124.4 and at high temperatures ($T >> \theta_D$) J_5 is equal to $\approx \left(\frac{1}{4}\right)\left(\frac{\theta_D}{T}\right)^4$. Substituting these values into Equation [73] yields Bloch's equations.

[74] $$\rho_{BG}(T) = \frac{124.4c_2}{\theta_D}\left(\frac{T}{\theta_D}\right)^5 \qquad T \ll \theta_D$$

[75] $$\rho_{BG}(T) = \frac{c_2}{4\theta_D}\left(\frac{T}{\theta_D}\right) \qquad T \gg \theta_D$$

The original deviation of these equations relied on several assumptions that are not fulfilled very well even for free-electron-like metals such as Na. However, the Bloch-Grüneisen formula explains the behavior of many real metals with great accuracy. This can be explained if one starts with a variational estimate of ρ through the transport electron-phonon coupling function $\alpha_{tr}^2F(\omega)$. Approximating the function as a power law yields

[76] $$\alpha_{tr}^2F(\omega) = C_n\omega^n$$

for $0 < \omega < \omega_{max}$. If n is set to 4 and taking into account $\hbar\omega_{max} = k_B\theta_D$, the variational method outlined by Kohler (155,156) and Sondheimer (157) and used extensively by Ziman (158) gives the exact same results as Equation [73]. The various complexities regarding the phonon spectrum, electron-phonon matrix elements, coupling to transverse phonons, Umklapp processes, etc., are all taken into account by the electron-phonon coupling transport function. Because the function is integrated over ω, the resistivity is determined by the gross features of the function and insensitive to the details. As a result, the assumptions made by Bloch do not have to be completely fulfilled and the results show are identical.

The Bloch-Grüneisen formula predicts that the resistivity of the Cu-Cr-Nb and Cu samples tested at room temperature and above will have resistivities that vary in a linear fashion since the test temperatures are above the Debye temperature of Cu. In most metals, i.e. Al and W, the resistivities of the metals increases by some small value as the metal expands. The expansion increases the resistivities since ρ is dependent on the volume of the material primarily through the phonon frequencies (159). The combination of the temperature dependency of ρ given by the Bloch-Grüneisen formula and the increase in resistivity with thermal expansion leads to a temperature dependency for the resistivity which has a slight positive deviation from linear.

2.6.5 Reversion Phenomena in Cu-Cr, Cu-Zr, and Cu-Cr-Zr Alloys

Reversion has been observed in Cu-Cr, Cu-Zr, and Cu-Cr alloys. The process manifests itself as an increase in the room temperature resistivity of the alloys upon reheating to a selected temperature and quenching.

In the general case, reversion is caused by the presence of metastable phases in an alloy system. The precipitation of these phases from the matrix produces a reduction in the amount of solute in solution and hence a decrease in electrical resistivity. As the samples are raised in temperature, the metastable phase becomes unstable and dissolves back into the matrix. This causes an increase in the electrical resistivity of the material. The electrical resistivity can be decreased again if another metastable or stable phase can precipitate.

Reversion for alloys that do not have metastable compounds can be induced by the thermal treatment of the material. If the material is aged at a low temperature, the critical radius for the precipitates below which the precipitates will dissolve is some value. If the temperature is suddenly increased, the critical radius increases to a value greater than the lower temperature value. Precipitates smaller than the new higher temperature critical radius dissolve back into the matrix. The electrical resistivity of the material is increased as a result. The dissolved solute will diffuse to the precipitates and allow them to grow. The decrease in solute in the matrix will decrease the electrical resistivity of the material.

Nishikawa, Nagata, and Koybashi (160) examined the reversion phenomena in a Cu-0.3 w/o Cr alloy. They aged the alloy at temperatures ranging from 300°C to 400°C followed by a water quench to room temperature. The electrical resistivity of the alloy at room temperature was then measured. The times for the heat treatments was determined by the time it took to reduce the electrical resistivity of the samples to the same value. The times are listed in Table 7.

Following these treatments, the temperatures of the samples were raised to 400°C, 450°C, and 500°C to induce reversion of the alloys. The electrical resistivity and the hardness of the samples were measured after quenching back to room temperature.

The results indicate that the samples underwent reversion when aged at 300°C and 350°C, but they did not show discernible reversion after aging at

400°C. The hardness measurements of the samples showed a very slight dip during reversion, but the values are so small that they fall within the scatter of the measurements.

The results display several trends. For a given aging temperature, the degree of reversion increases with increasing reversion temperature. In example, the increase in electrical resistivity after aging at 300°C is greatest in magnitude and fastest in time to peak increase in resistivity for the reversion treatment at 500°C. For a given reversion temperature, the magnitude of the electrical resistivity increase is greatest for the lowest temperature, 300°C.

The test was repeated for the same samples to evaluate the effect of multiple aging and reversion treatments. The results followed the same basic trends as outlined above, but the magnitude of the reversion decreased with each treatment and was assumed to cease after a finite number of cycles.

Suzuki, Kitano, and Kanno (161) examined reversion in Cu-Zr and Cu-Cr-Zr alloys as well as Cu-Cr alloys. Three compositions were used; Cu-0.26% Cr, Cu-0.30% Zr, and Cu-0.12% Zr-0.28% Cr.

For the Cu-Cr alloy, the reversion phenomena was observed continuously from 300°C to 500°C following aging at 300°C and 500°C. This result is in conflict with Nishikawa, Nagata, and Koybashi. The other general trends observed by Nishikawa, Nagata, and Koybashi are, however, followed. Since split aging cycles can affect the size, distribution and number of vacancies and other sites for heterogeneous nucleation, samples were tested following aging at 300°C for 50 hours plus 350°C for 50 hours. The results show a slight decrease in the magnitude of the reversion but virtually no change in the reversion rate compared to a sample aged at 350°C for 50 hours.

For the Cu-Zr alloy, the reversion phenomena was observed for the Cu_3Zr precipitates. The general trends were that the magnitude and rate of reversion increased with increasing reversion temperature. Increasing the initial aging temperature decreases the amount of reversion observed. Split reversion treatments where the samples were pre-aged at 300°C for 50 hours followed by 350°C for 50 hours indicated that the reversion rate and magnitude was greater than for samples aged isothermally at 350°C for 50 hours. The other trends observed for the isothermally aged samples were followed for the split aged samples. The magnitude of the reversion for the Cu-Zr alloy was considerably less than that for the Cu-Cr alloy studied.

The Cu-Cr-Zr alloy was tested following isothermal and split aging treatments. The results show that reversion occurs, but the magnitude of the reversion is somewhat greater than that for Cu-Cr and the rate is slightly slower. The effect of split aging on the reversion of the Cu-Cr-Zr alloy was to increase both the magnitude and rate of the reversion. This is in contrast to the results for Cu-Cr but is consistent with the Cu-Zr results. The difference observed is thus a manifestation of the changes experienced by the reversion of the Cu_3Zr.

Suzuki, Kitano, and Kanno also plotted the change in resistivity of the samples with respect to reversion temperature for each of the aging temperatures. If a metastable phase equilibrium line is crossed, there should be a discontinuity in the curves. The results show no discontinuities. The conclusion can thus be drawn that there are no metastable phases for the Cu-Cr-Zr alloy up to 650°C.

From these studies the possibility for reversion in Cu-Cr-Nb alloys exists, particularly for alloys rich in Cr.

Table 7
Times Required to Reduce the Electrical Resistivity of Cu-0.3 w/o Cr Alloy to the Same Value for Various Aging Temperatures
From Nishikawa, Nagata, and Koybashi (160)

Aging Temperature (°C)	Aging Time (min)
300	3000
350	300
450	45

2.6.6 Electrical Resistivity and Thermal Conductivity of Various Materials

The electrical resistivities and thermal conductivities for a variety of materials are summarized in Figures 18 and 19.

The values for the electrical resistivity and thermal conductivity show that Ag, Cu, Au, and Al are the best conductors of electrical and thermal energy. The other metals have significantly lower conductivities with heavily alloyed materials having the lowest conductivities.

Figure 19 shows that the alloys such as the stainless steels that would normally be used for applications where moderate strength at 500°C (932°F) is required have thermal conductivities that are one to two orders of magnitude less than pure Cu and high conductivity alloys. For applications such as rocket nozzles where the transfer of heat through the material is critical to control the temperature these lower thermal conductivities preclude the use of these alloys.

Instead alloys of Ag, Cu, Au, and Al must be considered. Al-based alloys melt at too low of a temperature for use in rocket nozzles. Au-based alloys are too dense for use in applications where weight is a prime concern. Ag-based alloys normally have a lower specific thermal conductivity, cost more, and melt at lower temperatures than Cu-based alloys. This makes Cu-based alloys the best candidates for rocket nozzle applications.

An examination of the various Cu-based alloys reveals that the best combination of conductivity and strength is achieved through dispersion strengthening and precipitation hardening as shown in Figure 2. By utilizing precipitation strengthening, it is possible to tailor properties as desired for the fabrication and use of the alloy as is done with other precipitation strengthened alloys. In this manner it is possible to form a soft material and harden it for use in the part. For dispersion strengthened materials, this is not possible since the dispersoid phase can not be dissolved into the matrix. There is also the possibility of seriously degrading the thermal conductivity of the Cu matrix by the introduction of other elements from the dispersoid into the matrix. This is a particular concern with oxides since even small amount of oxygen are particularly harmful.

Based on these considerations the decision was made to pursue development of a precipitation strengthened Cu-based alloy.

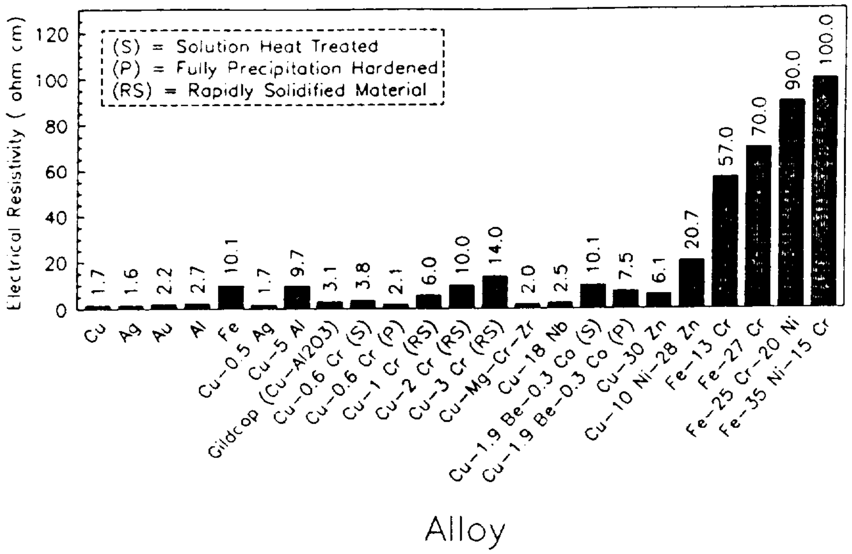

Figure 18 - Electrical Resistivities of Several Elements, Cu-Based Alloys, and Stainless Steels From References (9),(162),(163),(164)

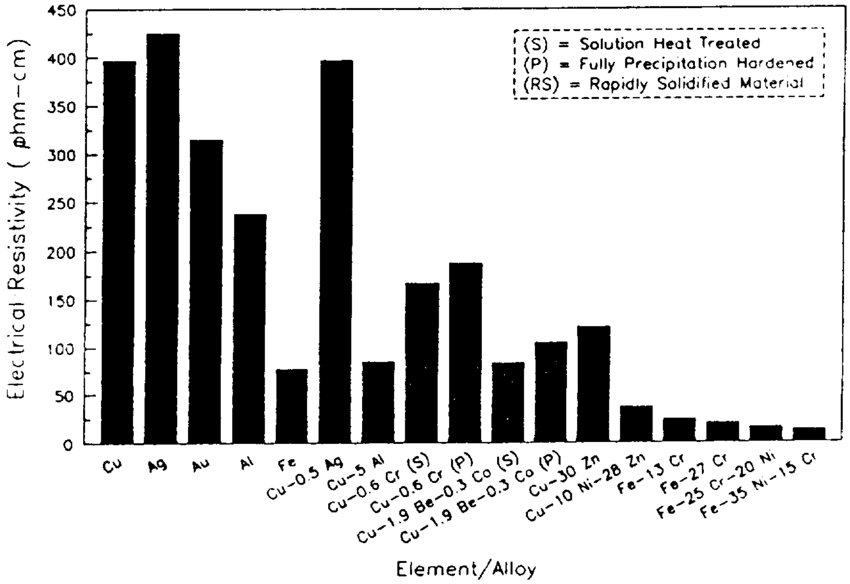

Figure 19 - Thermal Conductivities of Several Elements, Cu-Based Alloys, and Stainless Steels From References (9),(161),(163)

3 Experimental Procedure

A series of five alloys were prepared by induction melting five master alloys of the desired compositions. The master alloys were remelted and chill block melt spun to produce ribbons. These ribbons were examined in the as-melt spun and aged conditions using X-ray diffraction, optical and transmission electron microscopy, microhardness measurements, tensile testing, and electrical resistivity measurements. In addition, selected alloys were tested after consolidation to examine the microstructure and properties.

3.1 Master Alloy Melting

The alloy compositions were selected to have an atomic Cr to Nb ratio of 2 to 1, the stoichiometric ratio for Cr_2Nb. A range of alloying contents were selected to determine the extent to which the elements could be placed into a supersaturated copper solid solution.

From the available binary phase diagrams, a minimum alloying content of 2 a/o Cr and 1 a/o Nb was selected. Maximum alloying additions of 10 a/o Cr and 5 a/o Nb were selected as a composition where there should be an incomplete solid solution following melt spinning to examine the effects of overalloying and determine the maximum amount of Cr and Nb that could be placed in solid solution through melt spinning.

Alloys were given a two number designation indicating the target atomic per cent Cr and Nb respectively followed by the chemical symbol for niobium. For example, 8/4 Nb indicates that the target composition for the alloy was 8 atomic per cent Cr and 4 atomic per cent Nb.

Master alloys of the desired compositions were prepared by induction melting the materials using elemental charges. The elements were originally melted in a 18% porous Al_2O_3 crucible and cast into high SiO_2 porous Al_2O_3 tensile test bar shell molds. It was noted that the crucibles and shell molds showed evidence of reaction with the molten metal. Analysis of the oxide phase diagrams indicated that the niobium might be fluxing the Al_2O_3 and SiO_2.

Y_2O_3 was noted to form a solid when combined with Nb_2O_5 for compositions up to 50 w/o Nb_2O_5 in the temperature range of interest. To stop any possible contamination of the master metals from the crucibles and molds, the inner surfaces of both were coated with a commercial Y_2O_3 paint. The crucibles and molds were fired to produce a good bond between the Y_2O_3 and Al_2O_3. The crucibles were fired by raising the temperature 100°C (180°F) per hour to 1600°C (2912°F), held for one hour, and cooled 100°C per hour to room temperature. The same firing cycle was used for the molds, but the maximum temperature was reduced to 1400°C (2552°F) because of the lower strength at elevated temperature for the molds.

Induction melting was done under an argon cover gas to minimize Cu and Cr volatilization. The temperatures used for melting and alloying the alloys are listed in Table 8. Even with these high temperatures Nb chunks were observed in the crucible after casting in most cases. Chemical analysis confirmed that incomplete alloying occurred.

After the initial melt spin runs a different geometry for the melt spin charges was desired. To achieve a 17.8 mm (0.700-in) diameter round cross section, the samples were remelted using the same type of crucibles and cast into a copper mold. The two lowest temperature melts exhibited some sticking to the mold, so for the higher temperature melts the molds were coated with a light coat of the Y_2O_3 paint. No further sticking was observed. The chemistries of the samples were tested after remelting.

Table 8
Induction Melting Temperatures For Cu-Cr-Nb Alloys

Alloy	Temperature (°C)
2/1 Nb	1482
4/2 Nb	1593
6/3 Nb	1649
8/4 Nb	1704
10/5 Nb	1704

3.2 Differential Thermal Analysis (DTA)

Prior to melt spinning the alloys, differential thermal analysis was used to determine the liquidus and solidus of the alloys. A small sample was placed in an Al_2O_3 crucible. A thermocouple was placed in contact with a thin spot in the bottom of the crucible to measure the temperature of the sample. Another thermocouple was placed in the furnace to measure the temperature of the furnace. The furnace temperature was raised at a rate of 10°C per minute to a maximum of 1830°C. A He atmosphere was used to prevent oxidation.

Endothermic reactions would require the absorption of heat from the surrounding environment. During this time the temperature of the sample would not increase. The result would be a measurable difference between the furnace and sample temperatures. This would appear as a negative peak on a plot of the difference in temperatures versus the furnace temperature. Exothermic reactions would raise the temperature of the sample, so the opposite would be true, and a positive peak would be observed.

Samples for four of the five alloys were tested. The fifth was not tested because of problems procuring the alloy initially and the results obtained for the four alloys tested.

3.3 Chill Block Melt Spinning

Chill block melt spinning (CBMS) facilities were provided by NASA Lewis Research Center. Two rigs were used. They differed only in the size of the wheel, power supply capacity, and level of instrumentation. No metallurgical difference between the two rigs has been observed for this work or in any other alloy system produced by the rigs (165).

A schematic representation of the melt spin rig appears in Figure 12. The entire melt spin assembly is enclosed in a chamber to allow complete control of the environment. The chamber was evacuated to a pressure of less than 10^{-6} torr and back filled with Ar gas.

The master alloys were remelted in dense Al_2O_3 crucibles. Temperature was measured using a two wavelength optical pyrometer. A comparison run was made to compare the indicated temperature to the temperature measured by a thermocouple because of suspected discrepancies in the true and indicated temperatures. The results were inconclusive, but tended to indicate that the temperature indicated by the optical pyrometer was ≈167°C (300°F) higher that the actual melt temperature.

The determination of when the material was ejected for many of the runs was done by observing the melt from the top with a video camera. When the solids floating on the surface completely dissolved into the liquid the molten metal was ejected from the crucible. This consistently occurred between 1843°C (3350°F) and 1870°C (3400°F). Taking into account the suspected discrepancy between the actual melt temperature and the indicated melt temperature, these values correspond to the melting point of Cr_2Nb.

Prior to the installation of the video camera, the melts were heated to a predetermined temperature and ejected. The temperatures used are listed in Table 9. These temperatures were based on the liquidus for the Cu-Nb phase diagram plus a superheat for casting. These temperatures were later shown to be insufficient to dissolve the Cr_2Nb. Some of the testing was done on these ribbons, but those tests were repeated with materials melted at higher temperatures.

The melt was ejected from the bottom of the crucible through a 1 mm (0.040-in) diameter hole onto a copper heat sink wheel rotating with a surface speed of 20 m/s. A variety of pressures were tried, but the ejection pressure for best results was found to be between 0.0224 MPa (3.25 psi) and 0.0276 MPa (3.75 psi). The ribbon produced varied in thickness from 20 to 80 μm with the width being approximately 2.5 to 4 mm. Long lengths of continuous ribbon were easily obtained when the ribbon did not stick to the wheel and disrupt the melt puddle.

Table 9
Indicated Temperatures at Ejection for Ribbons Produced Prior to Installation of Video Camera

Alloy	Temperature (°C)
2/1 Nb	1593
4/2 Nb	1621*
6/3 Nb	1621
8/4 Nb	1645
10/5 Nb	1732*

*Reflects increased temperatures used after initial test runs

3.4 Aging Study

Since stability of the precipitates was a major concern of the study, the ribbons were aged at 500°C for times of 1, 10 and 100 hours to determine the effects of the aging on the precipitates and properties of the alloys.

Samples were aged by placing pieces of ribbons in Al_2O_3 boats. These boats were in turn placed in a quartz furnace tube. The end of the tube was sealed with a two hole rubber stopper. A long piece of stainless steel tubing allowed dry H_2 gas to be introduced into the hot end of the tube over the samples. The H_2 was extracted from the tube at the cool sealed end.

Five foot lengths of flexible tubing allowed free movement of the furnace tube into and out of the furnace. Heating and cooling times of the samples could thus be minimized by inserting the samples into a hot furnace and quenching into cold water.

The furnace was preheated to 500°C (932°F) and stabilized. Ar gas was flowed through the furnace tube at a rate of 500 cc/min for 10 additional minutes to remove most of the oxygen in the tube. H_2 was introduced at the same rate for at least 10 minutes to produce a reducing atmosphere.

The furnace tube containing the samples was inserted into the hot furnace for the desired aging time. No correction was made for the time required to reach temperature. Experience with the system used to measure resistivities of the materials at elevated temperatures indicated that the desired temperatures were reached in less than 500 seconds. Following aging, the furnace tube was immersed in cold water to quench the samples.

3.5 Consolidation of Cu-Cr-Nb Alloys

Several alloys were processed from the as-melt spun ribbon into a sheet product by a combination of hot pressing and hot rolling. The material was then tested in a manner similar to the ribbon samples to determine its physical properties. Samples of Cu made from melt spun ribbon were also consolidated by the same processing technique to provide a comparison to the Cu-Cr-Nb alloys. The consolidation processing technique is shown schematically in Figure 20.

The as-melt spun ribbons were cut into flakes using a Retsch SM-1 rotary grinding mill. This mill uses three rotary blades and four stationary blades to cut the material into small pieces. A screen in the bottom controlled the size of the material. Pieces larger than the screen opening size were retained in the cutting chamber for further cutting. A screen with an opening size of 4 mm was used for the first cut to convert the large lengths of ribbon into a more manageable size. An intermediate cut using a 2 mm screen size was used prior to the final cut with a 0.75 mm screen size. For the first and intermediate cuts material in the chamber was recovered and added back into the charge for the subsequent cut to increase the recovery rate. For the final cut only the material passing through the 0.75 mm screen was collected for consolidation.

Thirty-five and eighty gram samples were hot pressed at 650°C (1202°F) for 1 hour in vacuum at 124.2 MPa (18 ksi). A rectangular die with outer dimensions of 5.08 cm X 10.16 cm (2 in. X 4 in.) was used. A retaining ring of 0.3 cm (0.125-in.) stainless steel tubing was used to retain the material in the die during hot pressing. The tubing has several holes drilled into it to allow the entrapped gas to be removed from within the tube when vacuum was applied. Without these holes the gas retained in the tubing would have prevented the compression of the tubing and hence the compaction of the samples. To pack the powder into the die prior to hot pressing, the sample were cold pressed using a load of 200 kN (45,000 pounds). The load generated a nominal stress of 38.8 MPa (5,625 psi). The overall densities for the hot pressed samples were greater than 85% the density of Cu, but the densities of the samples were not uniform. The central regions consistently showed evidence of higher densities. The better densities were caused by the nonuniform filling of the die. The flakes were heaped in the center of the dies and could not flow to the edges during subsequent pressing.

The hot pressed Cu, 2/1 Nb, and 8/4 Nb samples were hot rolled at a temperature between 920°C (1688°F) and 940°C (1724°F) on a 2-high Fenn rolling mill with 25.4 cm (10 in.) diameter rolls to a nominal thickness between 0.50 mm (0.020-in) and 0.64 mm (0.025-in). A sample of 10/5 Nb was also hot rolled to sheet as an initial trial run, but a rolling temperature of only 850° was used. This temperature proved to be insufficient, and the rolling temperature of subsequent hot rolling operations was increased to the values given previously. To minimize internal oxidation during the first few passes, the samples were sealed in a metallic envelope made from 310 stainless steel. Ti sheet was placed in the envelopes with the samples as an O getter. The envelope was backfilled with He. After a 30% reduction in thickness, the samples were removed from the envelopes to prevent bonding of the samples to the envelope, the formation of indents and impressions on the surface of the sheets, and restraint of the sample during hot rolling. The samples were hot rolled in air to the final thickness.

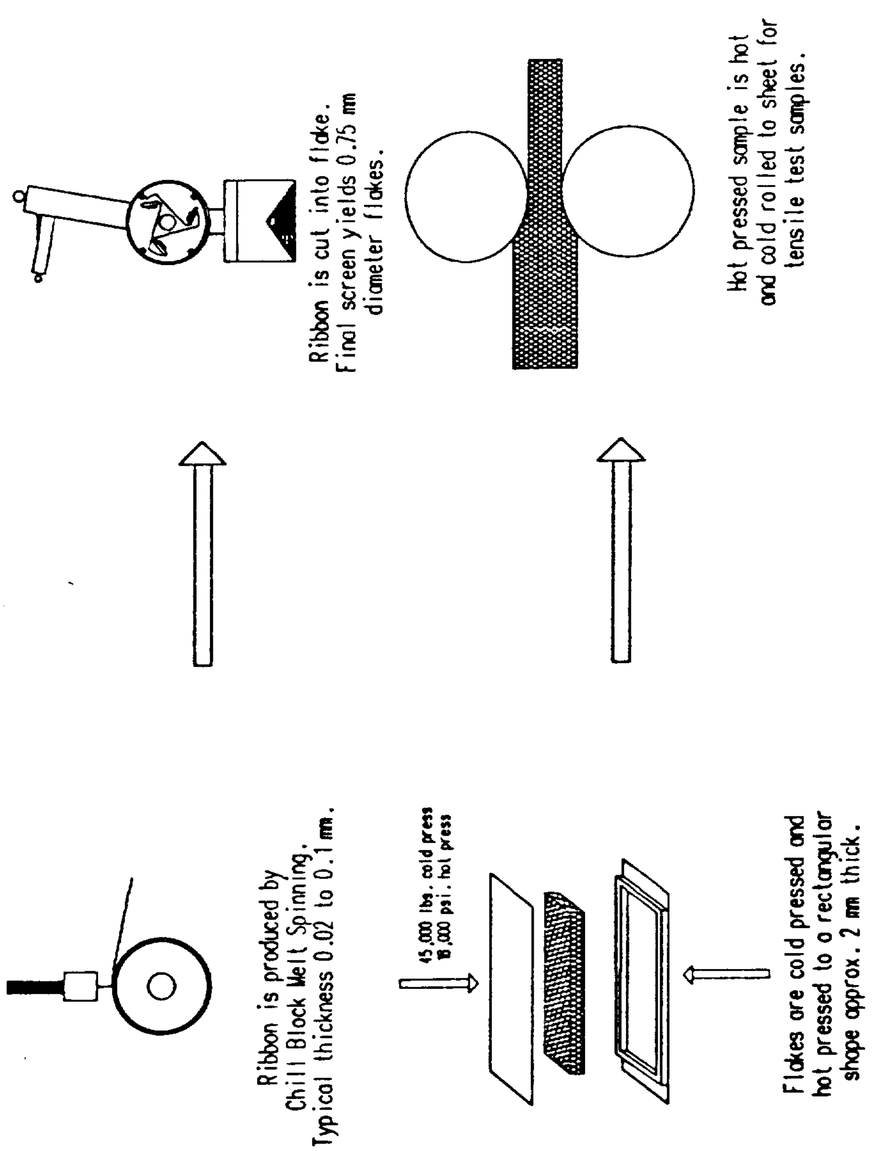

Figure 20 - Schematic Diagram of Consolidation of Melt Spun Cu-Cr-Nb Ribbons

3.6 X-ray Diffraction

As-melt spun and aged ribbons were examined by X-ray diffraction using a diffractometer to determine the phases present and the Cu lattice parameter. The ribbons were cut to fit on a glass slide and attached using double sided tape to produce a flat sample approximately 1.5 cm by 1.5 cm. Each sample was irradiated with Cu X-rays using a Ni filter. The signal was recorded by a detector attached to a computer for further analysis.

The X-ray peaks were identified for each phase that could be detected. In most cases only Cu peaks were observed. A computer program using a $\cos\theta\cot\theta$ iteration routine was utilized to determine the lattice parameter of the Cu matrix.

Four separate melt spin runs with different compositions were used to determine if there was any measurable difference in the Cu lattice parameter of the wheel side and the free side of the ribbon. The four samples indicated that the differences measured were well within the limits of accuracy of the technique used to determine the lattice parameters. In most cases the difference between the two values was less than 0.0002 nm. From this it was concluded that there was no intrinsic difference in the lattice parameter through the thickness of the ribbon and no special effort was needed to keep track of the lattice parameters of the wheel and free sides of the ribbon.

3.7 Optical Microscopy

Samples of the induction melted master alloys, as-melt spun and aged ribbons, and consolidated material were examined using optical metallography to determine their microstructure and grain size. Pieces of the induction melted master metals were cut and mounted to examine the transverse circular cross-section of the castings. Samples of the ribbon and consolidated material were mounted to examine the longitudinal cross-sections of the samples.

The ribbon and consolidated samples were polished using a Struers automated grinder using the following conditions.

For the ribbon:

Step 1: 600 grit SiC paper rotating with a speed of 150 rpm. A force of 200 Newtons was applied to the samples. A time of 30 seconds was used for the polishing step.

Step 2: 2400 grit SiC paper with the same conditions as in step 1.

Step 3: 4000 grit SiC paper with the same conditions as in step 1.

Step 4: 3μm diamond paste slurry was applied to a hard synthetic cloth. A speed of 150 rpm and a force of 200 Newtons was again used. The polishing time was increased to 60 seconds.

Step 5: 1μm diamond paste on a hard synthetic cloth using the same conditions as step 4.

Step 6: 0.05μm SiO_2 colloidal suspension applied to a synthetic chemical resistant cloth using the same conditions as step 4.

For the consolidated materials, the same basic steps were used except the following modifications were made:

Step 1: The first step was a 320 grit SiC paper. The samples were then polished as in steps 1 through 3 for the ribbons.

Step 2: A synthetic woven cloth was substituted for the hard synthetic cloth in steps 4 and 5 for the ribbons.

An etching solution consisting of 15 ml H_2O - 15 ml NH_4OH - 15 ml H_2O_2 plus 4 pellets of NaOH added last was used to etch the samples. In some cases even this relatively mild etchant produced overetching through attack of the precipitates. This was a particularly unsatisfactory problem with the most highly alloyed materials.

c - 2

The ribbons were examined at magnifications between 1000X and 1500X to see the fine grains. Differential interference contrast (DIC) was used to bring out the grains and other fine details.

3.8 Transmission Electron Microscopy (TEM)

TEM was performed on as-melt spun, aged, and consolidated samples to determine the phases present, their crystal structure, and the size of the precipitates.

A thinning solution consisting of 500 ml methanol - 200 ml 2- butyloxyethanol - 250 ml nitric acid or 200 ml nitric acid - 600 ml methanol (25% nitric) chilled to between -30°C and -50°C was used to thin the samples. The voltage was varied between 20 V and 70 V to attempt to determine the best thinning conditions. The best results were obtained for the 25% nitric acid solution chilled to -30° C or lower when a voltage of 20V to 25V was used.

Because of the extremely convoluted topography of the free side of the ribbons, the free side of the ribbons was pre-polished using 600 grit SiC paper prior to electropolishing. The samples still had a few depressions in the free side even after the pre-polish. The samples invariably thinned in these regions first. Because of the steep sides of the depressions there was only minimal thin area produced.

For the consolidated materials, the oxide layer produced by the hot rolling had to be removed. This was accomplished by abrading the surface with 180 grit SiC paper until all visible signs of the oxide were removed. The samples were mechanically thinned further with 600 grit SiC paper to a thickness of less than 0.13 mm (0.005-in). Three millimeter disks were punched from the samples for electropolishing as with the ribbons. Unlike the ribbons, the samples showed considerable thin areas.

The thin foils were examined in a Philips 400T TEM microscope with an attached EDS unit for chemical analysis of the samples. The EDS unit was upgraded to a Kevex ultrathin window EDS unit in the last few months of the study.

3.9 Microhardness Measurements

Microhardness measurements were made on the longitudinal cross-section of the as-melt spun and aged ribbons as well as the consolidated material. Microhardness measurements for the induction melted material are not reported due to extreme segregation of the alloys which lead to measurements that varied greatly depending on the phases the indenter struck. Careful positioning of the indenter on the samples did however allow for the measurement of the microhardness of the Cr_2Nb precipitates.

Knoop microhardness measurements were selected over Vickers microhardness measurements because the Knoop indenter allowed more area of the ribbon to be incorporated in the indentation. The indents are also shallower than the Vickers hardness indents. A load of 25 grams was selected since it produced an indent equal to half the thickness of the ribbons or less. A dwell time of 15 seconds was used for all measurements.

The Buehler microhardness tester used had a built-in computer for converting the size of the hardness indent to a Knoop hardness number. After the desired number of tests were completed, the computer calculated the average Knoop hardness and the standard deviation of the hardness measurements and provided a list of the measurements and statistical analysis.

3.10 Tensile Testing

Tensile testing was done for many of the alloys at room temperature and elevated temperatures. Tensile testing of the ribbons proved to be extremely difficult due to the very small cross sectional area and relatively low strength of the alloys. Tensile testing was also conducted on the consolidated materials. Samples of consolidated melt spun Cu ribbon were also tested.

To remove as much of the effects of edge roughness as possible and to impart a reduced section to the samples, the ribbons were held in a jig and the edges sanded with 180 grit SiC paper. The jig had an indent in the side that produced the reduced section. Careful manipulation of the ribbons resulted in relatively parallel edges after sanding. The width of the samples was not consistent from sample to sample due to the method for producing the reduced section. The widths of the samples ranged from 0.38 mm (0.015-in) to 1.02 mm (0.040-in). Thicknesses of the samples were determined by the thickness of the ribbons produced during melt spinning. No effort was made to remove impressions from the free surface of the ribbon.

The tests were performed using an Instron tensile test machine. A chamber with a W mesh heater enclosed the samples. A diffusion pump allowed the chamber to be pumped down to a vacuum of better than 5×10^{-5} torr for testing the samples at elevated temperatures. While not specifically designed for the low temperatures used in this study, the heater controller was able to hold the temperature of the samples within 5°C of the desired test temperatures for the duration of the tests. The temperature of the samples was measured by attaching a thermocouple to the grips so as to hang even with the midsection of the samples. Sample heat up rates were in excess of 150°C (270°F) per minute to minimize the effects of aging on the materials' properties.

A crosshead speed of 0.127 mm/min (0.005 in/min) was used for all testing. The sensitivity of the load cell was set at 9.1 kg (20 pounds) for the ribbon testing, the lowest limit available. Typical loads measured were on the order of 1 Kg (2.2

pounds). The weight of the grips was significant in these tests. The values obtained for the load at yielding and the ultimate tensile load were corrected by adding the weight of the bottom grip that was supported by the samples to the weight recorded by the load cell.

For the consolidated sheet samples, the test samples were punched out from the hot rolled sheet using a die punch. Extensive cracking of the 4/2 Nb and 6/3 Nb samples resulted in insufficient good material to produce tensile test specimens. The 10/5 Nb material also showed evidence of cracking, but two tensile test samples could be produced. Subsequent testing showed that the samples were bad, and the results of the tests were dropped. The sample geometry appears in Figure 21. Severe problems with failure of the samples in the grip areas were encountered initially. After several tests with different fixtures and test conditions, the decision was made to use the initial configuration of test fixtures which placed a pin through a hole in the grip section. To prevent the failure of the sample in this region, the grips were selectively sandblasted to remove the oxide layers and pieces of stainless steel were spot welded to the grips. The samples consistently failed in the reduced section thereafter. A photograph of a typical sample is shown in Figure 22.

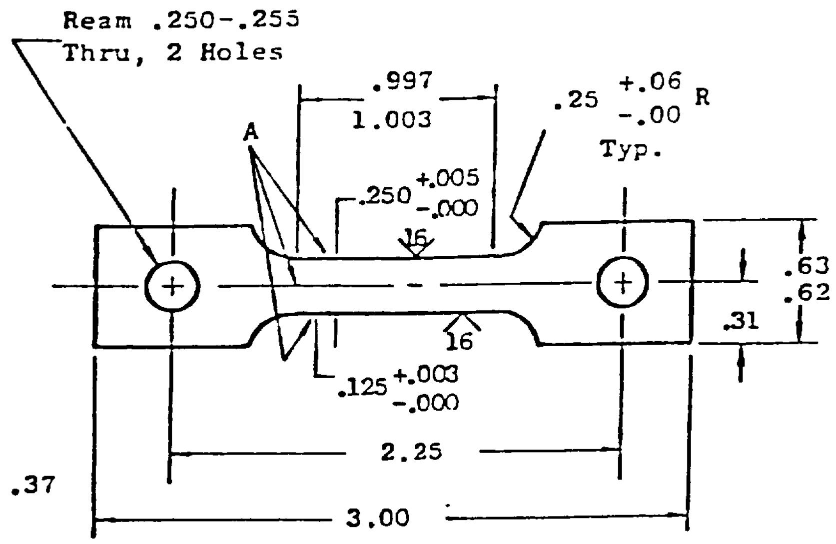

Figure 21 - Consolidated Tensile Test Sample Geometry

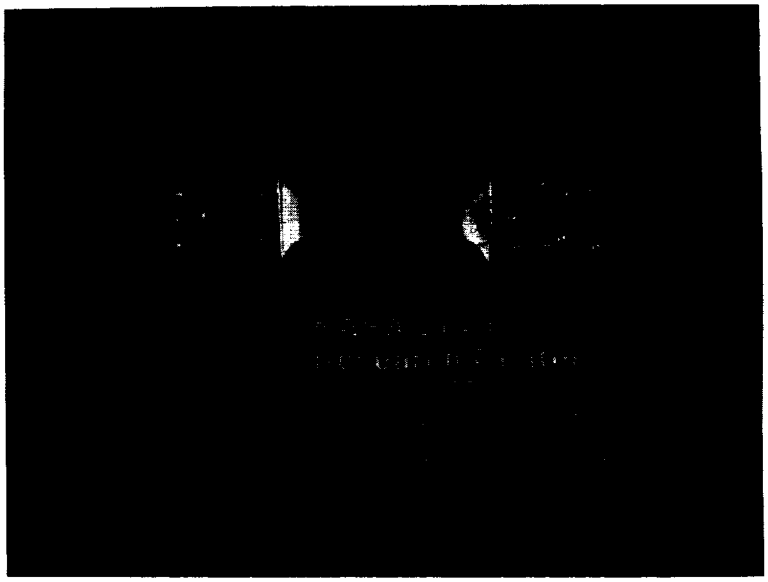

Figure 22 - Consolidated Tensile Test Sample Showing Spot Welded Stainless Steel Reinforcement Pieces on Grips

3.11 Electrical Resistivity Measurements

The thermal conductivity was determined by measuring the electrical resistivity of the materials and converting the resistivity into a thermal conductivity using the Wiedmann-Franz Law (See Section 2.6.1). A Lorentz number of 2.23 X 10^{-8} watt ohm/deg^2, the value for pure copper, was used for the conversion factor.

A schematic diagram of the resistivity measurement rig is presented in Figure 23. The original measurements of the sample resistivities was done using the 10 mA power supply of the Fluke multimeter. The small temperature gradients of the sample produced thermally induced currents as high as 2.5 mA or 25 per cent of the applied current. As a result, the original power supply was replaced by a larger power supply capable of producing up to 5.5 amps. The currents used ranged from 1.2 to 1.9 amps. The multimeter was then used to measure the voltage drop across the inner two probes. The contribution from the thermally induced current was thus reduced to 0.2% of the measured values.

For resistivity measurements at elevated temperatures the quartz tube was sealed and evacuated to a pressure believed to be in the 10^{-6} torr range. The placement of the ion gauge between the diffusion pump and the smallest orifice rather than between the smallest orifice and the furnace tube precluded the accurate measurement of the vacuum in the furnace tube. The samples were noted to be only lightly oxidized even after 100 hour exposures, so the vacuum was deemed to be good. A heat pipe provided a hot zone approximately 20 cm long. Variation of temperature in the hot zone was measured to be less than 5°C (9°F) over the entire length of the hot zone. The temperature of the sample was continuously monitored using a thermocouple placed next to the sample. Control of the temperature was provided by a thermocouple placed outside the heat pipe due to the large thermal mass associated with the heat pipe. A difference of approximately 65°C was measured between the control thermocouple and the sample thermocouple.

The width of the sample was measured using digital calipers with an accuracy of 25 μm. The thickness of the sample was measured using digital micrometers with an accuracy of 2.5μm. The micrometers had 15° pointed anvils to allow for the measurement of the thickness of the samples in depressions.

The length measurement proved to be initially inaccurate. Because of the use of alligator clips to attach the leads to the sample, there were several contact points spread out over a considerably length. It was discovered that the average length between the contacts was needed to accurately determine the resistivity of the samples. To correct for this problem, the electrical resistivity of the sample was measured at room temperature *in situ* following testing. The electrical resistivity of the sample was then immediately remeasured using clips designed to produce a point contact with the sample. By calculating the resistivity in this manner and comparing it to the measured *in situ* resistivity value, it was possible to determine the effective *in situ* length of the samples. The measured *in situ* resistance measurements could then be accurately converted to resistivities.

The voltage drop, current passing through the sample, and temperature of the sample were recorded at the rates shown in Table 10. Following the first 10,400 seconds, measurements were taken periodically up to the end of the test. The aging tests ran for a minimum of 24 hours except for the melt spun Cu which was aged for only 4 hours.

Following the isothermal aging of the sample at 500°C, the temperature of the sample was varied to determine the dependence of resistivity on temperature. The samples were heated to a maximum temperature between 550°C (1022°F) and 600°C (1112°F). Particular attention was paid to measuring the electrical resistivities in the temperature range between room temperature and 100°C and the temperature range between 475°C and the maximum temperature attained in the tests. Measurements were typically taken every 5°C during heating and cooling.

Table 10
Reading Rates for Electrical Resistivity Measurements

From (sec)	To (sec)	Readings Taken Every (sec)
0	600	15
600	1200	30
1200	1800	60
1800	10800	300

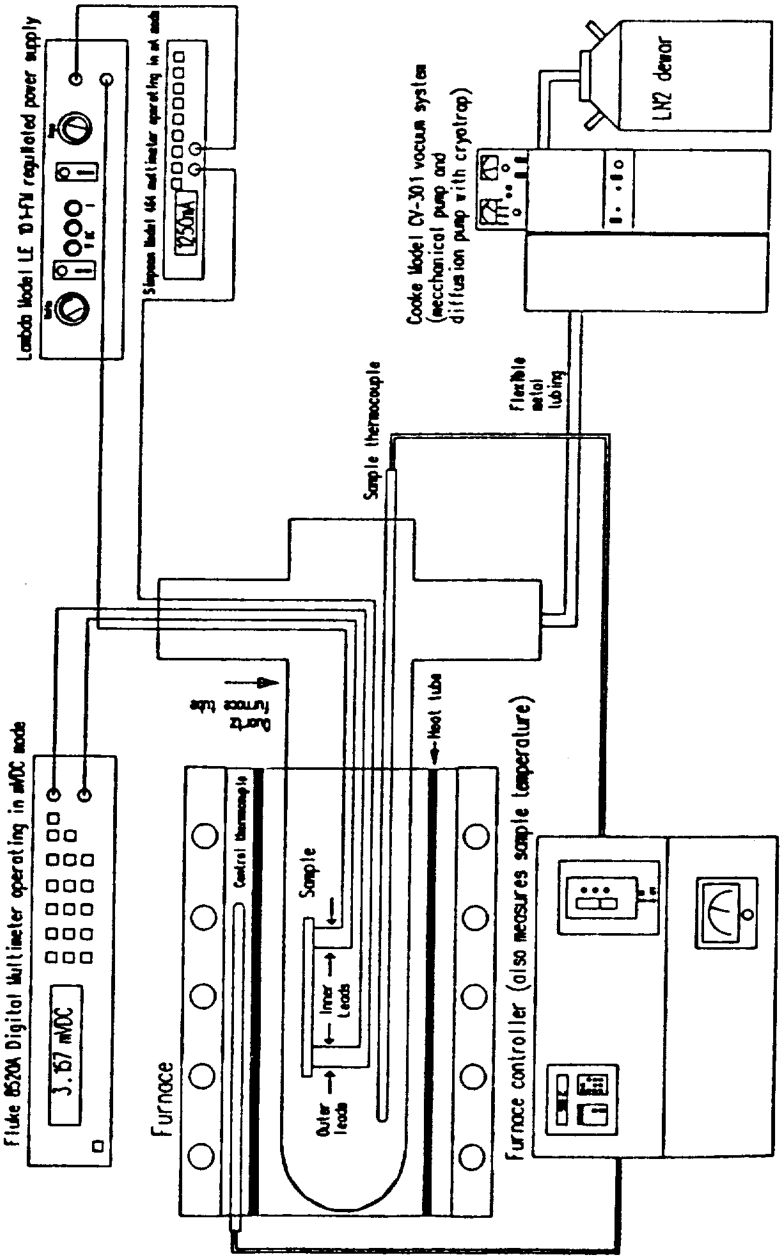

Figure 23 - Schematic Diagram of Elevated Temperature Electrical Resistivity Measurement Rig

4 Results

A description of the production of the materials in all stages; master melt, melt spun ribbon, and consolidated material; is presented. Observations from the optical and transmission electron microscopy are shown. The results from the mechanical testing and electrical resistivity measurements are also presented.

4.1 Chemical Analysis of Master Alloys and Melt Spun Ribbons

The compositions of the master alloys for the study are listed in Table 11. The Cu, Cr, Nb, and O contents are listed. More complete analyses of the materials revealed that the level of other elements was below the limits of detectability in all cases. This included Al, Si, and Y, the three elements composing the refractory materials of the crucibles and molds.

Since the materials had to be remelted for some of the work, the composition before and after remelting were tested. Differences between the two values were within the accuracy of the chemical testing methods.

Typical alloy compositions for melt spun ribbons are listed in Table 12. The composition of each run was tested, but the individual compositions did not vary greatly from the listed compositions. Indeed, for most runs of a given alloy the compositions were identical to the listed values.

The actual alloying levels were fairly close to the desired alloying levels for the 4/2 Nb, 6/3 Nb, and 8/4 Nb alloys. More importantly, these alloys have atomic ratios of Cr to Nb near 2 to 1, the ratio for stoichiometric Cr_2Nb.

The 2/1 Nb alloy had a low Nb content due to problems encountered with dissolving the solid Nb in liquid Cu. The kinetics of the dissolution proved to be slow. Higher temperatures and longer holding times cured the problem for the other alloys.

The 10/5 Nb alloy has a higher Nb content in the ribbon than the desired 5 a/o. The high Nb content and lowered Cu and Cr levels were caused by the volatilization of Cu and Cr from the melt during remelting due to the high temperatures used. Direct evidence of this was seen by examining the crucibles which had Cu and presumably Cr deposited on the cool surfaces and observations of the melt during melt spinning. Gases were observed leaving the melt at temperatures above 1760°C (3200°F). This temperature corresponds roughly to the temperatures at which the partial pressures of Cu and Cr are greater than 100 torr.

Table 11
Composition Of Cu-Cr-Nb Master Alloys

Master Alloy	Cu (w/o)/(a/o)	Cr (w/o)/(a/o)	Nb (w/o)/(a/o)	O (ppm)	Cr:Nb Ratio
2/1 Nb	97.2/97.1	1.8/2.2	1.0/0.7	16	3.1
4/2 Nb	93.8/94.1	3.1/3.8	3.1/2.1	72	1.8
6/3 Nb	88.3/90.0	4.3/5.3	7.4/5.1	180	1.0
8/4 Nb	86.0/86.5	7.2/8.9	6.8/4.7	330	1.9
10/5 Nb	86.6/87.3	6.6/8.1	6.7/4.6	340	1.8

Table 12
Typical Compositions Of Melt Spun Cu-Cr-Nb Ribbons

Ribbon	Cu (w/o)/(a/o)	Cr (w/o)/(a/o)	Nb (w/o)/(a/o)	O (ppm)	Cr:Nb Ratio
2/1 Nb	97.7/97.6	1.6/2.0	0.7/0.5	57	4.0
4/2 Nb	94.8/94.8	2.9/3.5	2.3/1.6	130	2.2
6/3 Nb	90.4/91.5	4.6/5.7	4.0/2.8	160	2.1
8/4 Nb	87.8/89.0	6.0/7.4	5.1/3.5	360	2.1
10/5 Nb	82.2/83.9	6.6/8.2	11.2/7.8	620	1.1

4.2 Differential Thermal Analysis (DTA)

Differential thermal analysis was performed on four of the five master alloys to determine the liquidus and solidus of the alloys for subsequent remelting and melt spinning of the alloys.

The DTA plots for 2/1 Nb, 4/2 Nb, 6/3 Nb, and 8/4 Nb alloys are shown in Figure 24. The 10/5 Nb alloy which had to be recast and not available until well after the other DTA tests were done was not tested because the results obtained with the other four alloys indicated that the solidus and liquidus were virtually independent of the composition. From the Cu-Cr and Cu-Nb phase diagrams a large difference in the solidus and liquidus temperatures had been expected. In the DTA plots this would have been manifested as a broad peak in the plot starting somewhat below the melting point of pure Cu, 1085°C (1985°F), and extending several hundred degrees Celsius above the solidus. Instead the DTA plots show a small peak between 1000°C (1832°F) and 1150°C (2102°F) for all the alloys with typical peak widths being approximately 50°C.

Initially this phenomena was not understood, but subsequent observations of the melt during remelting for rapid solidification showed that the Cr_2Nb

precipitates were stable in liquid Cu to temperatures above 1700°C (3092°F). The work also indicated that the majority of the Cr and Nb were present in the form as Cr_2Nb precipitates instead of being in solid solution.

The temperature range for the DTA experiments should have covered the melting of the Cr_2Nb or the dissolution and reprecipitation in the melt. The transformation of Cr_2Nb from the FCC to hexagonal phase was also hoped to be detected. The sensitivity of the measurements and the unknown value for ΔG made detection of the transformation questionable though. Even for the most heavily alloyed material tested, 8/4 Nb, no such peaks were observed.

No good explanation exists for this. Cr_2Nb was observed to dissolve into the liquid Cu above an indicated temperature of 1843°C (3350°F) during the melt spinning process. Some experiments with cycling the temperature also indicated that the Cr_2Nb reprecipitated on cooling as little as 56°C (100°F). Since the indicated temperatures are believed to be higher than the actual temperatures of the melt, the DTA experiments should have covered the temperature range of these reactions. The results must be viewed to reflect a lack of sufficient sensitivity in the DTA test itself.

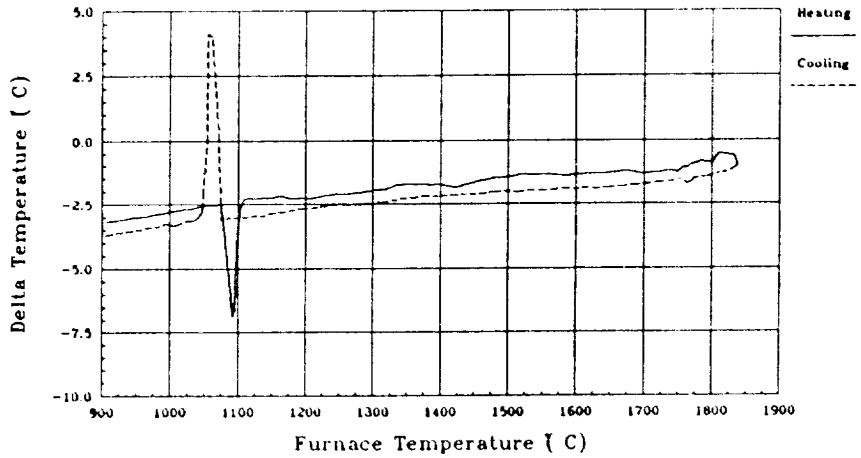

Figure 24a - Differential Thermal Analysis (DTA) Plot for 2/1 Nb

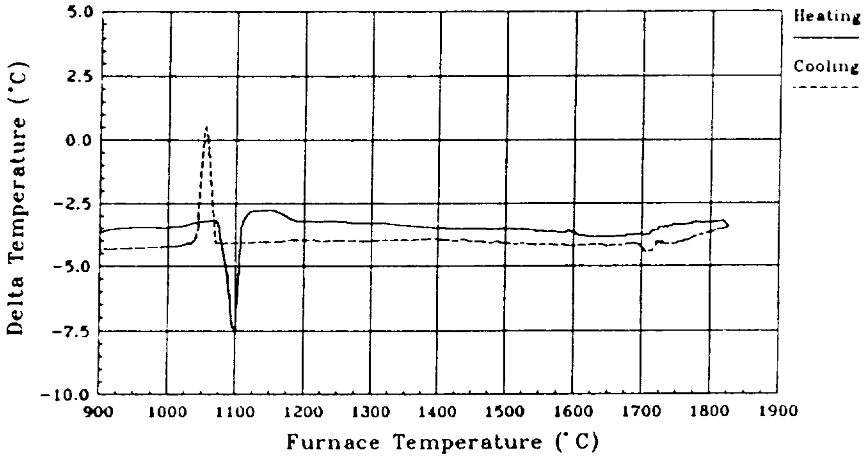

24b - Differential Thermal Analysis (DTA) Plot for 4/2 Nb

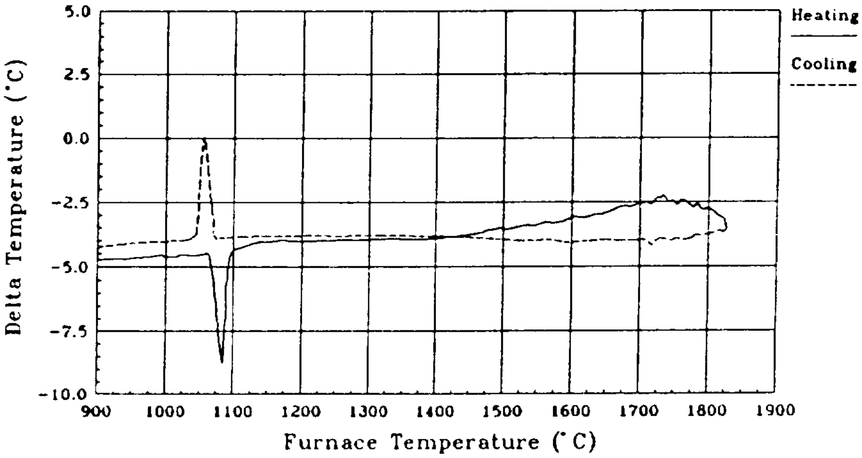

24c - Differential Thermal Analysis (DTA) Plot for 6/3 Nb

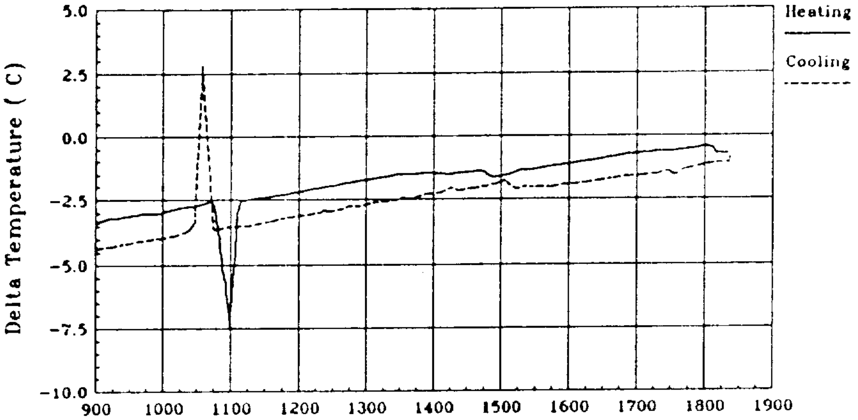

24d - Differential Thermal Analysis (DTA) Plot for 8/4 Nb

4.3 X-ray Diffraction

X-ray diffraction was performed on the induction melted master alloys, as-melt spun and aged ribbons, and consolidated material to determine the phases present and the lattice parameters of the Cu matrix.

For the induction melted master materials, the results indicated that the material contained Cu with a lattice parameter a_0 of 0.36147 nm and the low temperature FCC phase of Cr_2Nb with a lattice parameter a_0 of 0.699 nm. The measured values of the copper lattice parameter indicate that there was little or no Cr and Nb in a solid solution.

The X-ray diffraction results for the as-melt spun ribbon showed no peaks for Cr_2Nb except in the most highly alloyed cases. Even then, only the most intense Cr_2Nb peak for the high temperature hexagonal phase was observed. The relative intensity of the peak was much less than 5% of the intensity of the strongest Cu peak. The phase identification was therefore done using TEM as explained in Section 4.5.2.

The lattice parameter of the Cu matrix was measured from the observed Cu peaks. The phases detected in the aged samples showed an occasional Cr_2Nb peak, but again in most cases only Cu was detected. The Cu lattice parameter for as-melt spun and aged ribbons are shown in Table 13. Typical error values were reported to be ±0.0002 nm.

The lattice parameter of the consolidated material was 0.36147 nm±0.0002 nm.

Table 13
Average Cu Lattice Parameter For Cu-Cr-Nb Ribbons

Alloy	As-melt Spun (nm)	Aged at 500°C for: 1 hr (nm)	10 hr (nm)	100 hr (nm)
2/1 Nb	0.36174	0.36160	0.36189	0.36144
4/2 Nb	0.36202	0.36179	0.36146	0.36147
6/3 Nb	0.36195	0.36173	0.36146	0.36124
8/4 Nb	0.36164	0.36105	0.36210	0.36143
10/5 Nb	0.36169	0.36173	0.36223	0.36147

4.4 Consolidation of Cu-Cr-Nb Alloys

Optical macrographs of the flake product for each of the five alloys plus melt spun Cu appear in Figure 25. The optical macrographs of the flakes were used to determine the maximum diameters of the flakes. Plots of the maximum diameter size distribution and the cumulative percent of the maximum diameters appear in Figure 26. Flakes larger than the 0.75 mm final screen size occur when long, thin flakes are able to get through the screen opening. Aspect ratios for the flakes smaller than 0.75 mm tended to be near 1 though no quantitative measurements were made. The larger flakes had an aspect ration approximately equal to their maximum diameter divided by 0.75 mm.

The density of the materials was calculated assuming that the materials formed stoichiometric Cr_2Nb. Since no values for the density of Cr_2Nb were available in the literature, the density of Cr_2Nb was calculated based on the volume of the unit cell and the atomic weights of the elements to be 8.09 g/cc. Using the weight of Cr_2Nb and Cu in the materials of the nominal compositions, the densities of the materials, and the total weight and volume of the materials, the volume percent Cr_2Nb and the densities for samples of the nominal compositions were calculated. The results appear in Table 14. The actual values for the densities are slightly higher while the volume percentages of Cr_2Nb are slightly lower.

The overall densities of the hot pressed plates were ≈85% of the theoretical density of the alloy. As is shown in Figure 27, the densities of the plates were far from uniform. The estimated density of the plates range from <70% for the edges where flakes were readily visible to near 100% in the central portions of the plates.

During hot rolling, it was observed that major cracks appeared in the first few passes in the low density regions and propagated inward. This proved to be the greatest problem for the consolidated materials. The cracks made tensile testing inaccurate. The electrical resistivity measurements were not as severely affected since crack free regions could be selectively tested.

The other problem encountered during hot rolling was internal oxidation. The expectation was that reducing the thickness of the material 30% would seal the material completely and allow for the removal of the material from the protective envelope. This last step was needed to allow the material to elongate during the rolling process without restraint from the undeformed envelope. Instead the material, particularly the 8/4 Nb showed evidence of large open areas and internal oxidation. The oxide was incorporated into the material as the samples were hot rolled. Examples of this are shown in Figures 28 and 29.

Because of these problems, the results for the tensile testing of the consolidated materials for the ultimate tensile strength and ductility represent lower limit bounds. Material that had been hot pressed to a higher, more uniform density and hot rolled in a manner to prevent the formation of internal oxides would be expected to have significantly better mechanical properties.

Table 14
Theoretical Densities of Cu-Cr-Nb Alloys and Volume Percentages of Cr_2Nb

Alloy	Density (g/cm^3)	Volume Percent Cr_2Nb
Cu	8.92	0
2/1 Nb	8.89	3.37
4/2 Nb	8.86	6.57
6/3 Nb	8.83	9.64
8/4 Nb	8.81	12.56
10/5 Nb	8.78	15.36

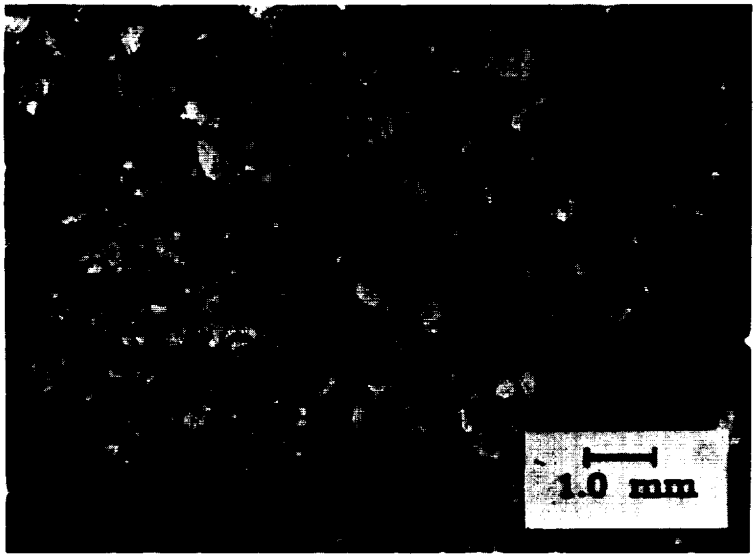

Figure 25a - Optical Macrograph of Cu Flakes Produced by Rotary Mill

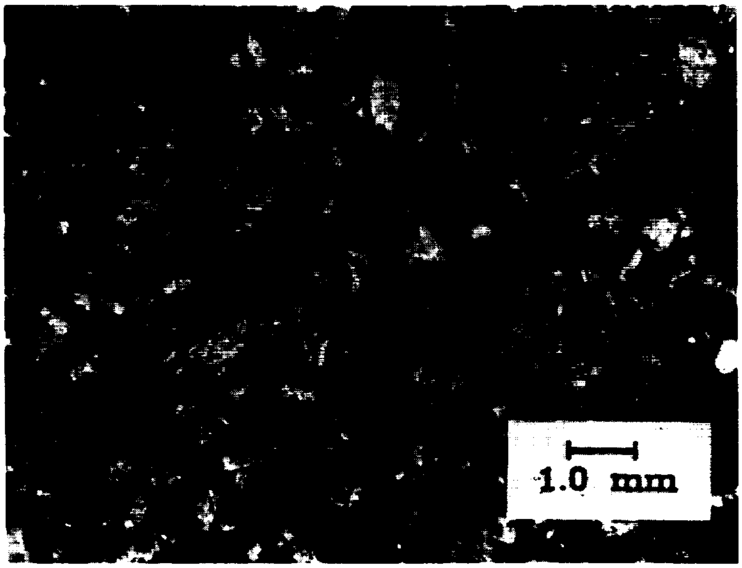

25b - Optical Macrograph of 2/1 Nb Flakes Produced by Rotary Mill

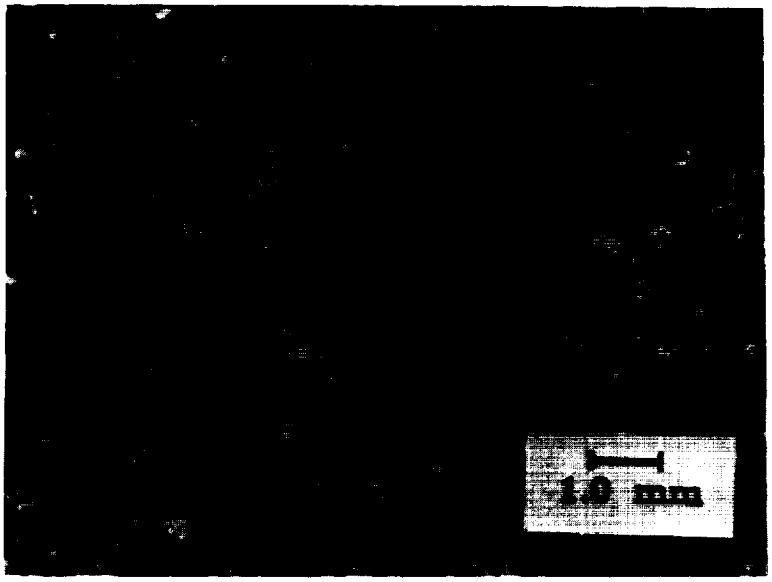

25c - Optical Macrograph of 4/2 Nb Flakes Produced by Rotary Mill

ORIGINAL PAGE
BLACK AND WHITE PHOTOGRAPH

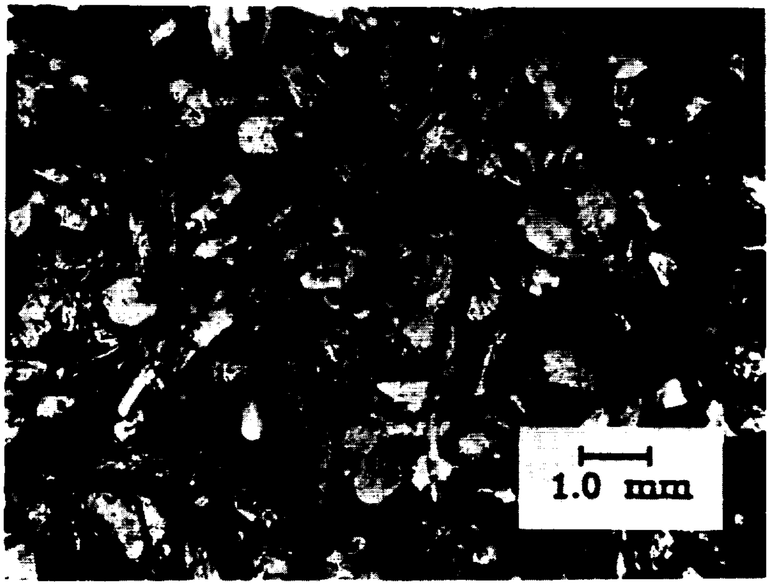

25d - Optical Macrograph of 6/3 Nb Flakes Produced by Rotary Mill

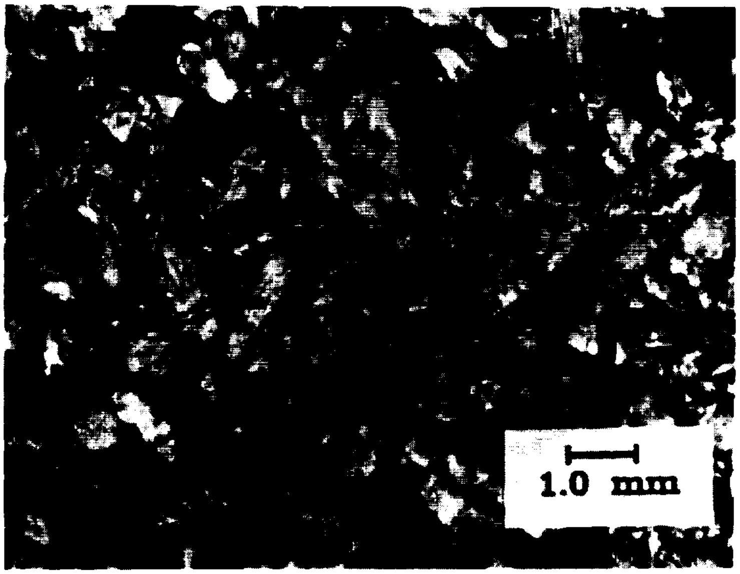

25e - Optical Macrograph of 8/4 Nb Flakes Produced by Rotary Mill

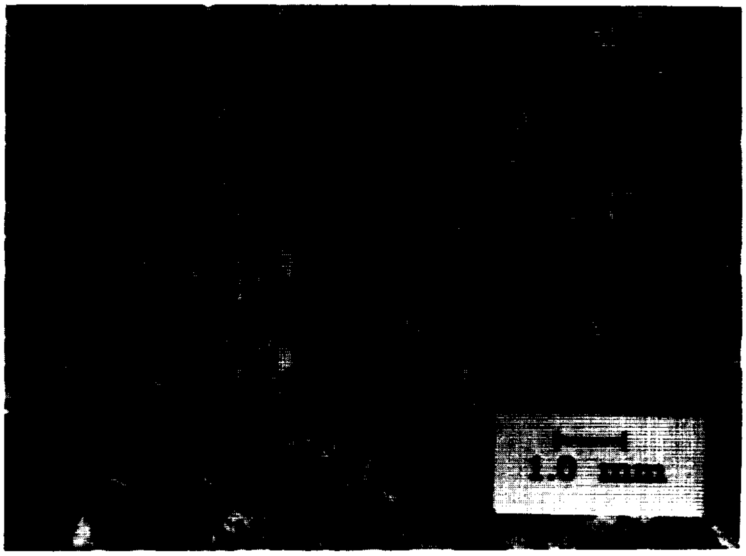

25f - Optical Macrograph of 10/5 Nb Flakes Produced by Rotary Mill

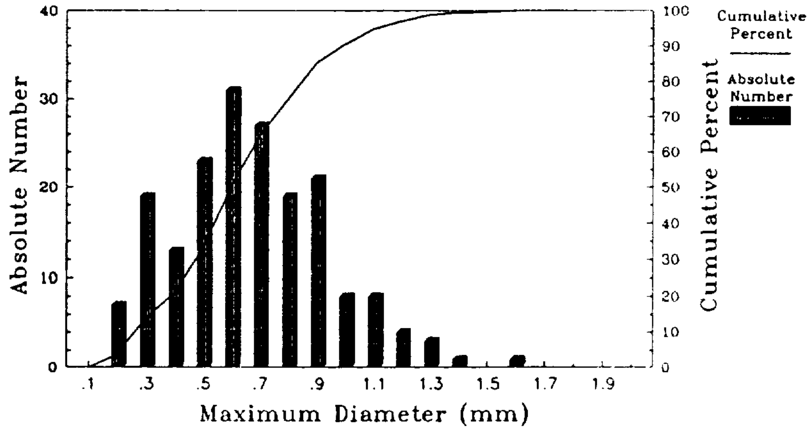

Final Screen Size - 0.75 mm

Mean Maximum Diameter - 0.62 mm

Figure 26a - Size Distribution of Cu Flakes

ORIGINAL PAGE
BLACK AND WHITE PHOTOGRAPH

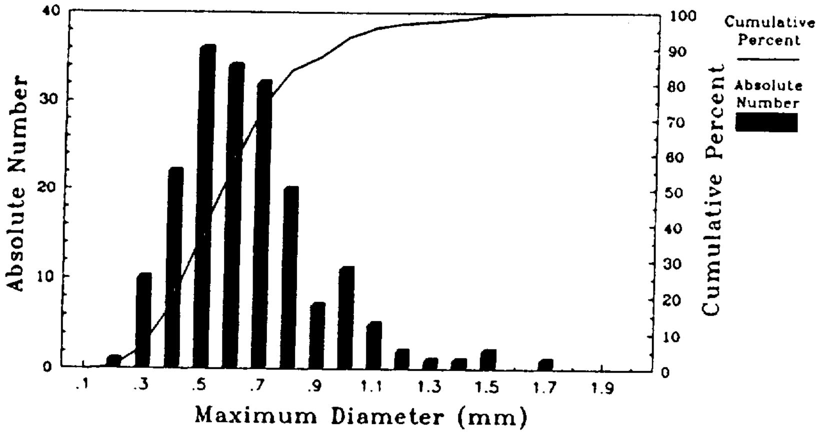

Final Screen Size - 0.75 mm

Mean Maximum Diameter - 0.61 mm

27b - Size Distribution of 2/1 Nb Flakes

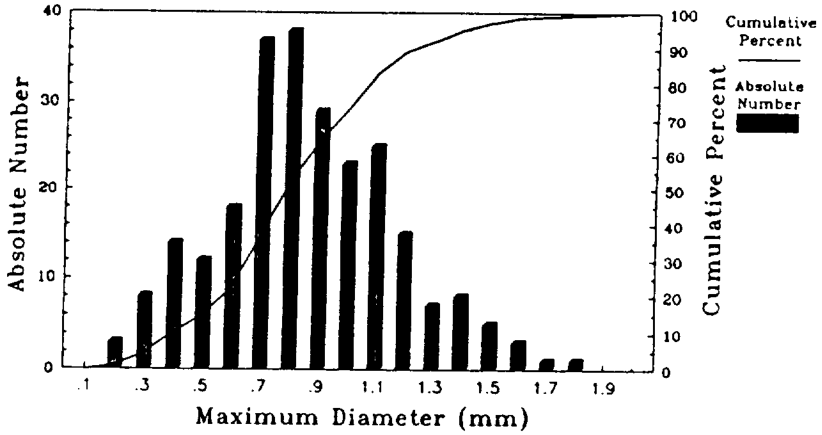

Final Screen Size - 0.75 mm

Mean Maximum Diameter - 0.81 mm

27c - Size Distribution of 4/2 Nb Flakes

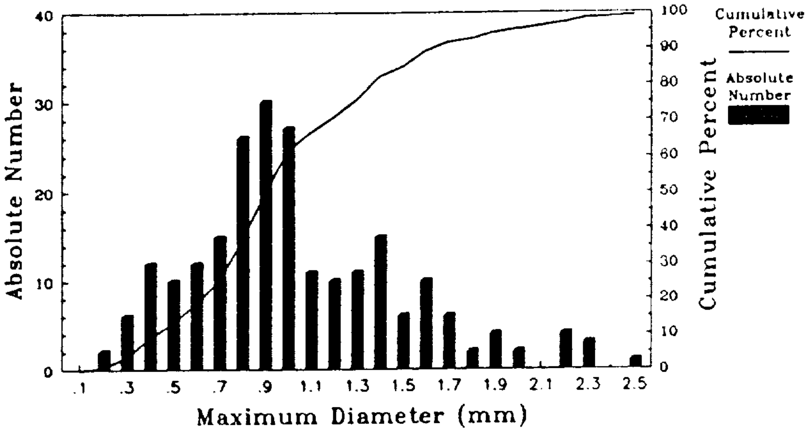

Final Screen Size - 0.75 mm

Mean Maximum Diameter - 0.99 mm

27d - Size Distribution of 6/3 Nb Flakes

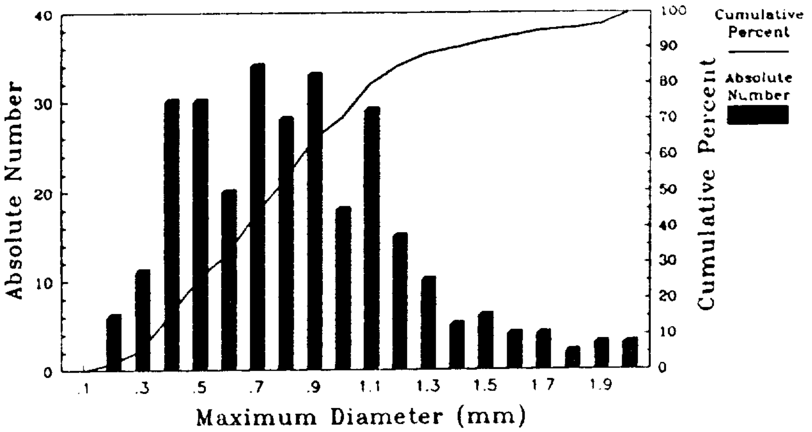

Final Screen Size - 0.75 mm

Mean Maximum Diameter - 0.80 mm

27e - Size Distribution of 8/4 Nb Flakes

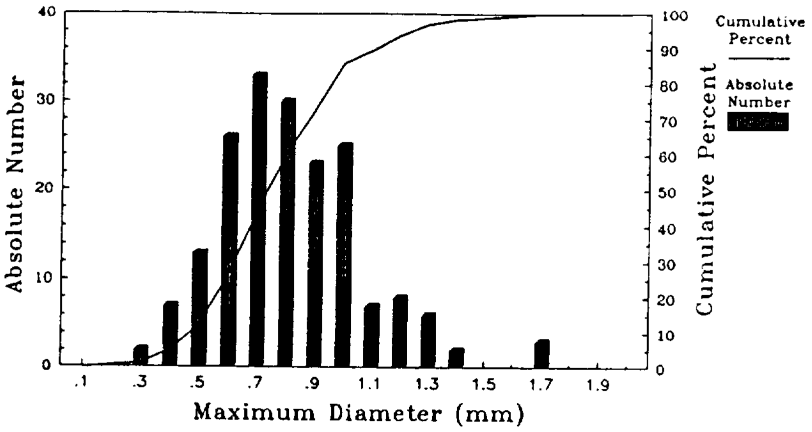

Final Screen Size - 0.75 mm

Mean Maximum Diameter - 0.77 mm

27f - Size Distribution of 10/5 Nb Flakes

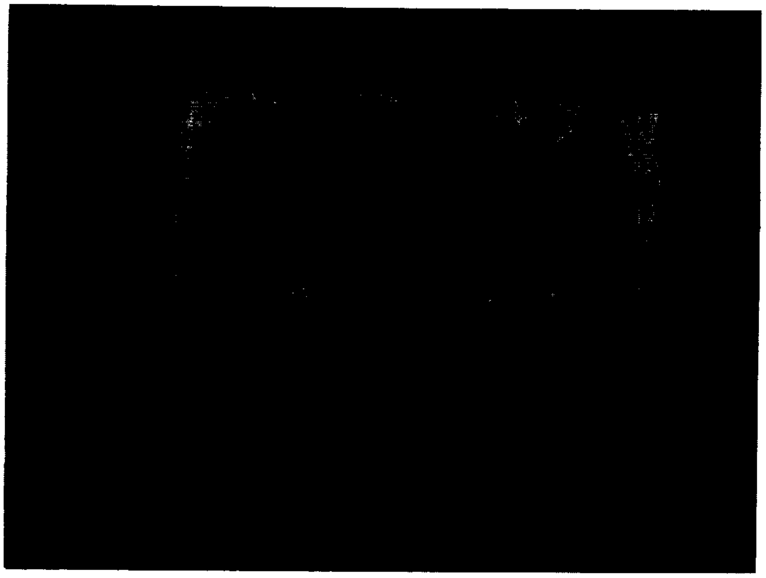

Figure 27 - Hot Pressed Plate of 2/1 Nb

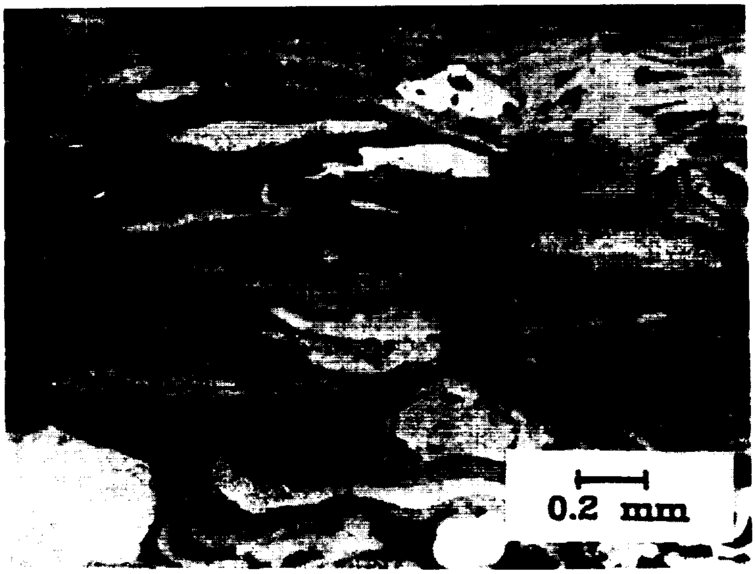

Figure 28 - Hot Pressed 8/4 Nb Hot Rolled 30%
Note Large Open Areas Denoted With Arrows

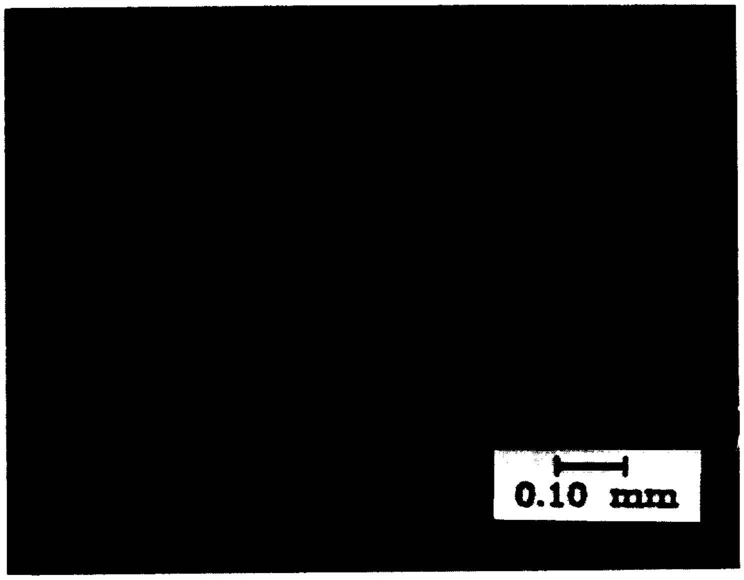

Figure 29 - Optical Micrograph Showing Flakes Outlined with Oxide Denoted With Arrows

ORIGINAL PAGE
BLACK AND WHITE PHOTOGRAPH

4.5 Microstructure

The microstructure of the induction melted master alloys, as-melt spun and aged ribbons, and consolidated materials was examined using optical microscopy and transmission electron microscopy.

4.5.1 Optical Microscopy

A typical optical micrograph of the induction melted material is shown in Figure 30. The material has large, coarse plates of Cr_2Nb in a Cu matrix. Some alloys exhibited a eutectic region due to the variation of the composition from the desired 2:1 atomic ratio of Cr to Nb. Based on the compositions, the Cu-Cr phase diagram, and work done by Bloom (166) on Cu-Cr-Ag alloys, the eutectic was determined to be a Cu-Cr eutectic.

Typical optical micrographs of the longitudinal cross sections of as-melt spun and aged ribbons appear in Figures 31 and 32. The micrographs show a variation in microstructure with alloying content, but little variation in microstructure with aging. No precipitates are observed.

The averages of the maximum diameter of the Cu grains of each alloy before and after aging were measured and calculated using a Zeiss Videoplan 2. Only limited numbers of grains in a small portion of the total ribbon length were measured. As such the numbers reflect larger than normal confidence limits. The inherent variability in the grain size due to differing cooling rates and other factors also extends the confidence limits for the measurements.

The measurements were also converted to an equivalent spherical grain size. This was accomplished by determining the diameter of a circle with an area equal to the measured area of the grain. The diameter was then used to determine the volume of a spherical grain of that diameter. This allows for comparisons between the various microstructures. The results are tabulated in Table 15.

The microstructure of the consolidated materials is shown in Figure 33. The samples show multiple oxide layers on the outer surface from the hot rolling step. The optical micrographs also clearly indicate that internal oxidation occurred.

The Cu grain size of the consolidated material was not quantitatively analyzed, but it is readily apparent from the optical micrographs that qualitatively at least the Cu grains for the Cu-Cr-Nb alloys did not undergo any significant growth while the Cu underwent considerable recrystallization and grain growth.

Table 15
Cu Grain Size and Equivalent Volumes for Cu-Cr-Nb Ribbons

	As-Melt Spun		Aged at 500°C for 100 hours	
Alloy	D_{Max} (μm)	V_{Eq} (μm^3)	D_{Max} (μm)	V_{Eq} (μm^3)
2/1 Nb	16.7	103	8.9	60.0
4/2 Nb	11.3	37.9	15.2	85.6
6/3 Nb	10.7	71.4	7.9	26.8
8/4 Nb	2.5	5.1	1.4	1.1
10/5 Nb	1.7	1.8	1.7	2.1

ORIGINAL PAGE
BLACK AND WHITE PHOTOGRAPH

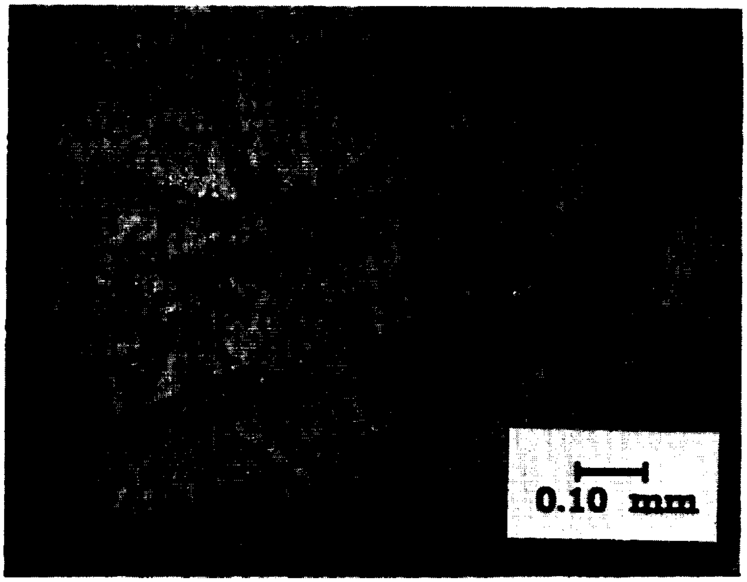

Figure 30 - Optical Micrograph of Transverse Section of Induction Melted 10/5 Nb Master Alloy Sample

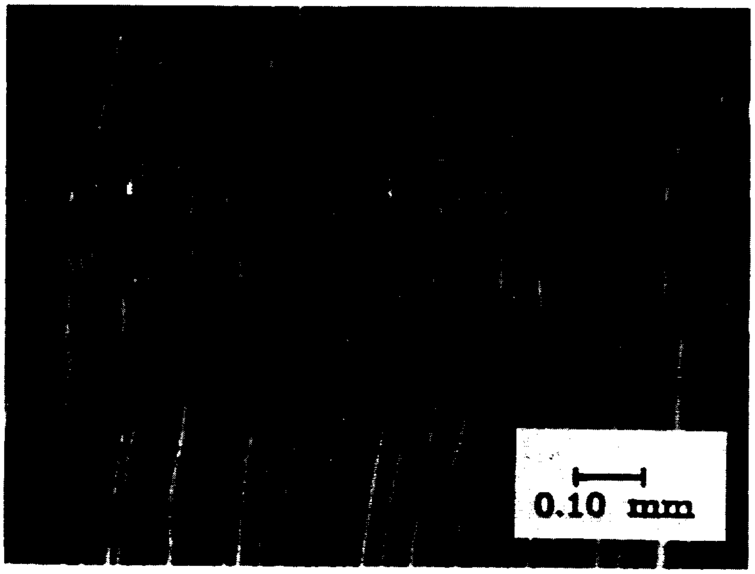

Figure 31a - DIC Optical Micrograph of As-Melt Spun 2/1 Nb Ribbon

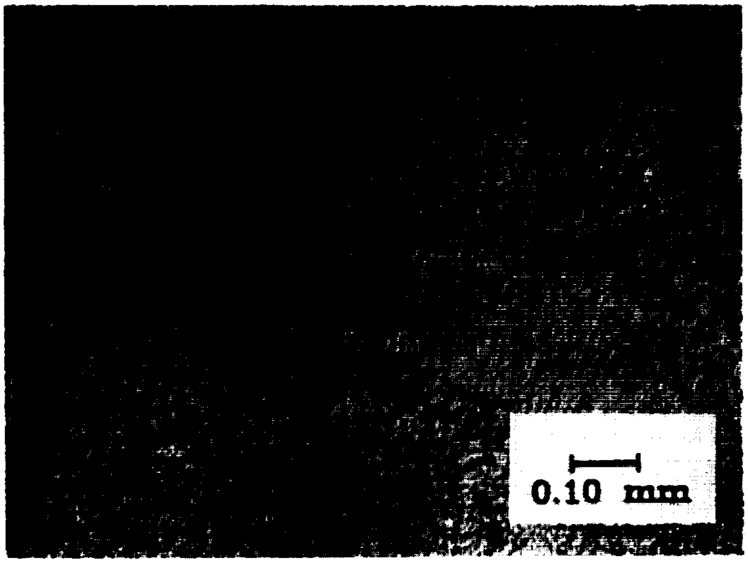

31b - DIC Optical Micrograph of As-Melt Spun 4/2 Nb Ribbon

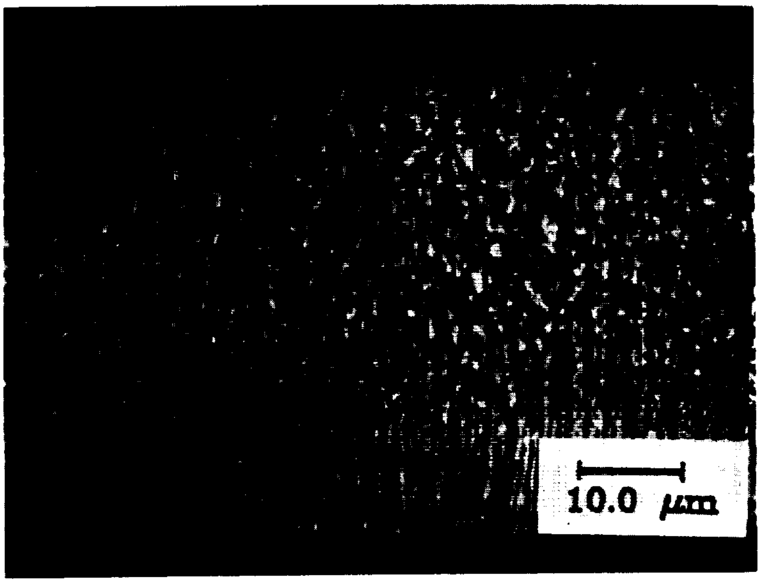

31c - DIC Optical Micrograph of As-Melt Spun 6/3 Nb Ribbon

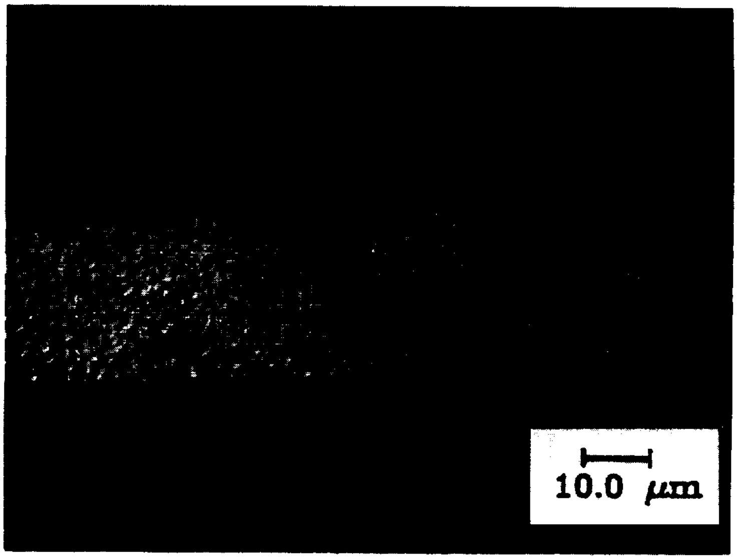

31d - DIC Optical Micrograph of As-Melt Spun 8/4 Nb Ribbon

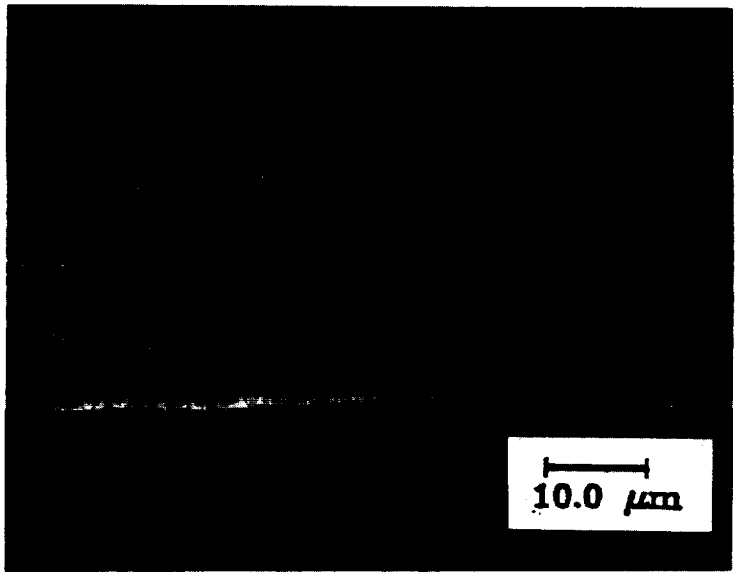

31e - DIC Optical Micrograph of As-Melt Spun 10/5 Nb Ribbon

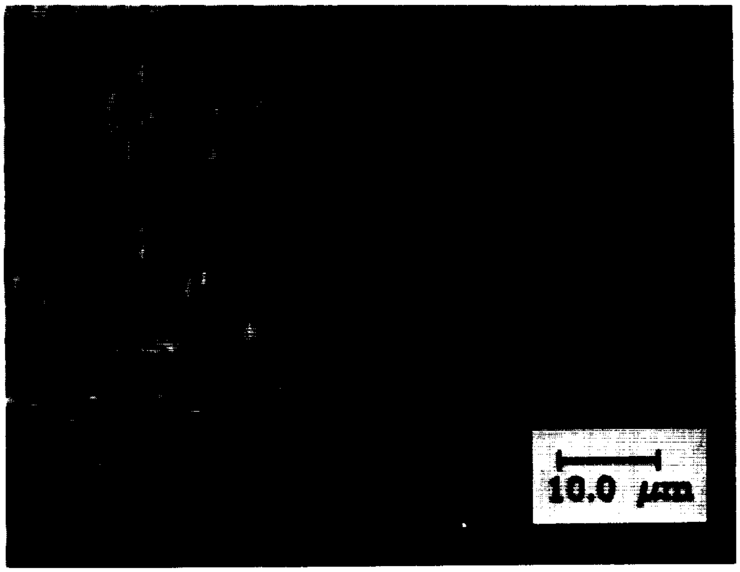

Figure 32a - DIC Optical Micrograph of 2/1 Nb Ribbon Aged 100 Hours at 500°C

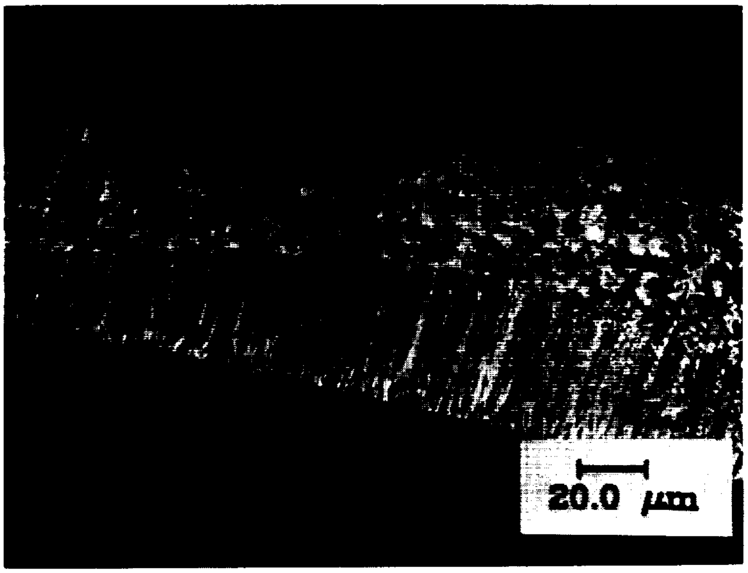

32b - DIC Optical Micrograph of 4/2 Nb Ribbon Aged 100 Hours at 500°C

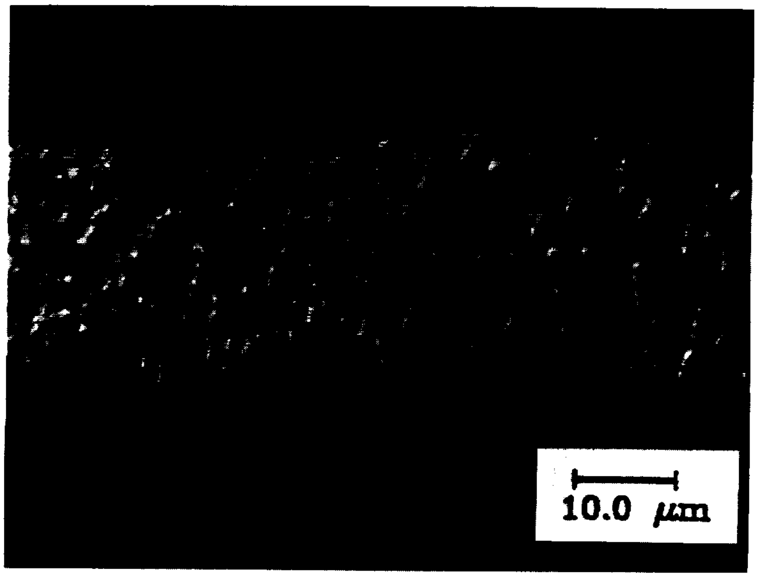

32c - DIC Optical Micrograph of 6/3 Nb Ribbon Aged 100 Hours at 500° C

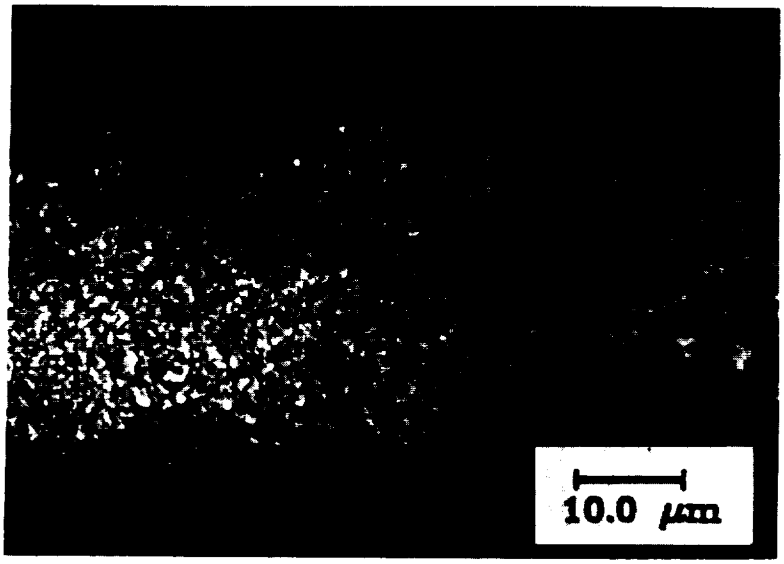

32d - DIC Optical Micrograph of 8/4 Nb Ribbon Aged 100 Hours at 500° C

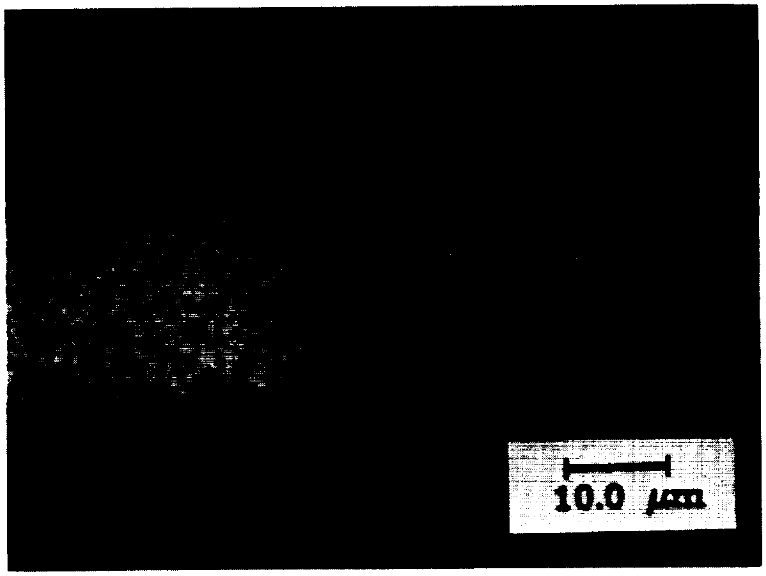

32e - DIC Optical Micrograph of 10/5 Nb Ribbon Aged 100 Hours at 500°C

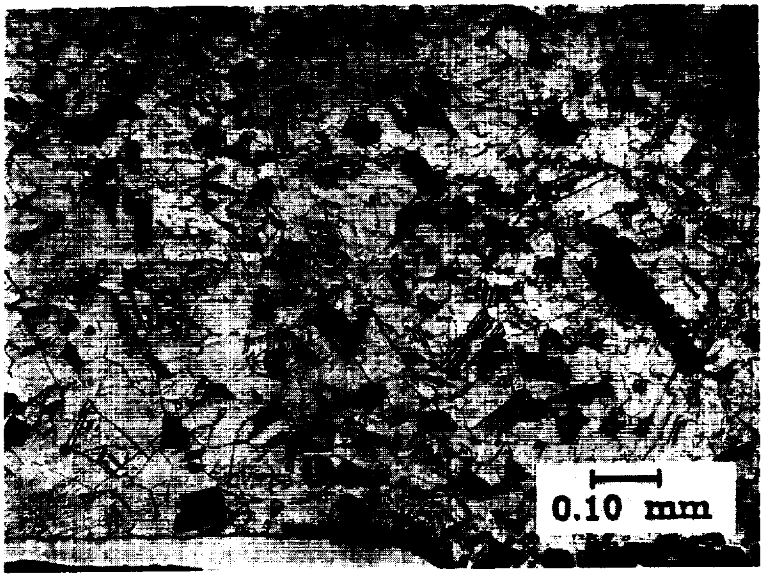

Figure 33a - Optical Micrograph of Consolidated Cu

ORIGINAL PAGE
BLACK AND WHITE PHOTOGRAPH

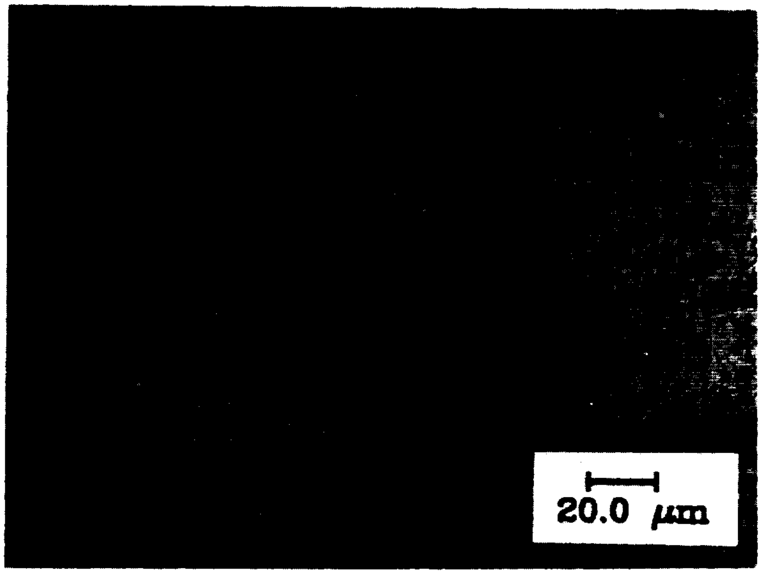

33b - Optical Micrograph of Consolidated 2/1 Nb

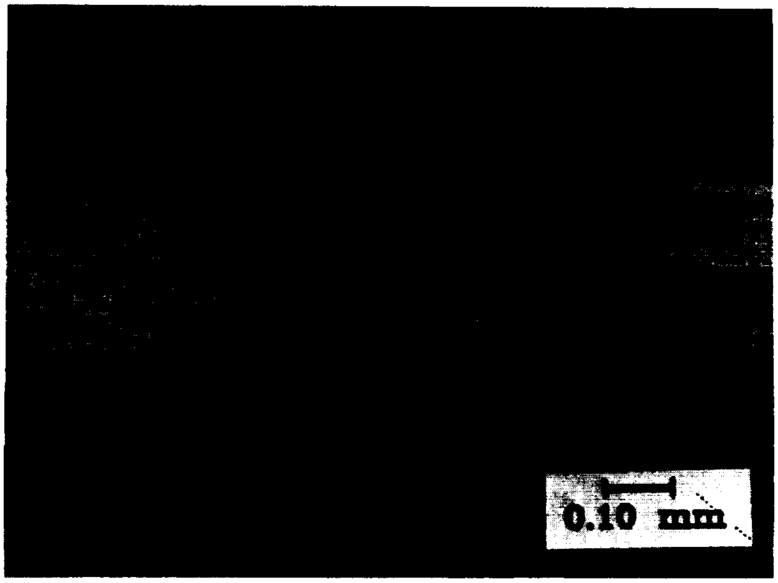

33c - Optical Micrograph of Consolidated 4/2 Nb

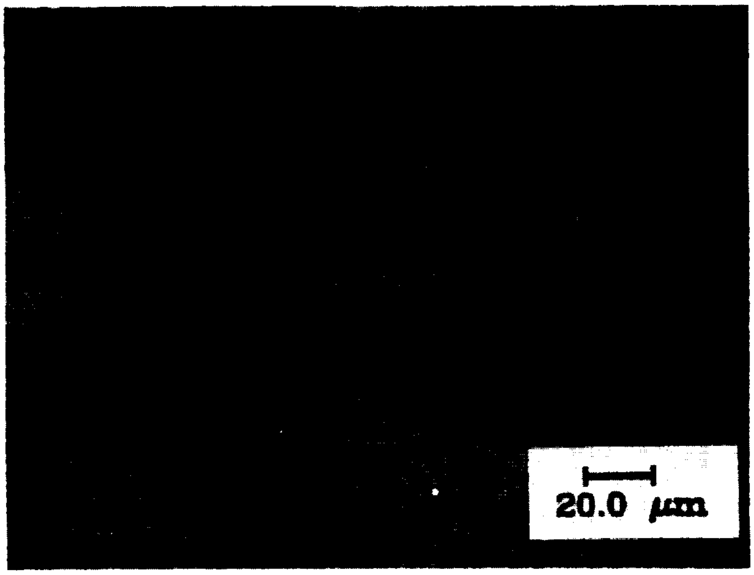

33d - Optical Micrograph of Consolidated 6/3 Nb

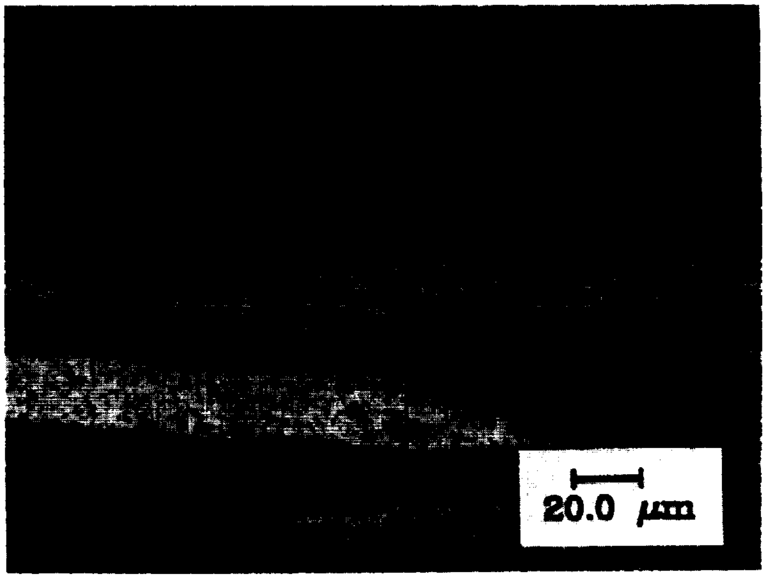

33e - Optical Micrograph of Consolidated 8/4 Nb

ORIGINAL PAGE
BLACK AND WHITE PHOTOGRAPH

ORIGINAL PAGE
BLACK AND WHITE PHOTOGRAPH

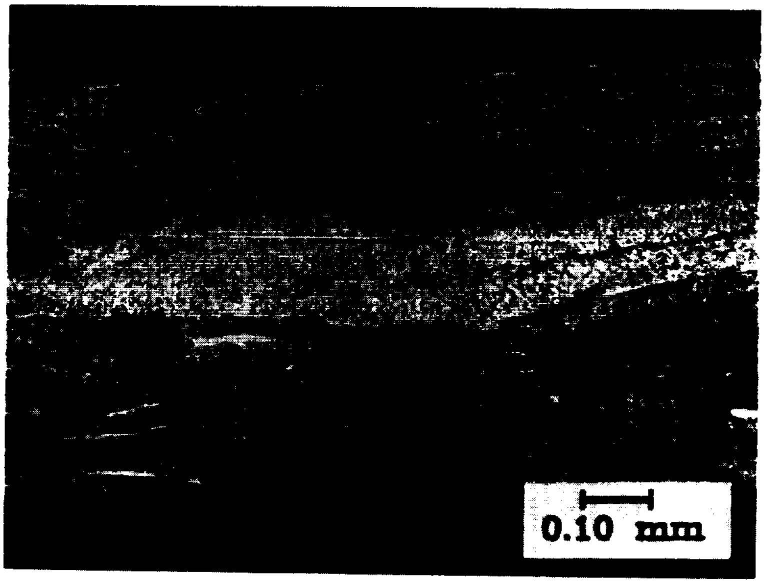

33f - Optical Micrograph of Consolidated 10/5 Nb

4.5.2 Transmission Electron Microscopy (TEM)

Transmission electron microscopy (TEM) was necessary to observe the precipitates in the consolidated material as well as the as-melt spun and aged ribbons. A combination of bright field images, dark field images, selected area diffraction patterns, and EDS spectra were used to characterize the microstructure and precipitates in the materials.

A characteristic bright field micrograph of the 2/1 Nb alloy appears in Figure 34. Two types of precipitates were observed. The first set of precipitates appear very light against the background and are designated type A. The second set of precipitates appear dark against the background and are designated type B. The electron beam was focussed on a type A precipitate and an EDS spectra obtained. The results appear in Figure 35. Strong Cr K_α peaks are observed with weak Cu K_α peaks from the surrounding matrix also detected. No Nb peak is observed in the spectra despite the fact that Nb was easily detected when a bulk spectra of the sample was taken. The beam was refocussed on a type B precipitate and another EDS spectra obtained. The results appear in Figure 36. In addition to a strong Cr peak, strong Nb K_α and L_α peaks are observed.

Quantitative analysis of the peak height taking into account the K ratios for Cr and Nb (167) was performed. The Cr K_α peak height was compared to the Nb K_α and L_α peak heights to determine the atomic ratio for Cr to Nb. Allowing for the K ratios of Cr and Nb, the results consistently indicated that the ratio was ≈2, the same ratio as stoichiometric Cr_2Nb.

From the EDS spectra the type A precipitates were identified as elemental Cr while the type B precipitates were identified as Cr_2Nb. To confirm the analysis and determine the form of the precipitates present, SAD patterns were obtained for all the samples.

A typical SAD pattern appears in Figure 37. The SAD pattern contains many rings, indicative of a noncubic phase. The pattern was successfully indexed using the d spacings for the high temperature hexagonal phase of Cr_2Nb with lattice parameters of a_0 equal to 0.487 nm and c_0 equal to 0.794 nm. Rings with the d spacings for FCC Cr were looked for, but none were observed. The d spacings for the BCC phase of Cr overlap the d spacings of Cr_2Nb, and thus the rings for elemental BCC Cr could not be independently observed. The intense regions of some of the rings were identified as Cu_2O that formed on the surface of the samples during preparation. The combination of the EDS spectra and SAD patterns showed that for the 2/1 Nb ribbons both BCC Cr and the high temperature hexagonal phase of Cr_2Nb were present.

For the 4/2 Nb, 6/3 Nb, 8/4 Nb, and 10/5 Nb alloys only Cr_2Nb precipitates were observed. The near 2 to 1 ratio of Cr to Nb for the 4/2 Nb, 6/3 Nb, and 8/4

Nb means that, assuming nearly complete reaction to form Cr_2Nb, the volume fraction of Cr and Nb precipitates is small. Thus the likelihood of observing elemental precipitates is small. Any elemental Cr or Nb precipitates that appear in the 10/5 Nb alloys were masked by the large number of Cr_2Nb precipitates.

Dark field images were used to further differentiate the two types of precipitates and determine the size of each. Two imaging conditions were used. The first utilized a ring that corresponds to both the d spacing for the $\{1\,1\,0\}$ planes of BCC Cr and the d spacing for the $\{2\,0\,\bar{2}\,1\}$ planes of hexagonal Cr_2Nb. The second condition utilized a ring with a d spacing that corresponds to only the d spacing for the $\{2\,0\,\bar{2}\,2\}$ plane of hexagonal Cr_2Nb. The resulting images and a corresponding bright field image appear in Figure 38.

Since there was no well established orientation relationship between the precipitates and the matrix as shown by the uniform ring patterns, it was difficult to find corresponding precipitates for both imaging conditions. However, careful examination of many areas using both imaging conditions showed that the type A precipitates were never in bright contrast when the imaging condition corresponding to only Cr_2Nb was used. Both types of precipitates were in bright contrast when the condition corresponding to both Cr and Cr_2Nb was used. These dark field images from many areas were used to distinguish large numbers of Cr and Cr_2Nb precipitates.

Once the two types of precipitates were identified, the size of the precipitates was measured. For Cr_2Nb the results indicate a bimodal size distribution. Figure 39 shows the size distribution of Cr and Cr_2Nb precipitates for the 2/1 Nb alloy. The size distribution is typical for all the alloys. The results also indicate a wide, continuous size distribution for the Cr precipitates with the average size being 18 nm. The size range observed though was between 9 nm and 50 nm. Table 16 lists the average sizes for Cr_2Nb precipitates observed in the alloys.

Figure 40 shows a bright field micrograph for the 10/5 Nb alloy. Only Cr_2Nb precipitates were observed in this alloy. The most important features of the micrograph is the size of the precipitates and the spatial distribution of the precipitates. The average size of the precipitates is approximately the same as that for the 2/1 Nb alloy, a result not expected since the alloy has significantly more Cr and Nb. The precipitates also show considerable agglomeration. Large clumps containing hundreds of precipitates were observed next to areas totally free of precipitates. From this and other data the argument to be presented in Section 5.3 that the Cr_2Nb precipitates formed in the liquid Cu was developed.

Consolidated materials produced good samples with ample thin areas. Figure 41 shows typical bright field micrographs of the consolidated materials. Considerable internal structure was observed in the Cr_2Nb precipitates. The precipitates were observed to have coarsened considerably compared to the as-melt spun ribbons, but were still submicron size. The precipitate size distributions and average sizes are presented in Figure 42 and Table 15 respectively. Only infrequently were Cr precipitates were observed in these alloys.

The SAD patterns of the aged ribbons and consolidated materials were examined to see if a phase change in the Cr_2Nb from hexagonal to FCC had occurred during aging or consolidation. Figure 43 shows a SAD pattern from 4/2 Nb aged 100 hours. A SAD pattern for the consolidated 10/5 Nb alloy is shown in Figure 44. The results indicate that no phase change had occurred in the alloys

Table 16
Average Size Of Cr_2Nb Precipitates

	Melt Spun Ribbon				
	As-melt Spun				
Alloy	Overall (nm)	Small Precips. (nm)	Large Precips. (nm)	Aged 500°C 100 hrs	Consolidated
2/1 Nb	20.8	16.4	51.6	-	96.7
4/2 Nb	26.4	22.6	45.2	20.6	77.4
6/3 Nb	25.8	21.2	45.5	-	164.3
8/4 Nb	26.9	22.0	47.1	-	135.1
10/5 Nb	26.5	22.0	49.2	-	69.2

Figure 34 - Typical Bright Field TEM Micrograph of As-Melt Spun 2/1 Nb Ribbon

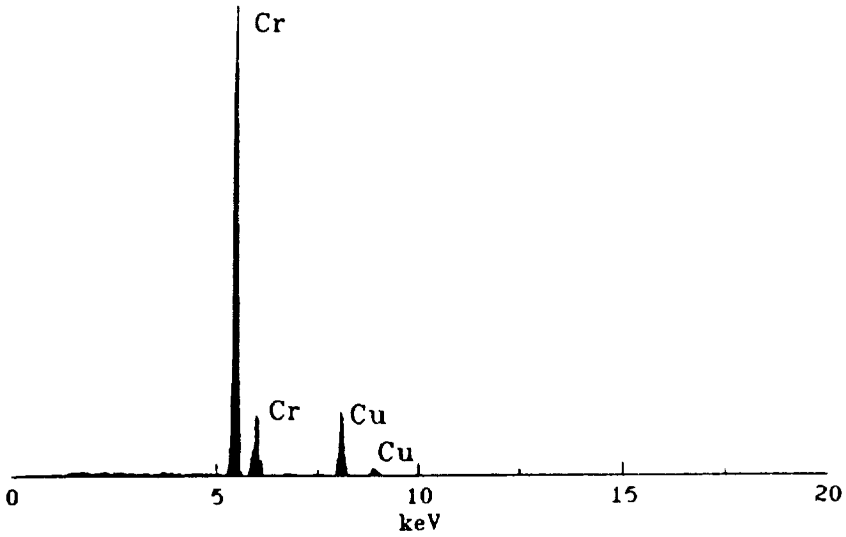

Figure 35 - EDS Spectra of Type A (Cr) Precipitates

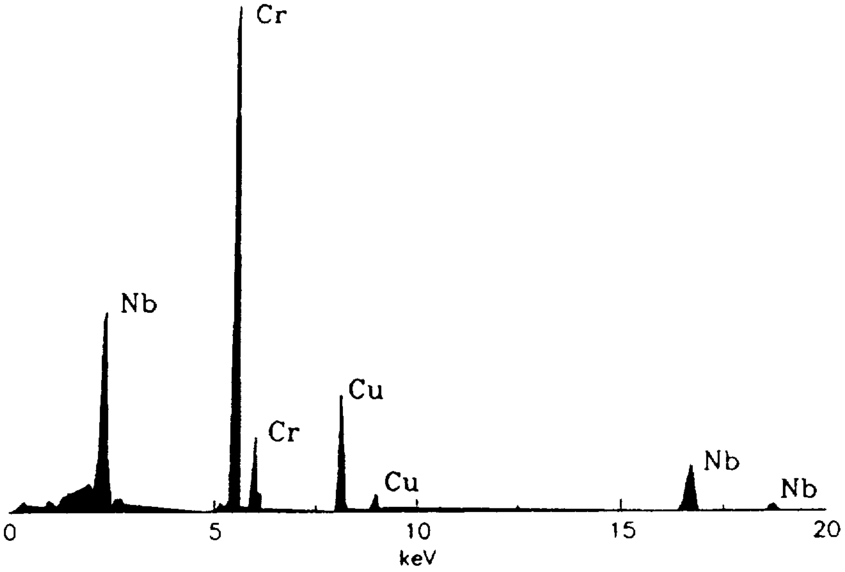

Figure 36 - EDS Spectra of Type B (Cr_2Nb) Precipitates

ORIGINAL PAGE
BLACK AND WHITE PHOTOGRAPH

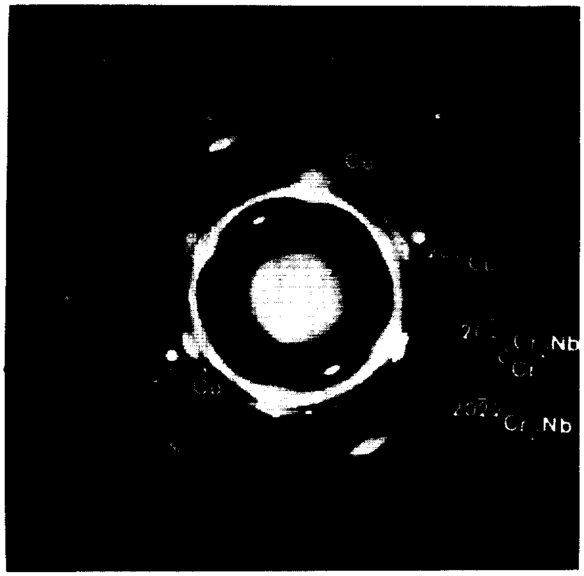

Figure 37 - SAD Pattern of As-Melt Spun 2/1 Nb Showing Ring Patterns for Cr and Cr_2Nb Precipitates; <111> Cu Zone

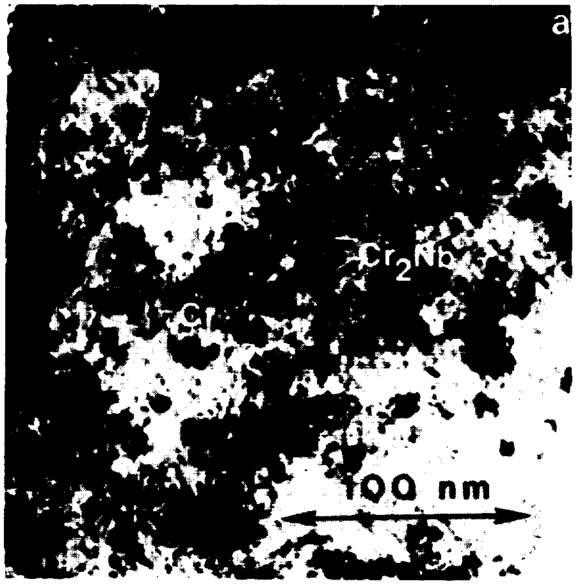

Figure 38a - Bright Field View of Area Imaged in Figures 38b and 38c

38b - Dark Field View of Figure 38a Using the First Imaging Condition. Both Cr and Cr_2Nb Precipitates Are In Strong Contrast.

38c - Dark Field View of Figure 38a Using the Second Imaging Condition. Only Cr_2Nb Precipitates Are In Strong Contrast.

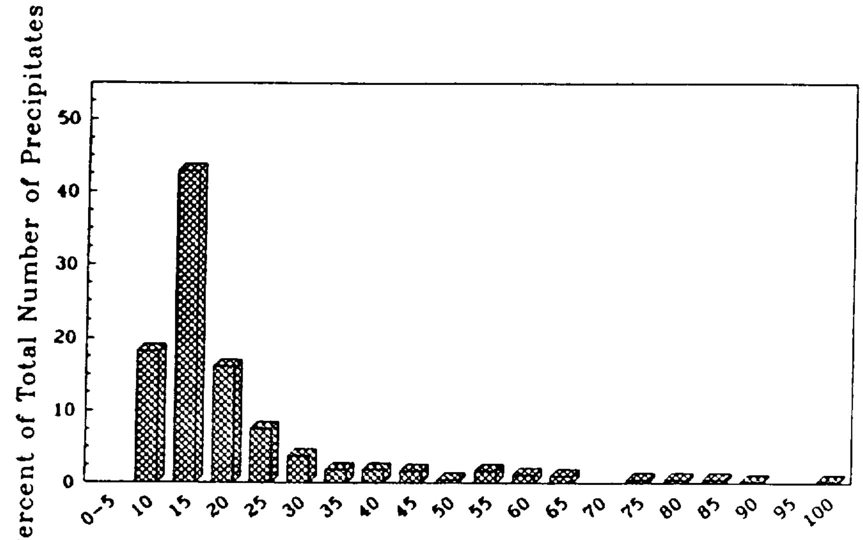

Figure 39a - Cr_2Nb Precipitate Size Distribution in As-Melt Spun 2/1 Nb

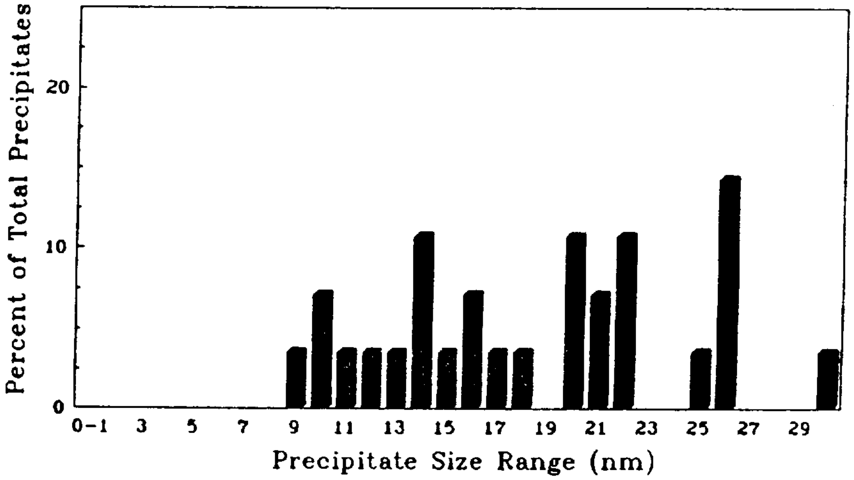

39b - Cr Precipitate Size Distribution in As-Melt Spun 2/1 Nb

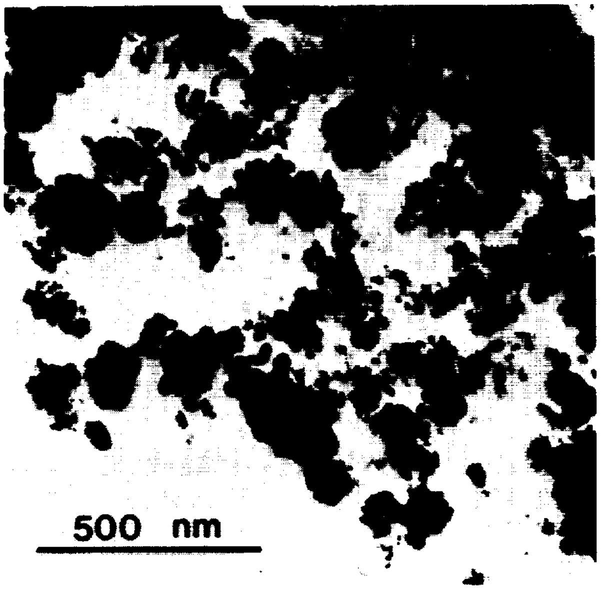

Figure 40 - Bright Field Micrograph of 10/5 Nb Alloy

Figure 41a - Bright Field Micrograph of Consolidated 2/1 Nb

41b - Bright Field Micrograph of Consolidated 4/2 Nb

41c - Bright Field Micrograph of Consolidated 6/3 Nb

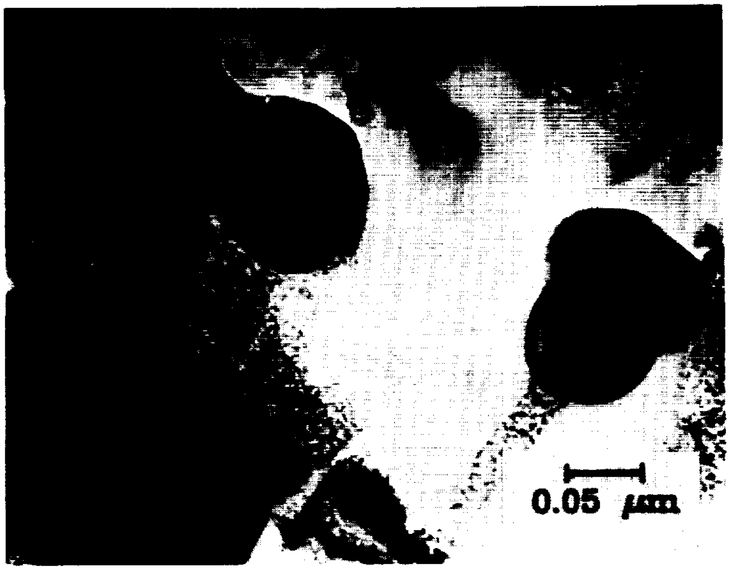

41d - Bright Field Micrograph of Consolidated 8/4 Nb

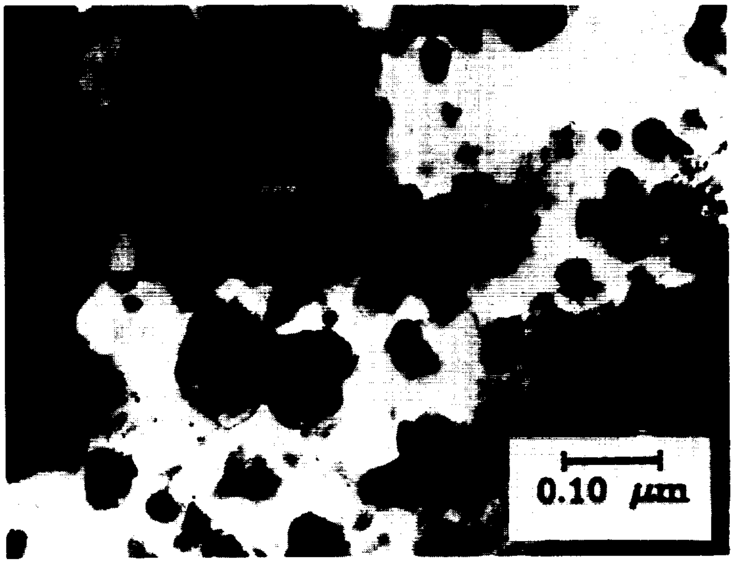

41e - Bright Field Micrograph of Consolidated 10/5 Nb

ORIGINAL PAGE
BLACK AND WHITE PHOTOGRAPH

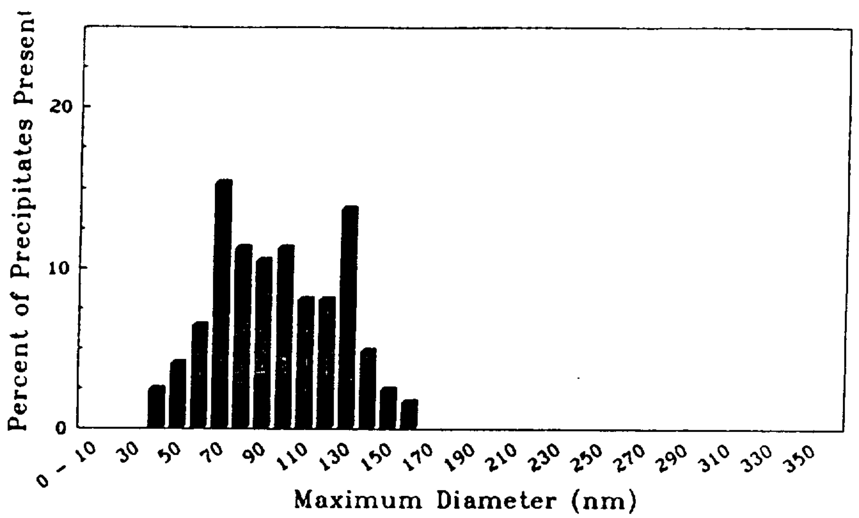

Figure 42a - Precipitate Size Distribution for Consolidated 2/1 Nb

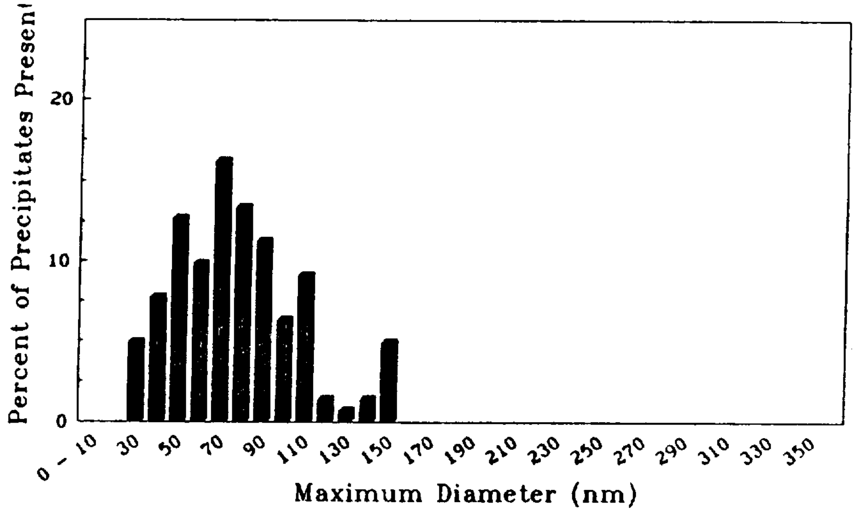

42b - Precipitate Size Distribution for Consolidated 4/2 Nb

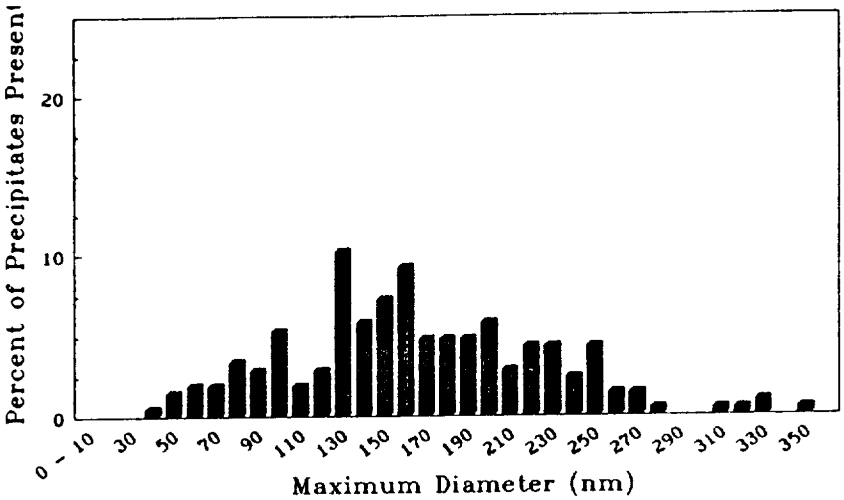

42c - Precipitate Size Distribution for Consolidated 6/3 Nb

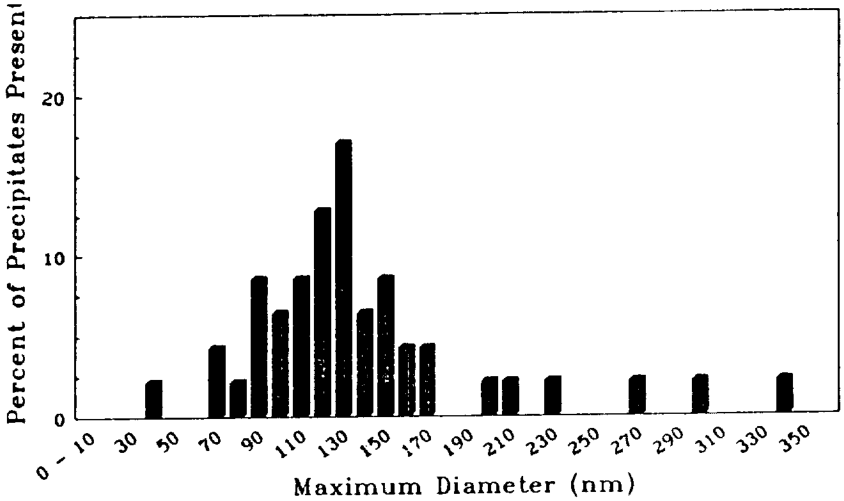

42d - Precipitate Size Distribution for Consolidated 8/4 Nb

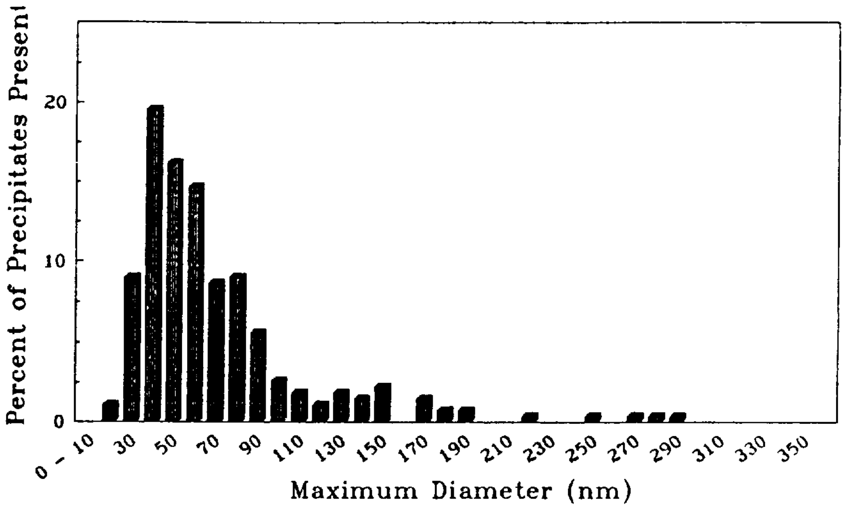

42e - Precipitate Size Distribution for Consolidated 10/5 Nb

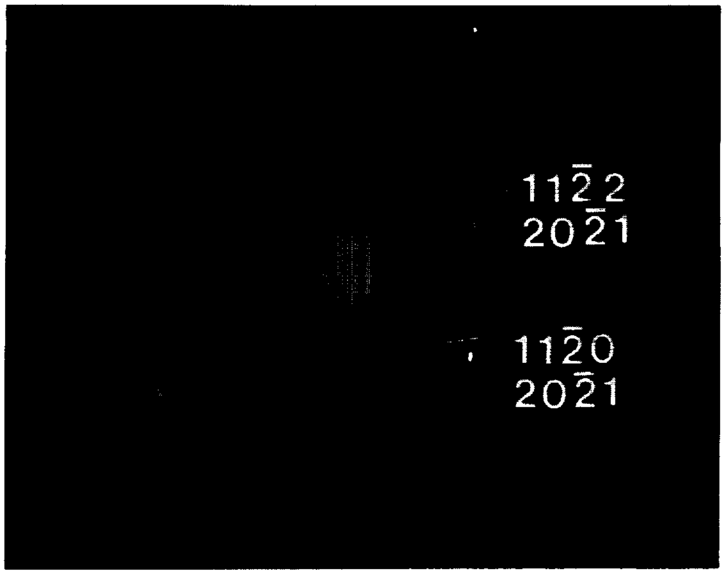

Figure 43 - SAD Pattern of 4/2 Nb Aged 100 Hours at 500°C

ORIGINAL PAGE
BLACK AND WHITE PHOTOGRAPH

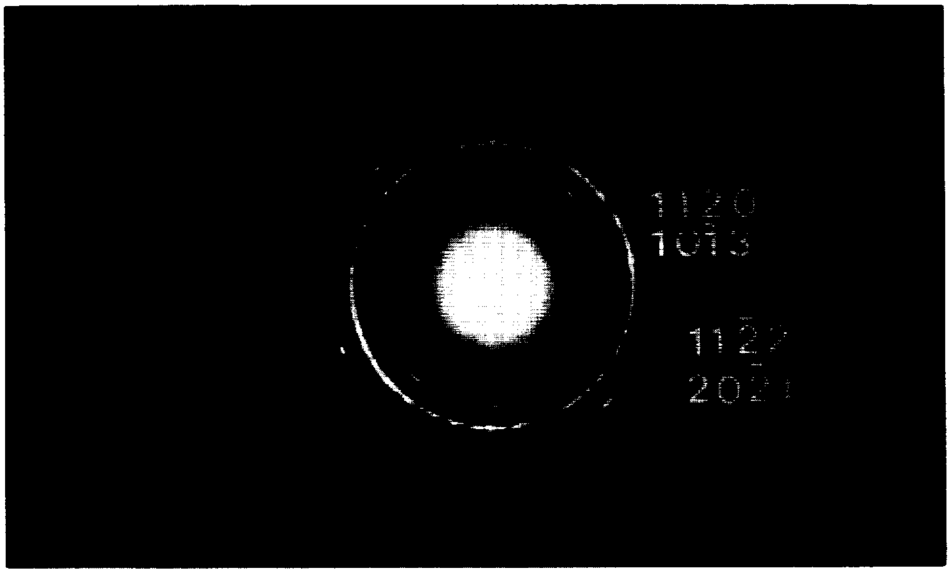

Figure 44 - SAD Pattern of Consolidated 10/5 Nb

4.6 Mechanical Properties

The mechanical properties of the materials were measured using both microhardness and tensile testing. The microhardness data covers all the alloys in all conditions examined in the study. Tensile testing of ribbon proved difficult, so only room temperature tensile strength data of as-melt spun ribbons is presented.

4.6.1 Microhardness

The results of the microhardness measurements are shown in Figure 45 for the as-melt spun ribbon, aged ribbon, and consolidated material. No values for induction melted material are presented because of the large variability of the microhardness depending on how much of the indent contained Cr_2Nb. The induction melted materials were used to determine the microhardness of the

Cr_2Nb phase by taking measurements from particles several millimeters in size using a 10 gram load to minimize matrix contribution to the readings. The measured value of the microhardness of the Cr_2Nb was 1920 KHN.

The microhardness results showed a significant variation in the values. The standard deviation for the measurements was typically 20 KHN. This represents a value between 10% and 15% of the reported values. In some isolated cases, certain measurements had to be deleted because they were so incongruous with respect to the other measurements for the alloy and aging condition.

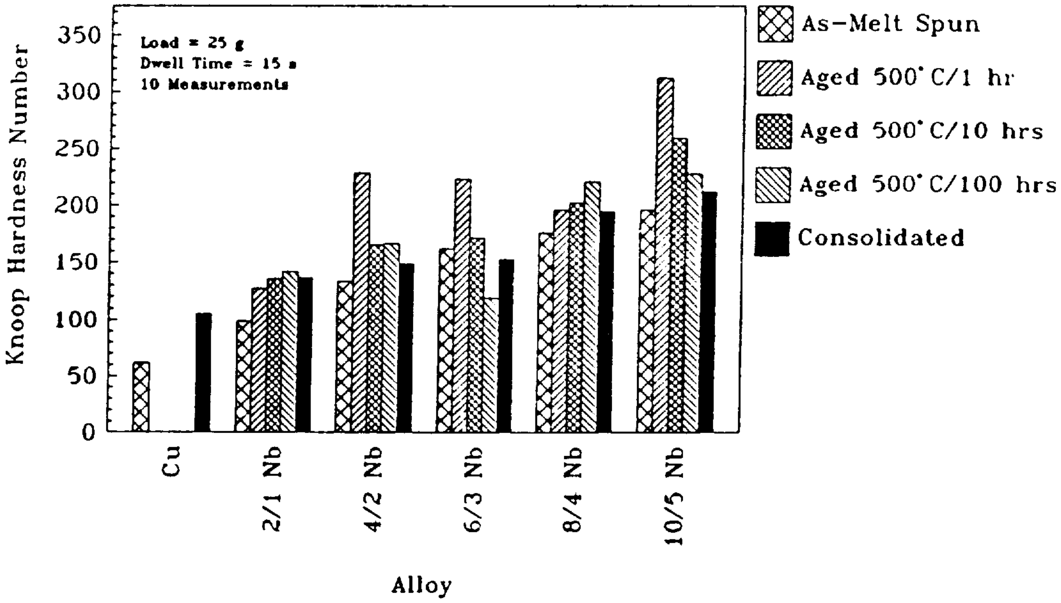

Figure 45 - Room Temperature Microhardnesses of As-Melt Spun, Aged, and Consolidated Cu-Cr-Nb Alloys. As-Melt Spun and Consolidated Cu Presented for Comparison

4.6.2 Tensile Testing

The yield and ultimate tensile strengths of the as-melt spun ribbons at room temperature are presented in Figure 46. No values for elongation are reported because the ductility of the material was severely limited by the sample geometry which tended to induce a plane strain condition and tearing of the ribbons during testing.

The yield strength and ultimate tensile strength of the consolidated materials for temperatures between 20°C and 850°C appear in Figure 47. The plot also presents the values for elongation obtained from these samples. The values should be considered lower limit bounds for the ultimate tensile strengths and ductilities of the material due to the pre-existing cracks in the material.

Scanning Electron Microscopy (SEM) work was done on the fracture surfaces of the test samples. Features indicating ductility such as dimples were the main target of this search. SEM fractographs of a typical ribbon sample appears in Figure 48 and of a typical consolidated specimen in Figure 49.

Optical microscopy was also performed on the longitudinal cross-sections of the ribbon samples and consolidated material tensile test samples near the fracture surfaces. The results appear in Figures 50 and 51 respectively.

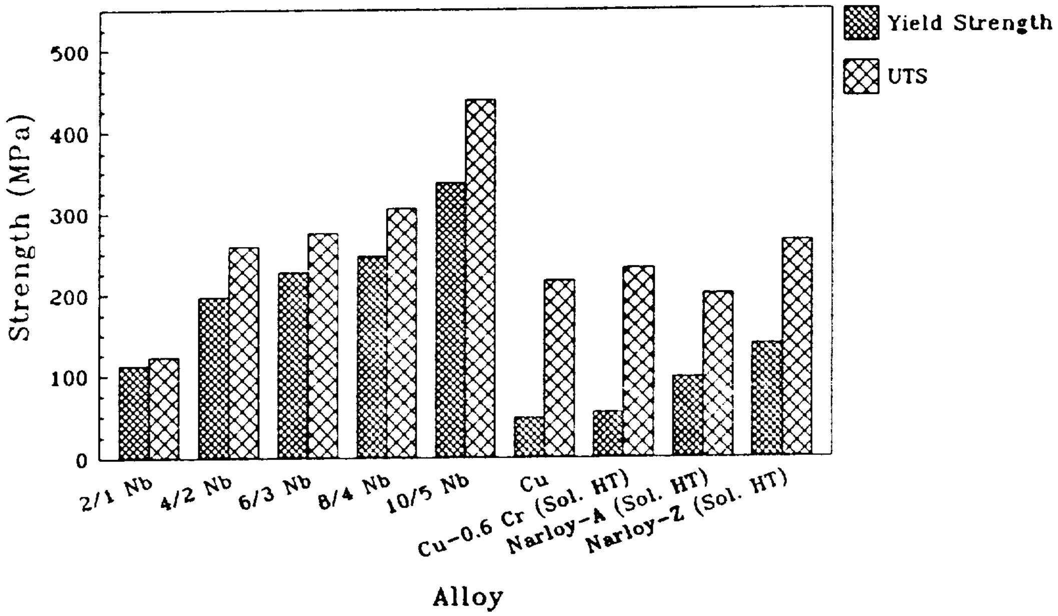

Figure 46 - Comparison of Room Temperature Strength of As-Melt Spun Cu-Cr-Nb Ribbons to Cu and Other High Temperature Cu-Based Alloys

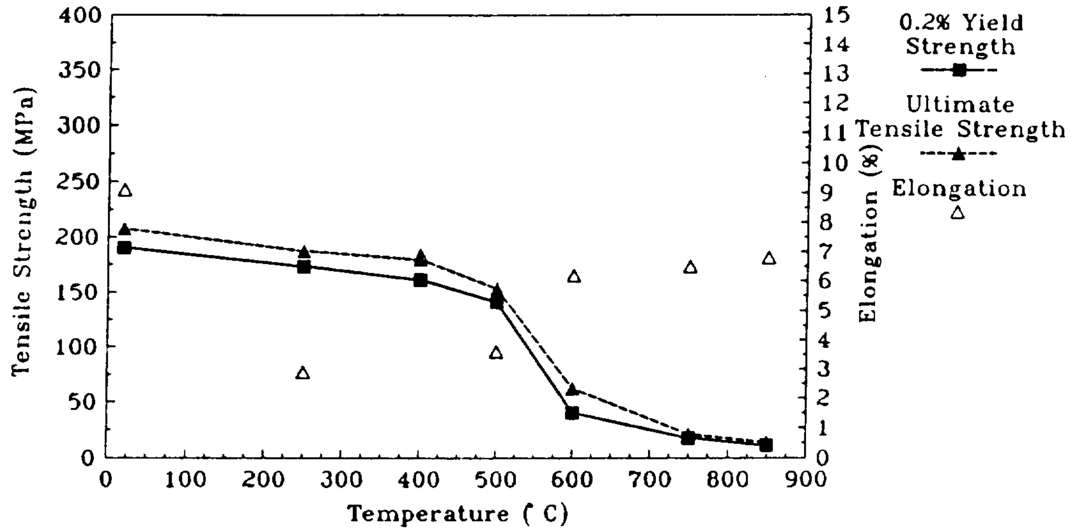

Figure 47a - Tensile Strength and Elongation of Consolidated Cu at Temperatures Between 20°C and 850°C

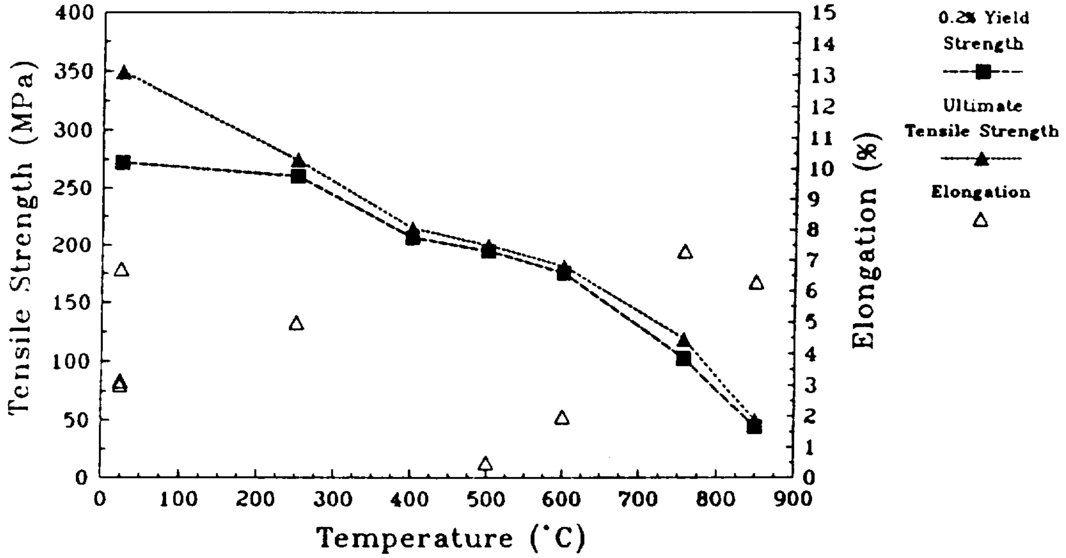

47b - Tensile Strength and Elongation of Consolidated 2/1 Nb at Temperatures Between 20°C and 850°C

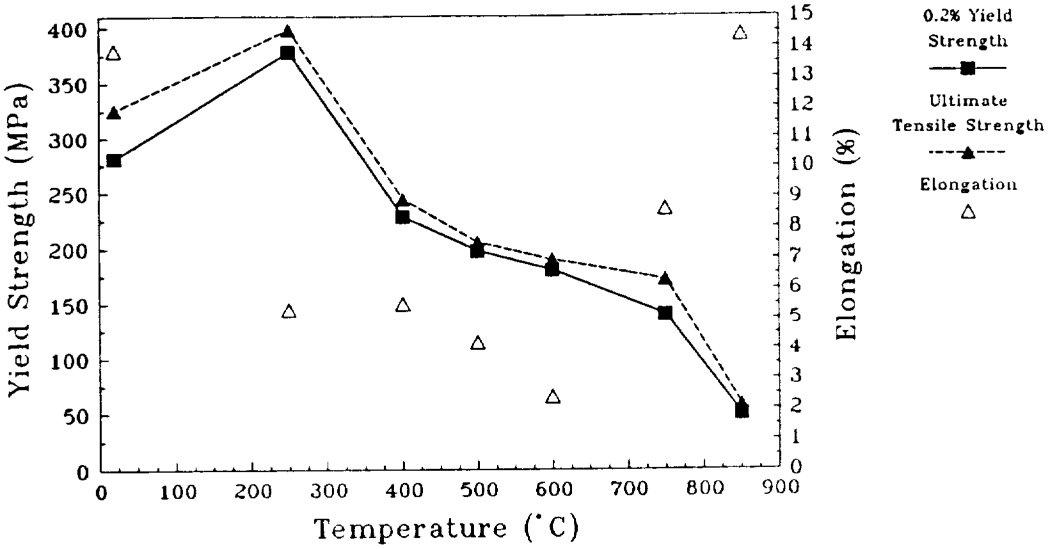

47c - Tensile Strength and Elongation of Consolidated 8/4 Nb at Temperatures Between 20° C and 850° C

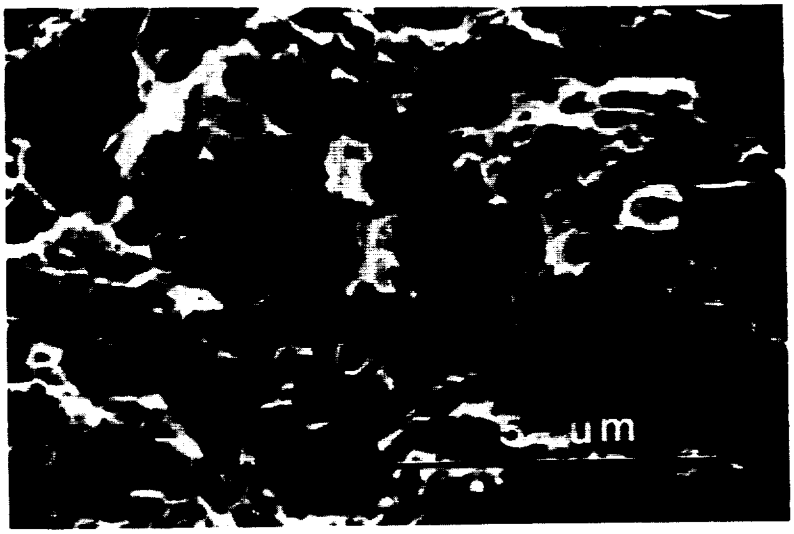

Figure 48 - SEM Fractograph of Ribbon Tensile Test Specimen

ORIGINAL PAGE
BLACK AND WHITE PHOTOGRAPH

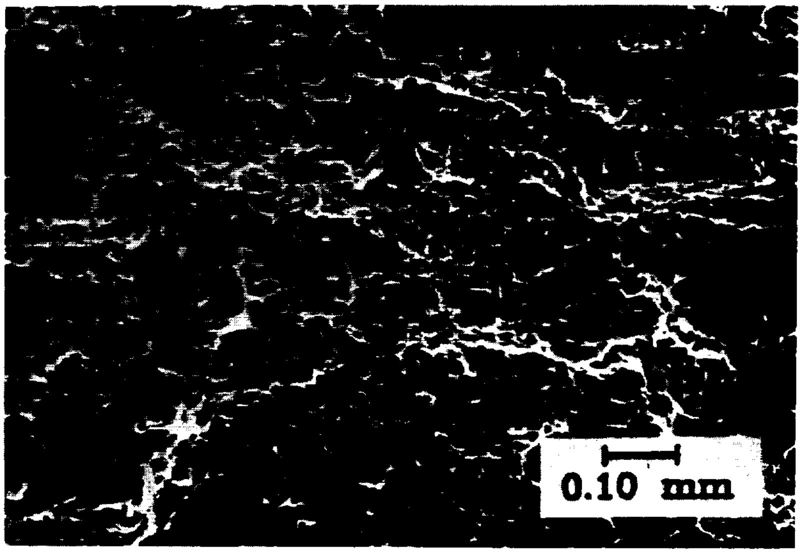

Figure 49 - SEM Fractograph of Consolidated Tensile Test Specimen

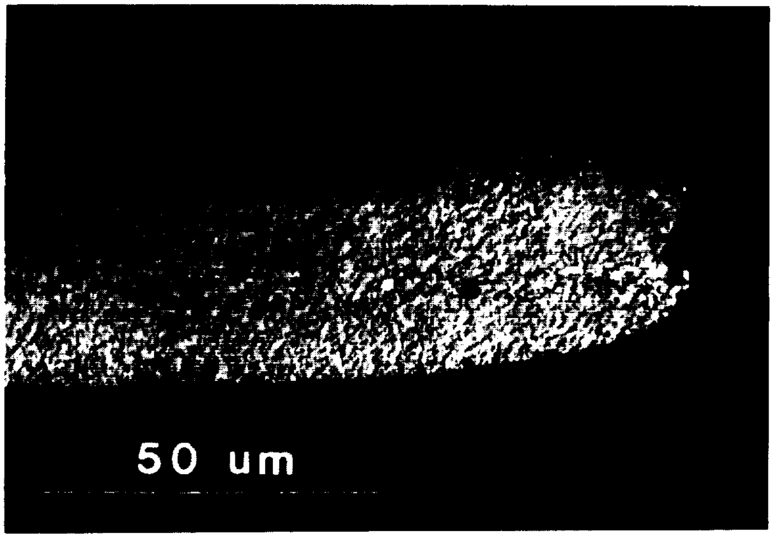

Figure 50 - Optical Micrograph of Longitudinal Cross-Section of Ribbon Tensile Test Specimen in Region of Fracture

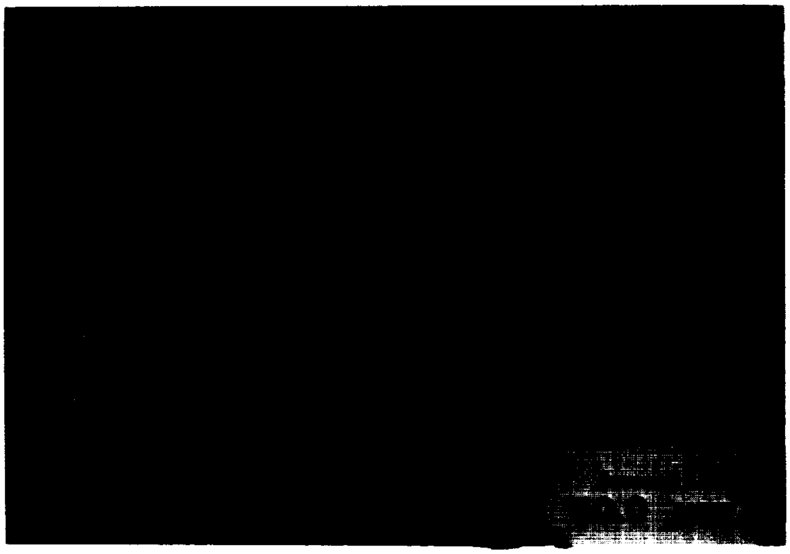

Figure 51 - Optical Micrograph of Longitudinal Cross-Section of Consolidated Tensile Test Specimen in Region of Fracture

4.7 Electrical Resistivities and Calculated Thermal Conductivities

The measured values for electrical resistivity and the calculated values for thermal conductivities at room temperature for as-melt spun and aged ribbons are shown in Figures 52 and 53. A sample of melt spun Cu ribbon was also tested, and the data is also presented.

The samples for the room temperature electrical resistivity and thermal conductivity measurements showed significant tarnishing following exposure for 100 hours. The presence of this tarnish layer reduced the cross-sectional area of the samples, but since no quantitative data was available to take into account this effect, the measured values for the cross-sectional area were used. The result is an increase in electrical resistivity and a decrease in the thermal conductivity.

ORIGINAL PAGE
BLACK AND WHITE PHOTOGRAPH

The resistivity measurements for elevated temperatures are not constant due to the changes in conductivity with temperature and the microstructural changes occurring in the alloys with time at elevated temperatures. As such, the data is best presented as a plot of electrical resistivity or thermal conductivity with respect to time. Plots of electrical resistivity and temperature versus time are presented in Figure 54. Figure 55 summarizes the results to allow easy comparison between the various runs. Using the Weidmann-Franz Law and the Lorentz number for pure Cu, the electrical resistivity values were converted into thermal conductivities. The results appear in Figure 56.

Following aging for at least 24 hours for the Cu-Cr-Nb alloys and 4 hours for the Cu ribbon at 500°C, the samples were heated to a maximum temperature between 550°C (1022°F) and 600°C (1112°F) and cooled to room temperature to measure the dependence of electrical resistivity and thermal conductivity on temperature. The results are presented in Figure 57 and summarized in Figure 58 for comparison. The values were again converted to thermal conductivities using the Wiedmann-Franz Law. The results appear in Figure 59. Figure 60 combines all the plots for comparison.

From the resistivity versus temperature data, the dependence of electrical resistivity on temperature over the entire test range and between two temperature ranges of interest, 25°C to 100°C and 450°C to 550°C, was determined. This was expressed as a temperature coefficient for electrical resistivity. The results are listed in Table 17.

The results of the isothermal aging experiments indicate that the materials precipitate the solute trapped in the supersaturated matrix during the heating of the samples and immediately thereafter. Vacancies which are also present in the material in high concentrations (168) are annihilated by moving to grain boundaries or the surface. This is evidenced by the decreases in resistivity between 0 and 1000 seconds.

Reversion does not appear to occur in the Cu-Cr-Nb alloys. The samples of melt spun ribbon show an initial increase in resistivity that can be accounted for by the increase in temperature increasing the resistivity of the Cu matrix.

The results also show that while the thermal conductivity of the alloys is low compared to Cu at room temperature, it increases to values near those of Cu at 500°C.

Following consolidation, consolidated 2/1 Nb samples were tested over a range of temperatures to determine the electrical resistivity of the consolidated materials. No aging treatment was used since it was expected that all the Cr and Nb would be precipitated from the Cu matrix. The results are shown in Figure 61. Instead of the expected straight line for heating and cooling, the alloys show a very different resistivity following exposure in the temperature range of 450°C to 500°C. The temperature range corresponds to the range normally used to precipitate Cr in Cu-Cr alloys. The alloys showed a decrease in resistivity along a straight line following exposure. The values of resistivity were again converted into thermal conductivities. The results appear in Figure 62.

These results indicate that the elemental Cr precipitates in the materials were placed in the Cu solid solution during the hot rolling process. The rolls of the hot rolling mill acted as a quench media to remove the heat from the materials too fast to allow precipitation to occur. During subsequent testing to determine the resistivities of the materials, the Cr was able to precipitate from the matrix, lowering the resistivity considerably. Retesting of the materials showed that the resistivities followed the lower curve determined during cooling.

The presence of oxides in the material as a result of the consolidation processing increased the electrical resistivities of the alloys slightly, but the overall effect was not large. This is because the oxygen was present as stable oxides, i.e. Cr_2O_3, rather than dissolved in the Cu matrix. With better processing the oxides can be eliminated and the conductivities increased to the values observed for the ribbons.

Table 17
Temperature Coefficients for Resistivity for Cu-Cr-Nb Alloys and Cu

Alloy	Temperature Range		
	25°C - 550°C (μohm·cm)	25°C - 100°C (μohm·cm)	450°C - 550°C (μohm·cm)
Cu	0.006316	.003470 (0.0043)*	0.006167
2/1 Nb	0.01889	0.009780	0.02219
Cons. 2/1 Nb (Heating)	0.005503	0.006369	0.006179
Cons. 2/1 Nb (Cooling)	0.007547	0.005216	0.008661
4/2 Nb	0.01760	0.008600	0.02102
6/3 Nb	0.01105	0.00633	0.01354
8/4 Nb	0.005753	0.003511	0.005884
10/5 Nb	0.007465	0.003333	0.008480

* - From Reference (164)

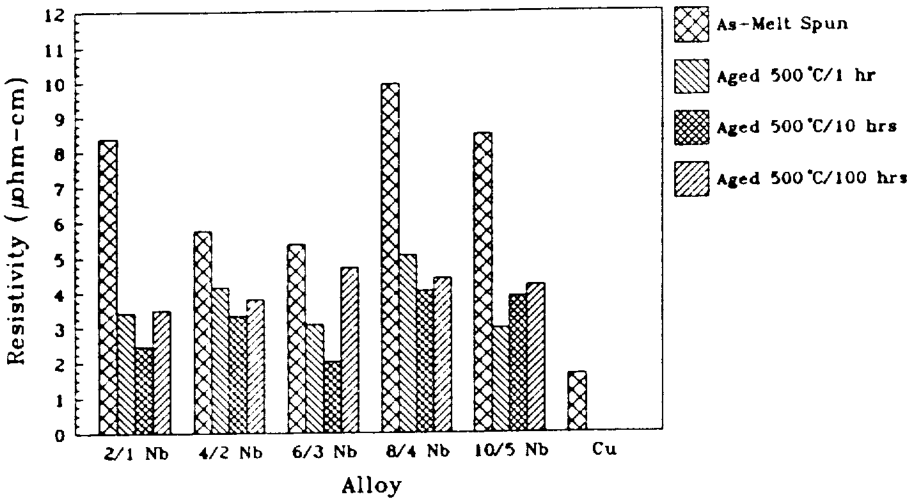

Figure 52 - Effect of Aging on Room Temperature Resistivities of Melt Spun Cu-Cr-Nb Ribbons

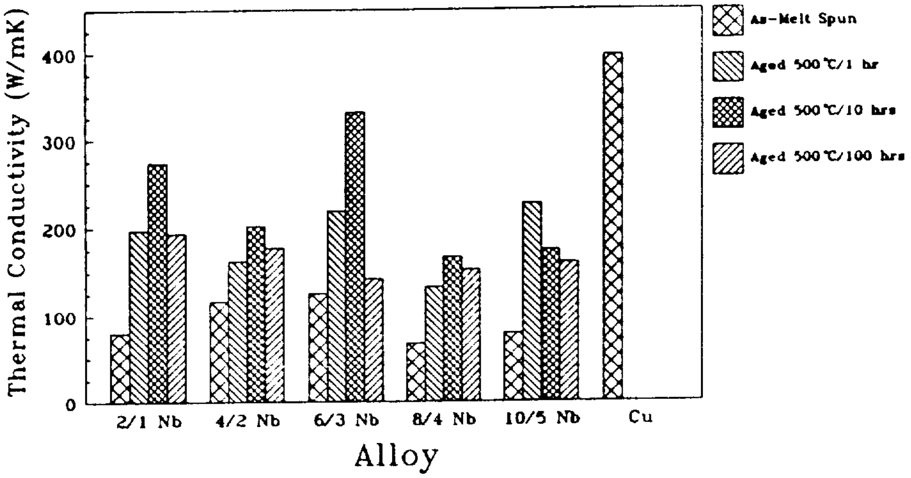

Figure 53 - Effect of Aging on Room Temperature Thermal Conductivity of Melt Spun Cu-Cr-Nb Ribbons

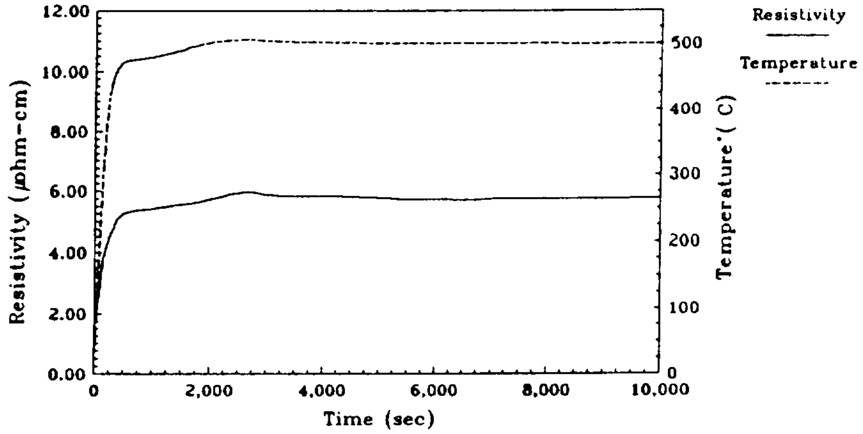

Figure 54a - Variation of Electrical Resistivity with Aging at 500° C for Cu

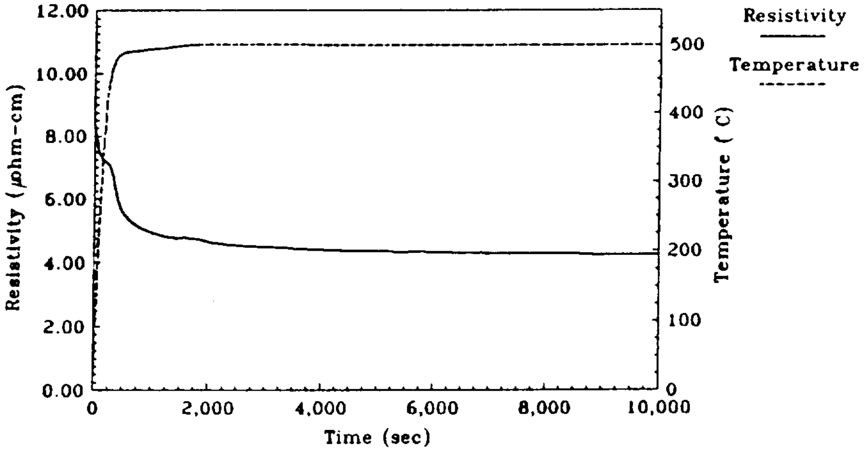

54b - Variation of Electrical Resistivity with Aging at 500° C for 2/1 Nb

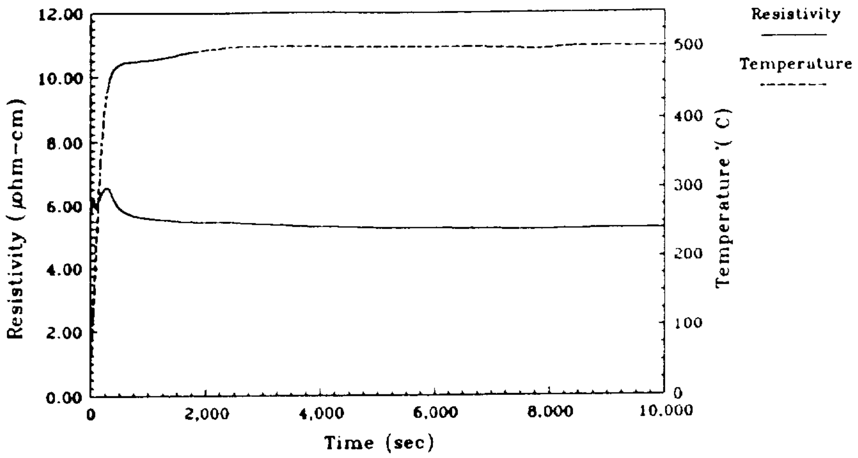

54c - Variation of Electrical Resistivity with Aging at 500° C for 4/2 Nb

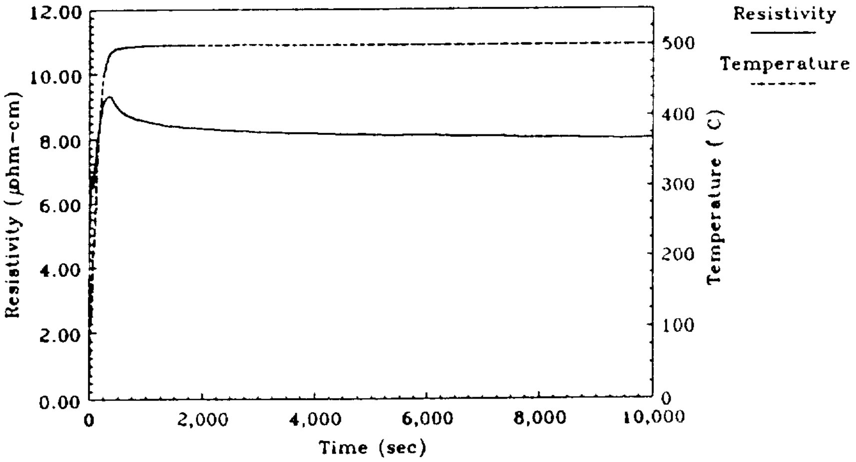

54d - Variation of Electrical Resistivity with Aging at 500° C for 6/3 Nb

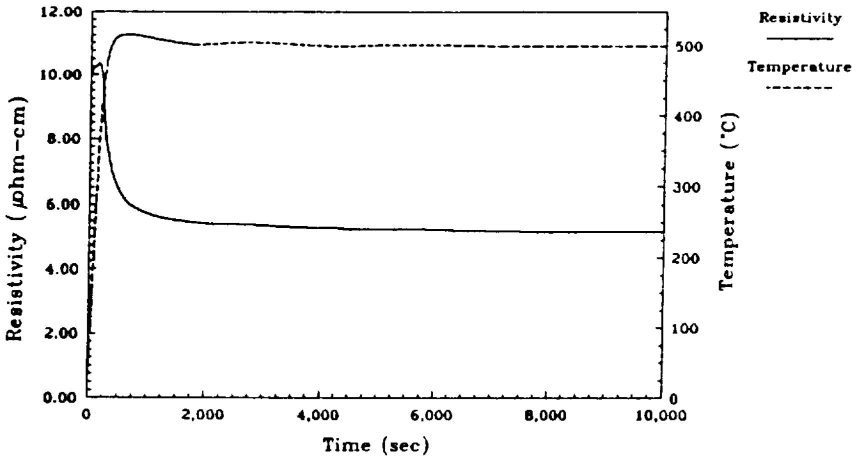

54e - Variation of Electrical Resistivity with Aging at 500° C for 8/4 Nb

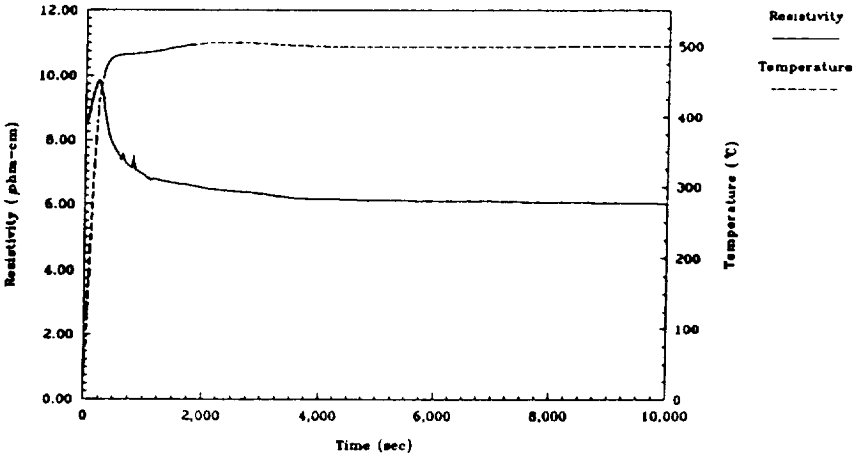

54f - Variation of Electrical Resistivity with Aging at 500° C for 10/5 Nb

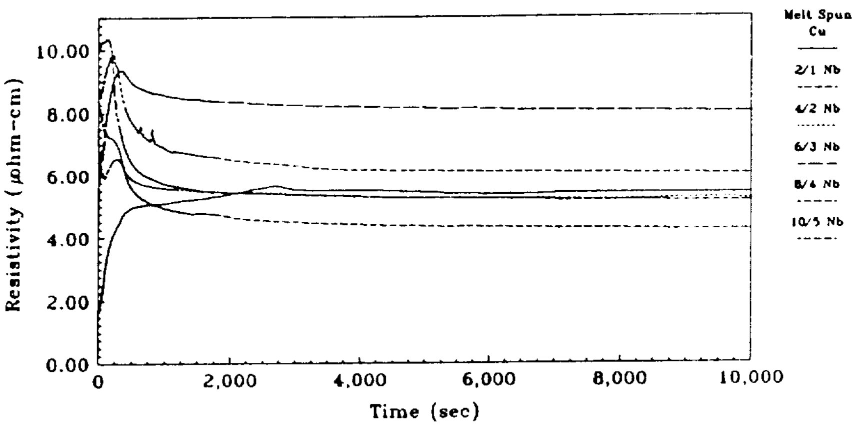

Figure 55 - Summary of Effect of Aging at 500° C on Electrical Resistivity of Cu-Cr-Nb And Cu Ribbons at 500° C

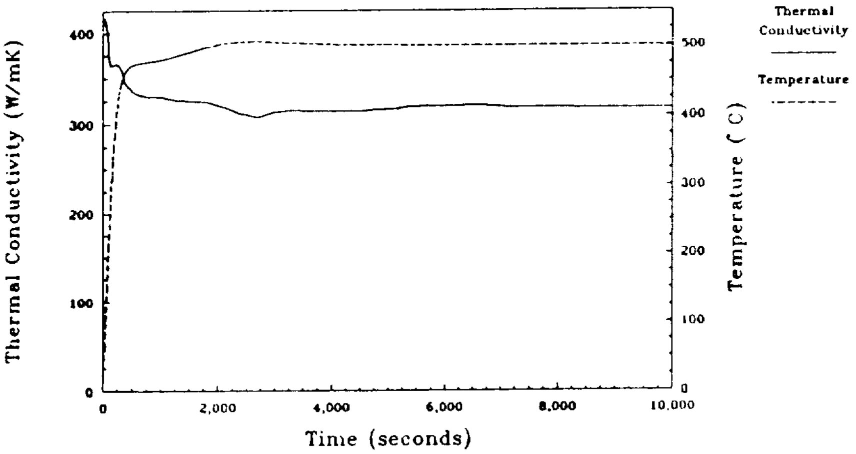

Figure 56a - Variation of Thermal Conductivity with Aging at 500° C for Cu

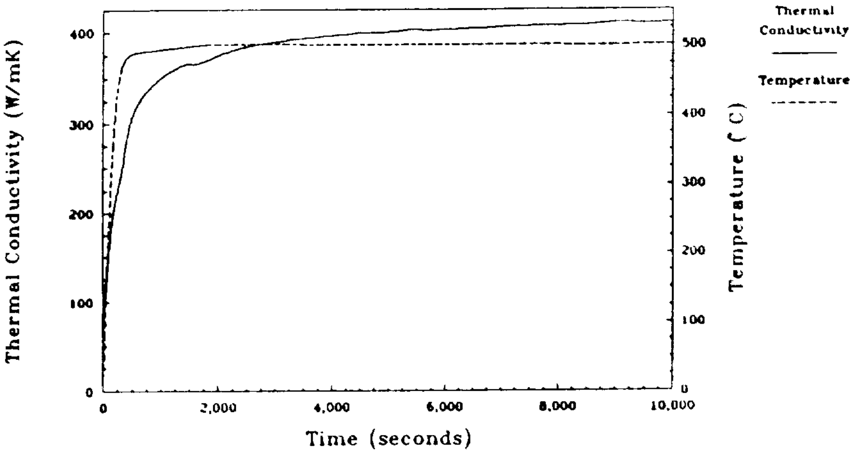

56b - Variation of Thermal Conductivity with Aging at 500° C for 2/1 Nb

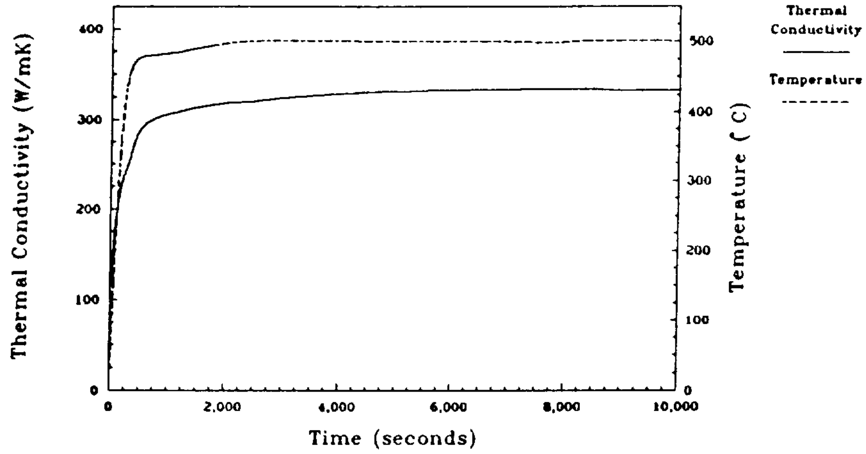

56c - Variation of Thermal Conductivity with Aging at 500° C for 4/2 Nb

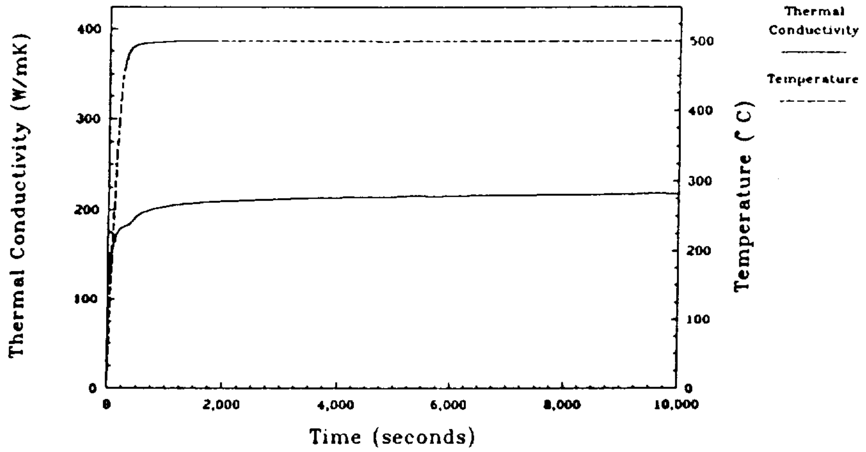

56d - Variation of Thermal Conductivity with Aging at 500° C for 6/3 Nb

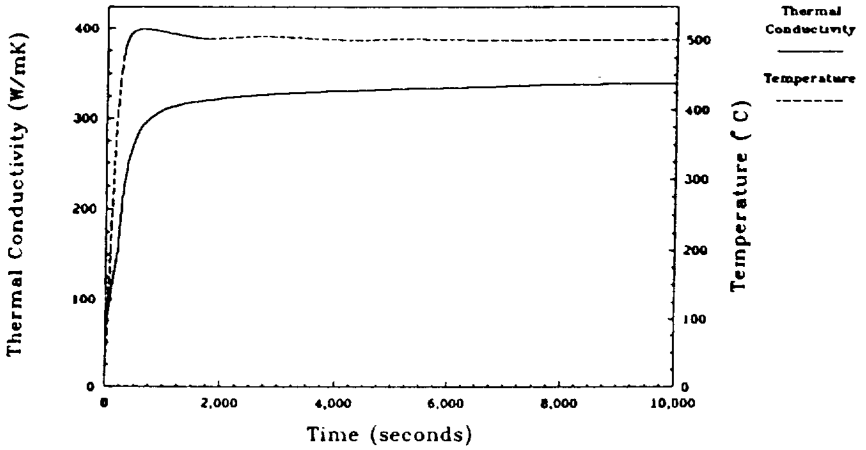

56e - Variation of Thermal Conductivity with Aging at 500° C for 8/4 Nb

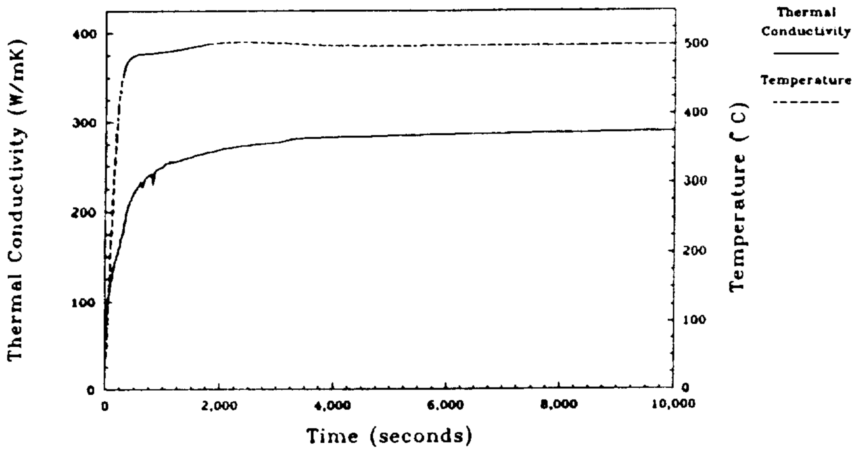

56f - Variation of Thermal Conductivity with Aging at 500° C for 10/5 Nb

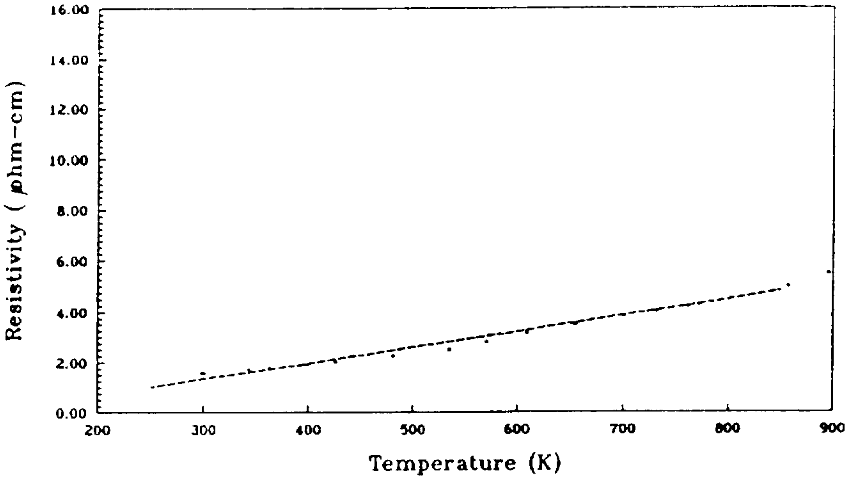

Figure 57a - Variation of Electrical Resistivity with Temperature for Cu

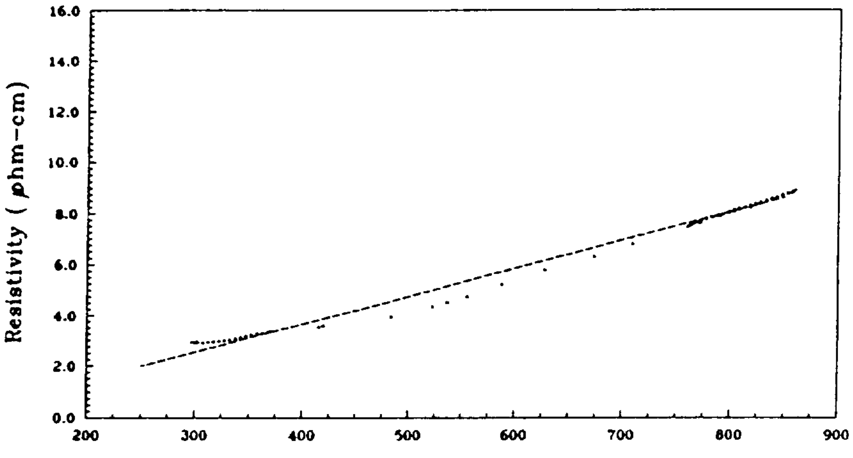

57b - Variation of Electrical Resistivity with Temperature for 2/1 Nb

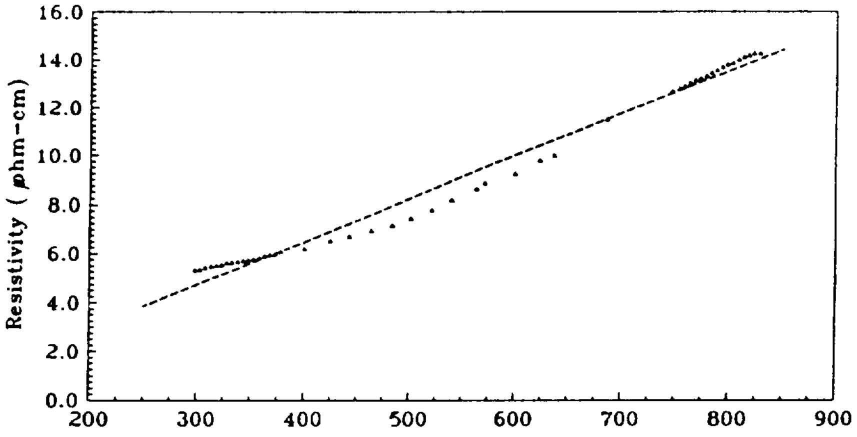

57c - Variation of Electrical Resistivity with Temperature for 4/2 Nb

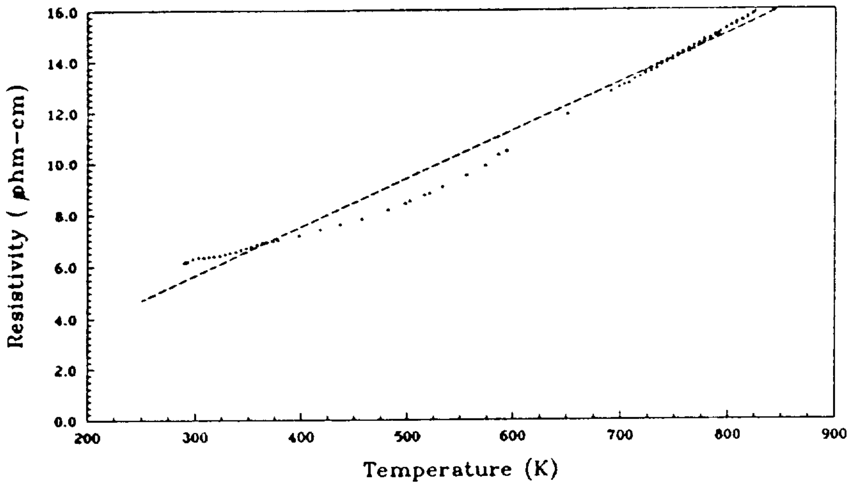

57d - Variation of Electrical Resistivity with Temperature for 6/3 Nb

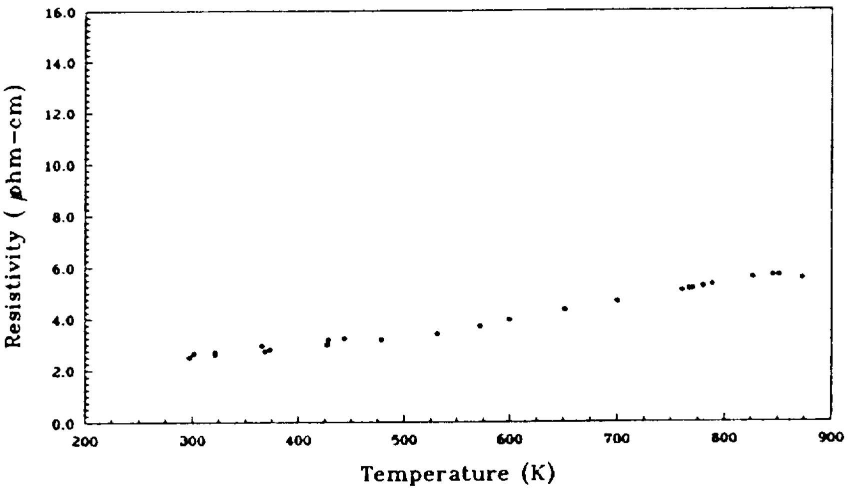

57e - Variation of Electrical Resistivity with Temperature for 8/4 Nb

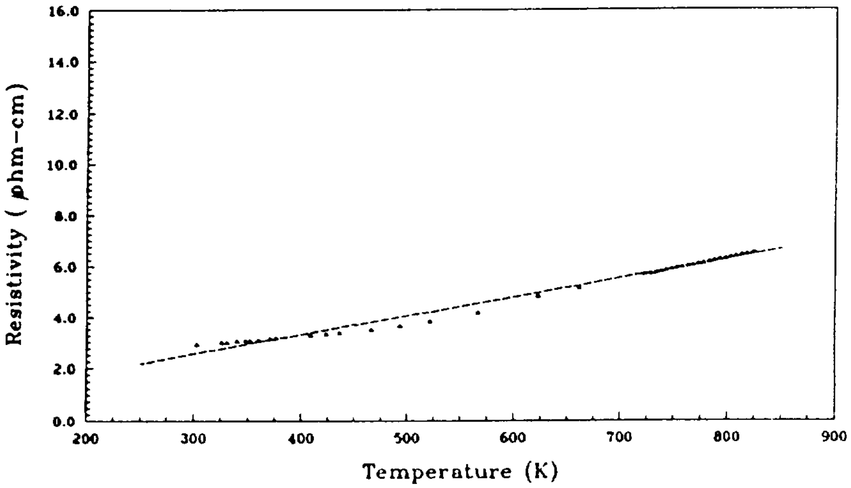

57f - Variation of Electrical Resistivity with Temperature for 10/5 Nb

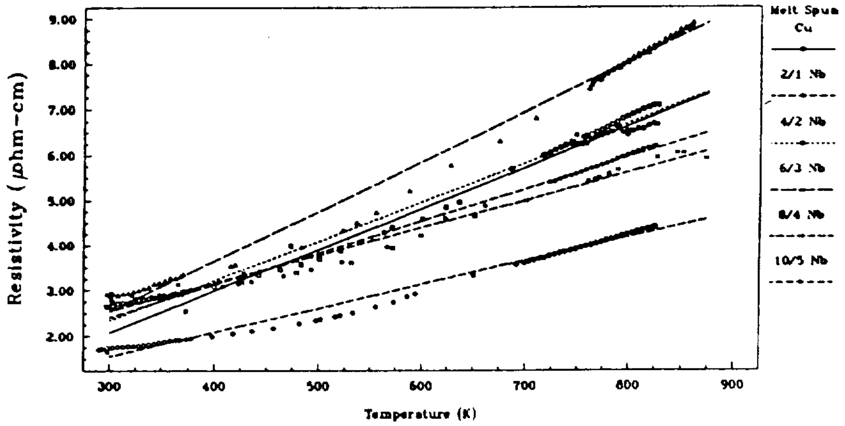

Figure 58 - Summary of the Effect of Temperature on Electrical Resistivity for Melt Spun Cu-Cr-Nb and Cu Ribbons

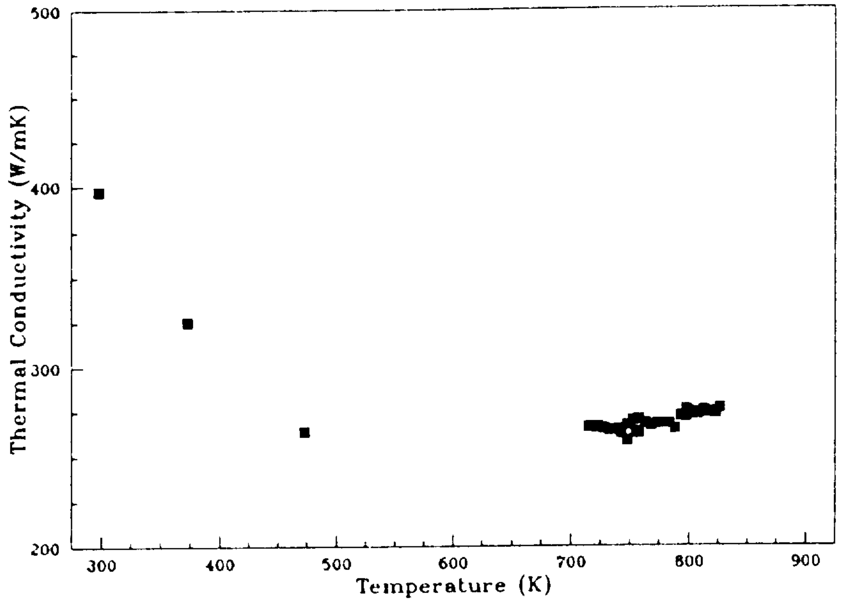

Figure 59a - Variation of Thermal Conductivity with Temperature for Cu

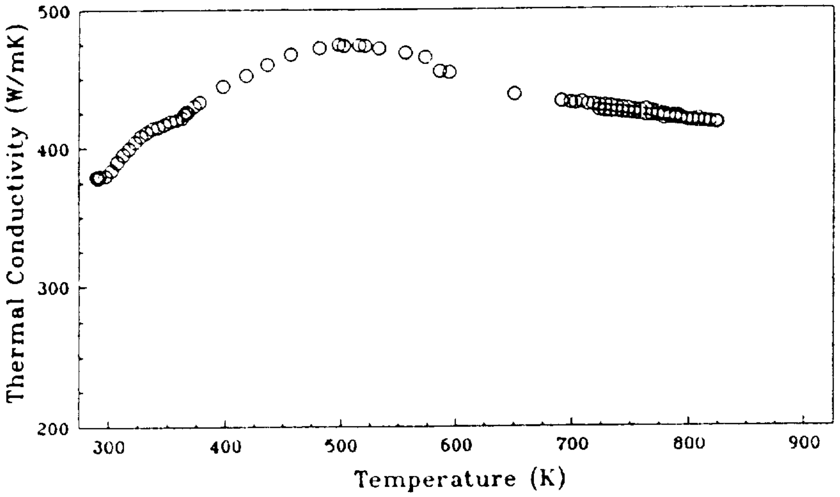

59b - Variation of Thermal Conductivity with Temperature for 2/1 Nb

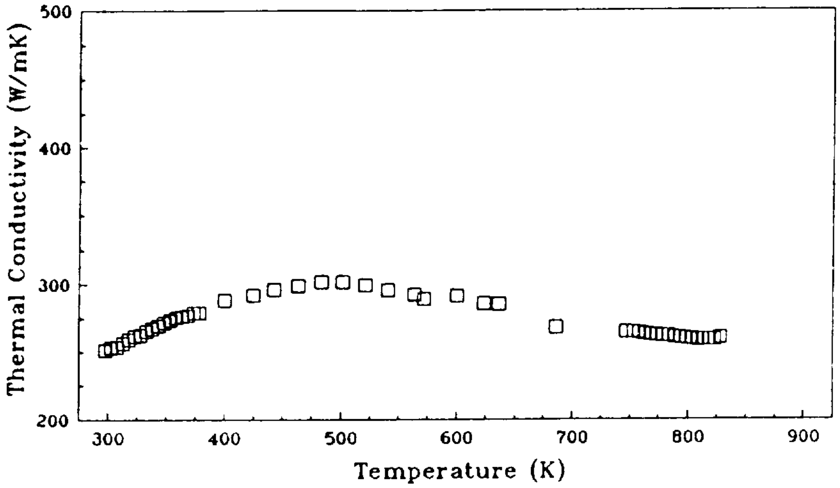

59c - Variation of Thermal Conductivity with Temperature for 4/2 Nb

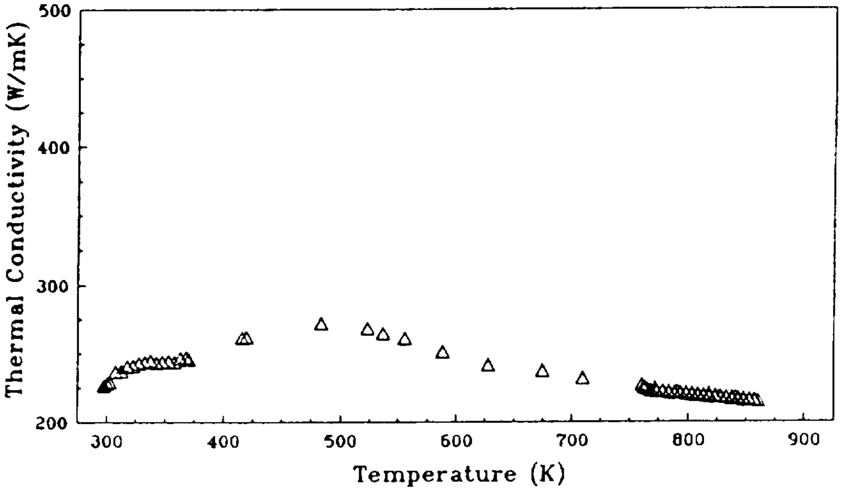

59d - Variation of Thermal Conductivity with Temperature for 6/3 Nb

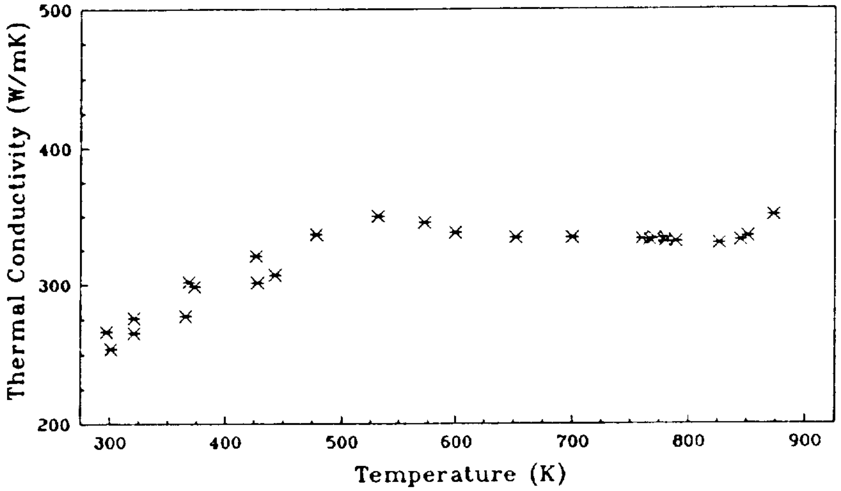

59e - Variation of Thermal Conductivity with Temperature for 8/4 Nb

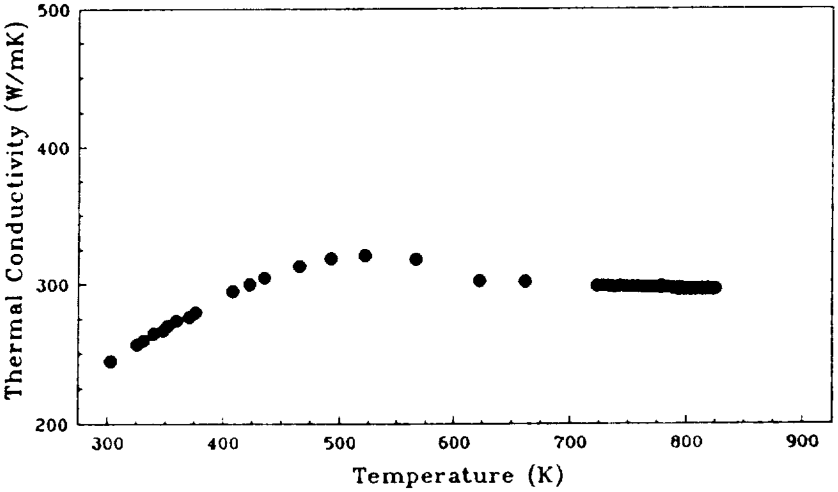

59f - Variation of Thermal Conductivity with Temperature for 10/5 Nb

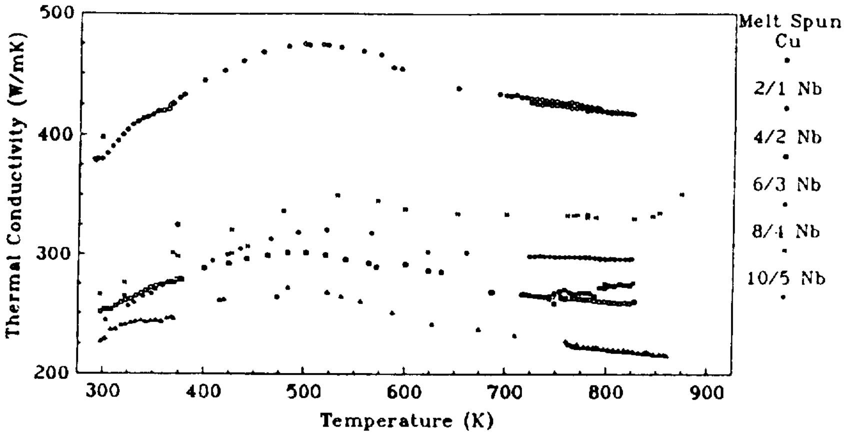

Figure 60 - Summary of Variation of Thermal Conductivity with Temperature for Melt Spun Ribbons

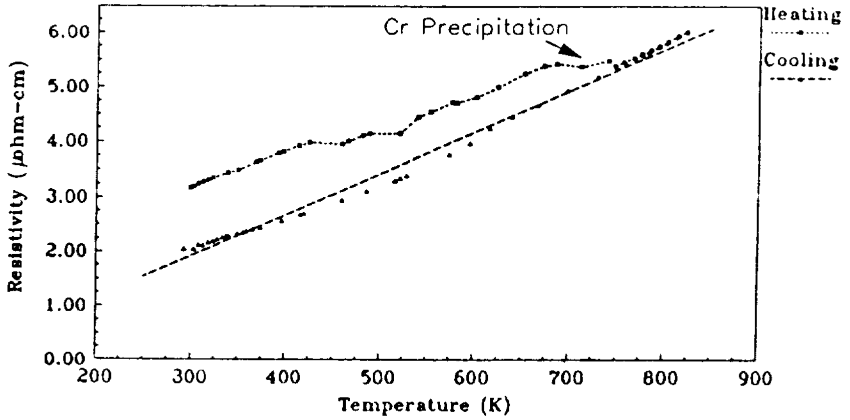

Figure 61 - Variation of Electrical Resistivity with Temperature for Consolidated 2/1 Nb

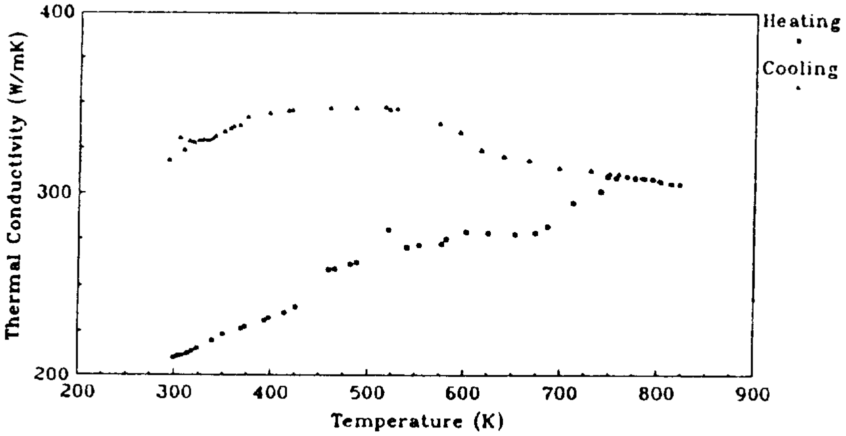

Figure 62 - Variation of Thermal Conductivity with Temperature for Consolidated 2/1 Nb

5 Discussion

From the results of the tests, several observations can be made with regards to the stability of the Cr_2Nb phase, the resistance to coarsening of the Cr_2Nb precipitates and Cu grains. The strengths and electrical resistivities of the materials relative to other materials can be discussed. Comments can also be made with respect to the consolidation processing of the materials.

5.1 Calculation of Cooling and Solidification Rates During Melt Spinning

The cooling and solidification rates for the alloys could not be directly measured. However, good estimates of the two rates were obtained from observations of the melt spin videos and ribbons.

To estimate the cooling rates, the melt spin videos were examined to determine the length of ribbon extending from the melt puddle that showed any signs of radiance. In all cases for all alloys this length was effectively zero. The lack of any detectable radiance in the material exiting the melt puddle indicates that the temperature of the material is between 500°C (932°F) and 700°C (1292°F). For this analysis a value of 500°C was chosen. The temperature of the molten metal supplied to the melt puddle was assumed to be equal to the temperature of the melt given the short time between exiting the crucible and impacting the wheel. These assumptions established the limits for the temperature.

To determine the time it took for the molten metal solidify and cool to 500°C, the size of the melt puddle was measured from the melt spin video. The melt puddle was 5 mm or less. By dividing the length of the melt puddle by the surface speed of the wheel, 20 m/sec, the time required to cool the molten metal to 500 °C was obtained. Dividing the temperature decrease by the time required to cool the material leads to a minimum cooling rate of 4.2 X 10^6 K/sec.

Tenwick and Davies (169) examined the cooling rates for Cu and Cu-Zr alloys at wheel speeds of 8 m/s and 35 m/s. Their technique used calibrated measurements of the density of photographic negatives of the melt spinning process to determine the temperature of the molten metal and ribbon during the melt spinning process. Their results indicate that while the ribbon was in intimate contact with the wheel, the cooling rate was 4 X 10^5 K/s for a wheel speed of 8 m/s and 5 X 10^6 K/s for a wheel speed of 35 m/s. Following the ribbons leaving the wheel, the cooling rate was between 7.5 and 32 X 10^5 K/s.

The calculated cooling rates for the Cu-Cr-Nb alloys falls reasonably close to the values of Tenwick and Davies. Assuming an approximately linear relationship between the cooling rate and wheel speed, a value of 2.4 X 10^6 is obtained using Tenwick and Davies values. This is low by a factor of about 2 compared to the calculated value for Cu-Cr-Nb. Tenwick and Davies' photographs clearly show that the ribbon was radiating light when it left the wheel. This indicates that the cooling rates for Tenwick and Davies materials were less than the cooling rates for the Cu-Cr-Nb alloys. From this the estimate of 4.2 X 10^6 K/s for the cooling rate is judged to be a reasonable value.

To determine the solidification rate, the thickness of the ribbons were measured to determine the distance that the solidification front passes through. The time that it takes the solidification front to move through this distance was determined by dividing the size of the melt spin puddle by the wheel speed. The solidification rate was calculated by dividing the maximum thickness of the ribbons as measured with flat anvil micrometers by this time. The calculated solidification rates are consistently in excess of 10 m/s and most are near 16 m/s.

5.2 Microstructural Stability of Cu-Cr-Nb Alloys

Since the properties of the material depend on the microstructure, changes in the microstructure with time or processing could have severe adverse effects on the physical and conductive properties. As part of this study, the effects of aging at 500°C and processing on the microstructure of the materials were examined. Particular attention was paid to the coarsening of the Cu grains and the Cr_2Nb precipitates.

5.2.1 Cu Grain Size

Zener (170) examined the dependency of grain coarsening on the size and volume fraction of a precipitate. The basic equation developed is

$$\bar{R} = \frac{4r}{3f} \qquad [77]$$

where

$\bar{R}$ = average radius of curvature of the grains

r = average radius of the precipitates

f = volume fraction of precipitates

From this simple equation, it is possible to calculate the critical size of the grains above which grain growth will not occur. Using this model, the critical grain size of the ribbons is 0.5 μm or less. As such, the Cu grains were not expected to grow. Comparing the sizes and volumes for the Cu grains in the melt spun and aged conditions shows that the values are equivalent. Deviations in the values for the grain sizes are taken to represent the inherent variations in the grain size of the materials due to differing cooling rates in the ribbons combined with the statistical inaccuracies associated with a small sample size. From this, the conclusion can be drawn that the grain size of the ribbons will not increase during thermal exposure at temperatures up to 500°C for times up to 100 hours.

For the consolidated materials, it is difficult to determine the Cu grain size because of the etching behavior of the materials. Qualitatively, it is evident that the Cu grain sizes are on the same order of magnitude as the melt spun and aged ribbons. Some of the samples exhibited isolated signs of recrystallization and grain growth. Those samples still had Cu grain sizes near the Cu grain sizes of the ribbons and non-recrystallized consolidated materials.

Calculating the grain size of the material based on an average precipitate size of 100 nm shows that the critical grain size is 5.3 μm. This would represent a considerable increase in the average size of the Cu grains. This is consistent with the observations of recrystallization and grain growth in same samples. It also indicates that degradation of the mechanical properties at low temperatures could occur through grain growth. However, since grain boundary sliding is one mechanism for the failure of materials at elevated temperatures, grain growth may in fact improve the high temperature mechanical properties of the materials.

In contrast, the Cu sample prepared as a comparison to the Cu-Cr-Nb alloys shows significant recrystallization and grain growth following the consolidation process. The grain size of the samples has increased to an average diameter of 56.7 μm. The effect of the precipitates in stopping the growth of the Cu grains is thus readily apparent.

The small grain size of the materials has both beneficial and detrimental effects associated with it. Beneficial effects include increased ductility and strength. For applications near room temperature this would give the alloys an advantage over alloys with coarser microstructures. Detrimental grain boundary sliding can occur at elevated temperatures leading to a loss in strength. The linear decrease in strength up to 750°C is taken to indicate that grain boundary sliding is not a major problem over that temperature regime. Another detrimental effect that the presence of many grain boundaries could have on the high temperature properties of the materials is the enhanced diffusion along the grain boundaries leading to increased creep rates in the temperature/stress regimes where diffusional creep mechanisms are operational. No creep testing was performed to determine if this would in fact be a problem.

Overall the results indicate that the Cu grain size of the material is controlled by the initial grain size produced during melt spinning. No significant increases in the Cu grain sizes occur during aging or consolidation. The probability exists that the Cu grains of the consolidated materials will coarsen following thermal exposure to a value between 1 and 5 μm.

5.2.2 Cr_2Nb Precipitate Size

Coarsening of the precipitates is a potential problem since the strength of a material is dependent on the precipitate size as outlined in Section 2.2.2. The results of the study indicate that the precipitates underwent considerable coarsening, but the degree of coarsening was not sufficient to degrade the mechanical properties below acceptable values.

The initial Cr_2Nb precipitate size was small, approximately 10 nm for all of the alloys. After aging at 500°C for 100 hours, the size of the precipitates in the 4/2 Nb alloy increased to only 20.6 nm. The increase is significant and does result in overaged material, but the microhardnesses of the materials do not show a decrease to values below the initial as-melt spun values or to values near pure Cu.

The consolidated material was subjected to much higher temperatures during the consolidation processing; 650°C for 1 hour plus heating and cooling and ≈920°C for up to 2 hours. The temperature of 940°C is near the eutectic temperatures ofboth the Cu-Cr and Cu-Nb systems. As such a significant amount of Cr and Nb could dissolve in the Cu. This would promote more rapid formation and coarsening of Cr_2Nb precipitates. Even under these conditions, the precipitates only grew to sizes in the 100 nm to 400 nm range. As will be discussed in Section 5.6.2 and 5.6.5, the mechanical properties of the materials were very good. Under these conditions, the conclusion is that while a smaller precipitate would be desirable, the sizes obtained through the consolidation process used in this study are still acceptable.

The results from the 500°C aging and the consolidation work indicate that the precipitate sizes can be kept reasonably small through proper processing. A processing method such as extrusion where high stresses and short times at temperatures are possible could result in a reduction in the size of the precipitates and improved mechanical properties. Once the precipitates are formed, the results from the aging study indicate that they will not coarsen greatly during subsequent exposure at 500°C.

5.2.3 Phase Change in Cr_2Nb Precipitates

From the phase diagram, it was known that Cr_2Nb has both a high temperature hexagonal and a low temperature FCC phase. The lattice parameters and structure of both have previously been documented. Duwez and Martin (25) had already shown that the transformation kinetics for the isomorphic Cr_2Ta compound were slow. One of the objectives of this study was to see if the Cr_2Nb would undergo a phase change during isothermal aging or the consolidation processing.

The SAD patterns for the aged and consolidated materials are shown in Figures 43 and 44. The patterns clearly show that the FCC form of Cr_2Nb is not present in any of the samples either following aging or consolidation.

The phase change of Cr_2Nb involves a change in the volume of the unit cells from 0.3274 nm^3 to 0.3415 nm^3. As such the transformation will produce a stress in the material. The stability of the precipitate and resistance to transformation is thus viewed as a benefit that will enhance long term mechanical properties.

5.3 Stability of Cr_2Nb Precipitates

One of the observations that came out of the study was the high stability of the Cr_2Nb precipitates in Cu-Cr-Nb alloys. This was seen be the difficulties experienced in dissolving the precipitates in liquid Cu during chill block melt spinning until the indicated temperature was above the melting point of Cr_2Nb and the moderate coarsening of the precipitates during consolidation.

Direct observations of the stability of the Cr_2Nb phase in liquid Cu came with the addition of a video camera to observe the melt during chill block melt spinning. The camera revealed that there was a solid phase floating on top of the liquid copper. The solid phase appeared as the Cu melted and persisted up to an indicated temperature between 1843°C and 1871°C (3350°F and 3400°F). The solid completely covered the surface of the liquid metal. The complete coverage of the top plus observations of solid being stirred in the material indicated that there was a considerable amount of the solid present in the melt.

The first possibility explored in identifying the solid was that the solid was an oxide slag such as Cr_2O_3 that had formed during induction melting. The oxygen analysis of both the master melts and the melt spun ribbon indicated that there was some oxygen present and therefore some oxide, but not a significant amount. In addition, no slag was observed in the crucible or chamber following the melt spinning process.

The next possibility explored was the possibility of the solid being solid Cr_2Nb. Observation of the behavior of several alloys indicated that the solid disappeared on heating and reappeared during cooling during repeated thermal cycling between indicated temperatures of 1704°C (3100°F) and 1899°C (3450°F). It was believed that these indicated temperatures were almost 167°C (300°F) higher than the actual temperature of the sample. If this correction factor is taken into account, the temperatures observed are consistent with the melting of Cr_2Nb at 1733°C (3151°F).

No direct sampling of the melt to isolate the solid from the copper was possible, but samples that would not eject due to nozzle clogging were allowed to solidify in the crucibles. These samples were removed from the crucibles and prepared for metallographic examination. The sizes of the Cr_2Nb particles and the position in the casting were observed. The sizes of the solid particles in the molten material could be determined by calibrating the video image magnification from the size of the crucible and measuring several of the particles. The observed Cr_2Nb particles were approximately the same size as the observed solid particles. In addition, the Cr_2Nb precipitates in the casting were found primarily in the upper half of the casting. The density of liquid Cu is 8 g/cm^3 at 1083°C (1981°C) and decreases slightly with increasing temperature (171). While no data is available on the elevated temperature density of Cr_2Nb, it is reasonable to expect the density to decrease from it room temperature value of 8.09 g/cm^3. A moderate decrease in density for the Cr_2Nb would result in the density of Cr_2Nb being less than the Cu. The Cr_2Nb would thus float to the top of the melt. This is consistent with the observations of the melt. Based on these observations, the conclusion was drawn that the solid was in fact Cr_2Nb.

Another direct observation of the stability of Cr_2Nb in liquid Cu was observed during optical examination of the as-melt spun 10/5 Nb sample. The 10/5 Nb material prepared using the old, lower temperature melt spinning method showed a large chunk of Cr_2Nb in the ribbon. While this is the only piece of Cr_2Nb directly observed, the total amount of ribbon actually examined is very small, so finding even this one piece is significant.

The stability of Cr_2Nb in liquid Cu is further evidenced by the TEM of as-melt spun ribbons. Many precipitates identified as Cr_2Nb are observed in the ribbons. There size is typically 7.5 to 10 nm. The particles are randomly orientated with respect to the Cu matrix giving rise to the ring diffraction patterns. There are two possible reasons for the observed random orientation. The first possibility is that the Cr_2Nb has no possible orientation relationship with Cu. This is unlikely for any material. Observation of the atomic arrangements and spacing of atoms on the $\{111\}$ plane of Cu and $\{1 1 \bar{2} 0\}$ plane of Cr_2Nb reveals great similarities and a reasonable chance for an orientation relationship to exist. The more likely possibility is that the Cr_2Nb precipitates formed in the liquid phase.

To examine this second possibility, the size of a precipitate that formed in the solid during cooling after solidification was calculated. Since the diffusivity of Cr and Nb in solid Cu is much less than the diffusivity in liquid Cu, if the precipitates were much greater than the calculated size, then the precipitates must form in the liquid Cu.

The average diffusivity and the total flux of atoms to a precipitate were calculated for Cr and Cr_2Nb precipitates using the following assumptions. First, the temperature was assumed to decrease linearly from the solidification temperature at a rate of 10^6 K/s to 500°C with no significant diffusion occurring below 500°C. The upper temperature bound was assumed to be 100°C below the melting point of Cu to allow for some thermal undercooling of the material prior to solidification. The lower limit of 500°C was assumed based on the observation of no radiance from the material as it separated from the melt spinning wheel.

Second, the diffusivity of each element in solid Cu is given by equations 78a and b (85).

[78]a
$$D_{Cr} = 0.237 e^{\frac{-46,610}{RT}} \frac{cm^2}{s}$$

b
$$D_{Nb} = 2.04 e^{\frac{-60,060}{RT}} \frac{cm^2}{s}$$

where

R = gas constant (1.987 cal/mol K)

T = absolute temperature (K)

D_{Cr}, D_{Nb} = diffusivity of Cr and Nb respectively (cm^2/s)

Third, the melt spinning process was assumed to produce uniform Cr and Nb distributions in the ribbon.

The flux of atoms to the precipitates was approximated by assuming that half of the atoms in a sphere of radius $\sqrt{\overline{D}t}$ move to the center of the sphere to form the precipitates. Here $\overline{D}$ is the average diffusivity during cooling and t is the time to reach 500°C Finally, it was assumed that Cr and Nb were completely depleted at the precipitate/matrix interface.

The average diffusivity of each element during cooling can be calculated using the formula

[79] $$\overline{D} = \frac{\left\{ \sum_{\Delta t=0}^{n} \sqrt{D(T)\Delta t} \right\}^2}{\sum_{\Delta t=0}^{n} \Delta t}$$

where

$\overline{D}$ = average diffusivity during cooling

D(T) = diffusivity at temperature T

Δt = time increment (1 millisecond used)

n = number of time increments needed to reach lower temperature bound

Under these set of assumptions the average diffusivity of each element, the radius of the sphere of affected material, and the number of atoms moving to the growing precipitate, J, can be calculated. The results are listed in Table 18. The corresponding diameter of spherical Cr and Cr_2Nb precipitates containing the number of atoms were calculated. The results appear in Table 19.

The calculated values for the sizes of the precipitates represent an upper bound estimates since they ignore the incubation time needed for the nucleation of the precipitates in the solid phase and the interaction between closely spaced precipitates that would be expected.

Based on these calculations, the Cr precipitates with diameters greater than 29 nm and Cr_2Nb precipitates greater than 4 nm could not have formed during the cooling of the material after solidification. These larger precipitates must form in the liquid Cu where the diffusivities of Cr and Nb are much greater. Only the smaller precipitates that were found in the distribution of particle sizes could have formed in the solid Cu after solidification of the ribbons.

The TEM micrographs of the high alloy as-melt spun ribbons also gives considerable evidence that the Cr_2Nb precipitates form in the solid phase. Figure 40 shows large agglomerations of Cr_2Nb precipitates. The individual precipitates have sizes comparable to the precipitates in the lower alloyed materials. The observation of these agglomeration of the Cr_2Nb precipitates is consistent with the formation of Cr_2Nb precipitates in liquid Cu.

Additional evidence for the formation of solid precipitates in the liquid phase is given by Morris and Morris (68). They examined the closely related Cu-Cr system. During the examination of rapidly solidified a Cu-5% Cr alloy they observed several Cr precipitates on the order of 50 nm in size. Using the cooling rates for dilute Cu alloys measured by Tenwick and Davies (164) and the liquidi for both the hypoeutectic and hypereutectic alloys from Hansen (172), Morris and Morris applied the Wagner-Lipshitz-Slyozov equation for intergranular coarsening to determine the maximum size of Cr precipitates that can form in the solid Cu below 1000°C. The calculated values for the precipitates were on the order of 5 to 7 nm. Lower cooling rates for the ribbon still yielded precipitate only on the order of 10 nm.

The use of a coarsening model instead of a growth model is questionable since Morris and Morris reported considerable supersaturation of Cr in the Cu following melt spinning. If one uses a typical growth model such as the one outlined in Section 2.3.2, the particle sizes would increase as r^2 with respect to time instead of r^3. The particle size from this calculation is approximately twice the size of the values calculated by Morris and Morris. Even this larger value is not sufficient to explain the largest Cr precipitates observed. The analysis thus does tend to support the conclusion that elemental Cr can form in the liquid Cu even under the high cooling rate conditions of chill block melt spinning. The conclusion can be drawn that Cr_2Nb which melts at higher temperatures and was directly observed up to temperatures near the melt spinning would behave in a similar manner providing Cr and Nb could react to form Cr_2Nb in the short time available.

The existence of precipitates in the liquid melt is not unexpected given the large difference in the liquidus and solidus temperatures for the binary Cu-Cr and Cu-Nb alloys and the strong rejection of Cr and Nb from liquid Cu as temperatures approach the eutectic. The formation of Cr_2Nb was not expected considering the extremely short time the materials were at elevated temperatures. The presence of Cr_2Nb precipitates is indicative of a very strong driving force for the formation of Cr and Cr_2Nb precipitates. Given the strong driving force for the formation of Cr_2Nb and the slow diffusion of Nb in Cu, the stability of Cr_2Nb in the solid Cu should be good, and the precipitates should not coarsen to large sizes.

Table 18
Calculated Diffusivities, Characteristic Distances, and Flux for Cr and Nb During Cooling

Element	$\overline{D}(\times 10^{9}\frac{cm^2}{s})$	$\sqrt{\overline{D}t}$ (nm)	J (atoms)
Cr	75.37	67	1,020,000
Nb	1.39	9	629

Table 19
Corresponding Diameters of Cr and Cr_2Nb Precipitates Grown During Cooling Based on Diffusion of Cr and Nb Atoms

Element	Cr Precipitate (nm)	Cr_2Nb Precipitate (nm)
Cr	28.64	34.28
Nb	N/A	3.68

5.4 Effect of Alloying and Melt Spinning on Cu Lattice Parameter

One of the expectations of this study was that a large amount of Cr and Nb would be trapped in a supersaturated solid solution. The presence of Cr and Nb in the solid Cu lattice would change the lattice parameter of the Cu matrix. The isothermal aging electrical resistivity measurements indicate that considerable amounts of solute were present in the as-melt spun ribbons. The X-ray diffraction results do indicate an increase in the lattice parameter over the lattice parameter of pure Cu for the as-melt spun ribbons. However, the results for the aged ribbons are not consistent with respect to either themselves or the electrical resistivity measurements.

Vegard's Law (173) states that the lattice parameter for a random solid solution is directly proportional to the atomic percent solute present. It assumes that the solute and matrix elements form an ideal solutions. This is not a good assumption for the binary Cu-Cr and Cu-Nb solid solutions. However, the use of Vegard's Law allows for the estimate of the effect of Cr and Nb on the lattice parameter of the Cu matrix.

For Cr, the diameter of the atom is 2.26 percent smaller than the diameter of the Cu atoms based on the size of the atoms in BCC Cr (174). Using Vegard's Law, the lattice parameter of the Cu matrix would be expected to decrease somewhat. In contrast, the Nb atoms have a diameter 12 percent larger than the Cu atoms (169). Nb atoms in solid solution would strongly increase the Cu lattice parameter if present in solid solution.

Large numbers of Cu vacancies are present in the as-melt spun ribbons. The concentration of vacancies approaches 0.1 a/o near the melting point of Cu (168). The vacancies will act to contract the lattice and decrease the lattice parameter of the as-melt spun ribbons. During aging, the concentration of vacancies should decrease rapidly as the vacancies move to the surface and grain boundaries and are annihilated. The vacancies should therefore not affect the lattice parameters of the aged materials.

Ignoring the effects of vacancies, the lattice parameter change from solute in solid solution as a function of the atomic fraction is given by the equation

$$a_o = \sqrt{2}(0.25560 N_{Cu} + 0.24982 N_{Cr} + 0.28637 N_{Nb}) \tag{80}$$

where

a_o = lattice parameter of solid solution

N_{Cu} = atomic fraction Cu in the solid solution

N_{Cr} = atomic fraction Cr in the solid solution

N_{Nb} = atomic fraction Nb in the solid solution

The minimum and maximum lattice parameters of the materials can be calculated. The minimum lattice parameter would occur if all the Cr and none of the Nb was in solution. The maximum lattice parameter would occur if all of the Nb and none of the Cr is in solution. The results of the calculations for the five alloys are presented in Table 20.

For the melt spun ribbons, the vacancies could have a substantial effect on the lattice parameter. The lattice parameters of these alloys would be expected to decrease by approximately 0.05% based on the estimate that the effective size of the vacancies for Vegard's Law is half the diameter of Cu atoms and the volume fraction of vacancies is 0.001. The vacancies would be present for both the minimum and maximum lattice parameter cases for the as-melt spun ribbons. As such the values in Table 19 should be reduced accordingly when considering the as-melt spun lattice parameters.

Referring back to Table 12, all of the as-melt spun alloys have lattice parameters greater than the lattice parameter of pure Cu and, with the exception of 2/1 Nb, less than the maximum lattice parameter listed in Table 19. The 2/1 Nb alloy has a lattice parameter only 0.01% higher than the calculated maximum lattice parameter, a value within the experimental error of the results.

The lattice parameters of the alloys after aging for 100 hours at 500°C were nearly equal to the lattice parameter of pure Cu with the exception of the 6/3 Nb alloy. Most of the difference between the measured lattice parameters and the lattice parameter for pure Cu falls within the error of the measurements. Small amount of Cr in solution would also help to decrease the lattice parameter. From this analysis, the conclusion is drawn that these samples had the equilibrium amounts of dissolved Cr and Nb and vacancies in the Cu.

The 6/3 Nb alloy showed a smaller lattice parameter than the lattice parameter of pure Cu. It is believed from problems encountered with this alloy that some impurities are present that were not detected by the chemical analysis. This would account for the observed smaller lattice parameter and relatively high electrical resistivity.

From the electrical resistivity and microhardness data, the expectation was that the atoms in solution would precipitate after aging for approximately 1 hour. The results for the 1 hour and 10 hour ages do not show a rapid decrease in the Cu lattice parameter to values near the lattice parameter of solid Cu. While four of the alloys showed a decrease in lattice parameters between the as-melt spun samples and samples aged for 1 hour, the largest lattice parameters observed occurred for samples aged 10 hours. Most alloys also saw an increase in the lattice parameter between the samples aged for 1 hour and 10 hours.

These inconsistent results can come from several sources. Variations in the starting materials with respect to cooling rates and local solute concentrations would greatly alter the initial lattice parameter from sample to sample even in a given alloy. This would tend to affect the as-melt spun samples and samples aged for 1 hour more than samples aged for 10 or 100 hours. The introduction of oxygen and other gaseous species into the metal from the environment during the first few hours of aging could result in an increase in the lattice parameter. Some of the increase in the lattice parameters of samples aged 10 hour could be accounted for by this mechanism. By 100 hours, the hydrogen environment should remove all the oxygen from the metals surface and reduce the lattice parameters of the alloys.

Overall the results of the X-ray diffraction portion of the study are inconsistent and inconclusive. The only trend observed that corresponds to the expected behavior of the lattice parameter is the reduction in the lattice parameter from its initial value greater than the lattice parameter of Cu to a value equal to the lattice parameter of Cu after aging for 100 hours.

Table 20
Minimum and Maximum Lattice Parameters as Determined by Vegard's Law for the Compositions of the Alloys

Alloy	Minimum Lattice Parameter (nm)	Maximum Lattice Parameter (nm)
2/1 Nb	0.36131	0.36169
4/2 Nb	0.36119	0.36217
6/3 Nb	0.36101	0.36269
8/4 Nb	0.36087	0.36300
10/5 Nb	0.36080	0.36487

5.5 Changes in Microstructure with Alloying

The change in the microstructure of the melt spun alloys with increasing alloying are very pronounced. The Cu and 2/1 Nb ribbons have columnar Cu grains extending from the wheel side through the entire thickness of the ribbon to the free side. Occasional equiaxed grains are noted on the free surface side of the ribbons that formed on the surface of the melt puddle and are incorporated into the growing ribbon. In contrast the heavily alloyed 8/4 Nb and 10/5 Nb alloys have very fine equiaxed Cu grains. The intermediate 4/2 Nb and 6/3 Nb alloys have a mixture of the two types of microstructure, columnar near the wheel side and equiaxed near the free side.

While it is beyond the scope of this study to model the heat flow and temperature gradients in the melt puddle during melt spinning, some general observations can probably explain the observed microstructure. There is a strong gradient extending through the ribbon and molten metal from the wheel side to the free surface. The wheel side is effectively the temperature of the wheel. The free side is near the temperature of the melt. Under these conditions there is a strong driving force to solidify the alloy at the wheel surface. Initially the liquid Cu solidifies as many fine equiaxed grains at the wheel/melt interface. The Cu grains grow into the liquid metal, developing a columnar microstructure as certain orientations of grains outgrow other, less favorably orientated grains. This explains the microstructure for the Cu ribbons.

For the alloyed ribbons, it is important to remember that there are many fine solid Cr_2Nb particles dispersed through the liquid melt. The particles act as sites for heterogeneous nucleation of solid Cu grains in the melt. The ability of these particles to actually form a solid Cu grain of any appreciable size would be determined by the temperature gradients in the melt and the undercooling of the melt in the local region of the particle. The number and size of the Cr_2Nb particles would also be important.

For the 2/1 Nb, the volume fraction of Cr_2Nb particles is approximately 0.6% assuming all the Nb forms Cr_2Nb. The size of these particles are also small, typically 7.5 to 10 nm. The small number and size of the particles appears be unable to form a significant number of Cu grains in the melt. As a result, the columnar grains growing from the wheel side dominate the solidification process and a columnar microstructure develops.

For the most highly alloyed materials, 8/4 Nb and 10/5 Nb, where the volume fraction of Cr_2Nb particles is over 10%, there are many sites for the formation of Cu grains in the melt. In addition, while the individual Cr_2Nb particles are between 7.5 nm and 10 nm, they tend to agglomerate. This produces a larger surface locally to promote the formation of individual Cu grains. The result appears to be the formation of many submicron grains through the entire thickness of the ribbon. The wheel side develops the initial fine grained equiaxed grains, but before they can grow the ribbon has completely solidified. The result is a ribbon with a very fine grained microstructure.

The intermediate alloyed materials, 4/2 Nb and 6/3 Nb, show a columnar microstructure near the wheel surface and a a very fine grained microstructure near the free side. The transition from columnar to equiaxed is very abrupt. It is believed that the Cu initially solidifies at the wheel/melt interface and forms columnar grains that grow into the melt. The melt contains many fine Cr_2Nb particles present both as individual particles and agglomerations. With the undercooling of the melt, the Cr_2Nb particles can act as preferential sites for heterogeneous nucleation of Cu grains. These grains form in the melt some time after the columnar grains begin solidifying but before the complete solidification of the melt. The result is a combination of columnar and equiaxed microstructures.

One alternative to this hypothesis is that the material solidified in a columnar manner but the temperature of the metal and the amount of stress induced in the material by the thermal gradients across the thickness and along the length of the ribbons were sufficient to recrystalize the Cu. The Cr_2Nb particles would pin the grain boundaries as they attempted to grow. The increased volume fraction of particles with increased alloying would decrease the grain size. The presence of the equiaxed microstructure at the free surface side of the 4/2 Nb and 6/3 Nb alloys could be explained by the rejection of Cr and Nb into the melt during the solidification of the Cu to form even more solid Cr_2Nb particles. The particles would again promote the formation of equiaxed Cu grains as with the 8/4 Nb and 10/5 Nb alloys. Since it was impossible to selectively examine the samples at precise positions through the thicknesses of the ribbons, this mechanism can be neither confirmed or disproved.

5.6 Mechanical Properties

One of the most important criteria for the use of these alloys in the shuttle main engine and OTV rocket nozzles is strength of the material at elevated temperatures and the ability of the materials to maintain good mechanical properties for prolonged periods of time at these elevated temperatures. In this study the strength of the materials and the effect of aging on the materials' strengths was measured using room temperature microhardness measurements and tensile testing.

5.6.1 Microhardness

Microhardness measurements were used primarily for the ribbon samples since it was very difficult to perform a tensile test on the ribbon samples. Most of the attempts at tensile testing the ribbon resulted in the sample failing from just the weight of the bottom fixture.

The results of the aging study shown in Figure 45 show that the microhardness of the 2/1 Nb, and 8/4 Nb alloys increases with aging time at 500°C while the microhardnesses of the 4/2 Nb, 6/3 Nb and 10/5 Nb show a peak hardness at one hour with decreasing microhardness values thereafter. The decrease in microhardness from the peak value for 4/2 Nb and 10/5 Nb is only 27%. Only the 6/3 Nb shows significant reductions in strength with aging. The reduction of 47% from the peak strength indicates that the 6/3 Nb alloy sample aged for 100 hours at 500°C is the only badly overaged sample.

The presence of the peak hardness at one hour for three of the alloys is not totally unexpected. The electrical resistivity measurements shown in Figure 54 indicate that almost all of the solute atoms precipitate out in the first 0.5 hours. After that the volume fraction of the precipitates is effectively constant. The size of the precipitates would be increasing as time progressed due to coarsening. Most of the strengthening models predict that for constant volume fractions of precipitates, the coarsening of the precipitates would result in a decrease in strength and hence microhardness. This is consistent with most of the observations.

The fact that two of the alloys, 2/1 Nb and 8/4 Nb, did not experience maximum microhardnesses at one hour is interpreted to be a manifestation of the experimental procedure. One hour appears to correspond to a transition time when the nucleation and growth of precipitates has stopped and coarsening has started. The rate of change in the precipitate size is high at this transition time. Under those conditions, small variations in time, temperature, or material characteristics such as solute homogeneity could affect the exact time at which the transition from nucleation and growth to coarsening dominating the process occurs. No material was available to confirm this hypothesis, but it is expected that samples aged for 15 minutes and two hours would show significantly different microhardnesses compared to the one hour samples for all alloys.

The microhardness measurements also show a trend toward higher hardnesses with increasing alloying content. This represents an increase in hardness with increasing volume fraction of precipitates.

5.6.2 Yield and Ultimate Tensile Strengths

The yield and ultimate tensile strengths of the as-melt spun ribbons show a general increase with increasing alloying content. As with the microhardness measurements, this increase is caused by an increase in the volume fraction of precipitates.

While the results are good for the as-melt spun ribbons, the electrical resistivity and microhardness data indicates that the strengths of these ribbons could be significantly increased through aging. Looking at the microhardness data for 4/2 Nb, the microhardness of the sample has increased by nearly a factor

C - 3

of two. Since the microhardness is a function of the strength of the material and scales in an approximately linear fashion, the strength of a ribbon sample aged for 1 hour at 500°C can be estimated from the as-melt spun strengths and the microhardness data. Doing so indicates that the yield strength of the material would be 396 MPa (57.4 ksi) and the ultimate tensile strength would be 517 MPa (74.9 ksi).

The values for the ultimate tensile strengths of the ribbons are best thought of as lower limit bounds to the actual strength of the materials. The samples are known to undergo tearing. This would limit the ultimate tensile strength values through premature failure of the samples.

For the consolidated material, the values shown indicate lower limits to the values of strength and elongation for these alloys because of the presence of cracks in the material. As such, the materials actually has a lower load bearing area than the nominal cross-sectional area used for calculating the stresses. Failure is also through the propagation of a pre-existing crack rather than microvoid formation or some other mechanism associated with ductile materials. This decreases the ultimate tensile strengths of the materials.

The good short term tensile strengths of these alloys up to a temperature of 750°C is a manifestation of the high volume fraction and moderately fine, uniformly distributed precipitates. The presence of many grain boundaries does not appear to affect these materials too adversely over this temperature range. Precipitates on the grain boundaries may strengthen the grain boundaries and stop grain boundary sliding.

The uniformity of the strength levels even with varying volume fractions of precipitates is related to the interrelationship between the volume fraction and precipitate size as explained by the strengthening mechanism.

5.6.3 Strengthening Mechanism of Cu-Cr-Nb Alloys

One of the objectives of this research was to investigate the strengthening mechanism(s) of Cu-Cr-Nb alloys. Due to the high volume fraction of precipitates and their close spacing, it proved impossible to directly observe dislocation-precipitate interactions. Some mechanisms can be definitely ruled out and suppositions drawn for the remaining mechanisms.

During the analysis of several hundred TEM photographs of the various materials examined, there was never once any indications of shearing of the precipitates. This was true even in the consolidated materials following reductions of up to 80% by hot rolling. From this observation, all strengthening mechanisms that require the penetration of the precipitate by matrix dislocations can be ruled out. This means chemical strengthening, stacking fault energy strengthening, modulus strengthening, and order strengthening do not contribute to the strength of Cu-Cr-Nb alloys.

This leaves coherency strengthening and Orowan strengthening as the possible means for the precipitates to increase the strengths of the materials. Examination of Equation [34] for coherency strengthening shows that the strength of materials strengthened in this manner are proportional to $(r\,f)^{1/2}$ where r is the radius of the particles and f is the volume fraction. For Orowan strengthening, Equation [47] shows the strength of the material is proportional to $\frac{f^{1/2}\ln(r)}{r}$.

From these relationships, the effect of volume fraction and radius of the precipitates on the strengths can be examined. Looking at the as-melt ribbons, the strength of the 8/4 Nb ribbon relative to the strength of the 4/2 Nb ribbon can be calculated based on the volume fractions and precipitate sizes. The coherency strengthening model predicts that the strength of the ribbons should increase by a factor of 1.54. The Ashby-Orowan model predicts a more modest increase of 1.25. Examining the tensile strengths and microhardness data, the yield strength of the as-melt spun 8/4 Nb is 1.25 times the yield strength of the as-melt spun 4/2 Nb alloy. This is in excellent agreement with the predicted value for the Ashby-Orowan model. The microhardness data with the exception of the samples aged for 1 hour also shows a consistent ratio in the range of 1.22 to 1.33. This result is also consistent with the Ashby-Orowan model and too low for the coherency strengthening model.

Based on the results of the tensile tests and microhardness data, the primary strengthening mechanism of the Cu-Cr-Nb alloys is Orowan strengthening.

5.6.4 Ductility

Most Cu-based alloys exhibit good ductility. For example, annealed Cu has a ductility of 40% and a reduction in area of nearly 90% at room temperature. The Cu-Cr-Nb alloys do not have nearly this high a ductility.

The low observed ductilities in these alloys can be explained. For the ribbons tensile tested, the sample geometry tended to favor a localized plane strain condition. This in turn would result in greatly reduced elongations. The ribbons also tore easily, an observation consistent with the results of Morris and Morris (68). The tearing of the samples as opposed to necking leads to a reduction in the observed elongations. In most cases the samples showed less than 1% elongation, a value considered to fall in the experimental error associated with the measurements of the samples. Lack of uniformity in the cross-sectional area of the samples due to the topography associated with the free side of the ribbon also helped to limit the deformation of the samples.

The consolidated samples did not suffer from the problems associated with the ribbons. Rather, the observed low to medium ductilities observed are a manifestation of the lack of good bonding between the individual flakes, the presence of pre-existing cracks, and the presence of internal oxides.

Delamination of the samples is easily observed in both Figures 49 and 51. The optical micrograph shows a saw-tooth edge. There is also evidence of cracks extending back away from the fracture surface in a direction parallel to the applied load along the boundaries between the flakes. The decohesion of the flakes during the tensile test would have lead to the failure of the sample along flake boundaries transverse to the load.

The pre-existing cracks present in the samples because of poor consolidation in the hot pressing and hot rolling steps readily propagated through the samples during the tensile test. These cracks would limit the observed ductility of the samples by acting as stress concentrators to limit the deformation to a small volume of the sample rather than the entire gauge length. The pre-existing cracks were probably the most detrimental obstacle to observing good ductility in these alloys. Indeed, most samples could be seen to fail as a crack propagated from one side of the sample to the other. Further evidence was seen in the engineering stress-strain curves where the engineering stress would decrease in steps from the ultimate tensile strength during the failure of the sample.

The samples showed varying degrees of internal oxidation following consolidation. In the case of the more heavily alloyed materials, the internal oxides were observed on most flake surfaces. In addition to preventing the formation of good bonds between the flakes, the oxide particles act as stress concentrators, sites for the initiation of cracks, and easy paths for crack propagation. The combination of these problems leads to significant reductions in the ductility of the materials.

Even with these problems, the ductility of several of the samples is good. Some of the 8/4 Nb samples have elongations in excess of 10%. All of the alloys had fracture surfaces with at least some evidence of ductile features, i.e. dimples associated with the formation of microvoids. From this is assumed that if the problems associated with the processing of the materials can be remedied, the ductility of the materials should be more than acceptable.

5.6.5 Comparison to Other Cu Alloys

Several comparisons between the strengths of the Cu-Cr-Nb alloys and other Cu-based alloys are possible. The ones considered most important are the strengths of the ribbons compared to Cu, Cu-Cr, NARloy-A, and NARloy-Z and the consolidated materials to melt spun Cu processed in the same manner, conventional wrought NARloy-Z, Cu-Cr, Cu-Cr-Zr, Cu-Zr, GLIDCOP, and thoria dispersion strengthened Cu.

Figure 46 shows a comparison of the yield and ultimate tensile strengths for the alloys, Cu, and solution heat treated alloys of Cu-0.6 w/o Cr, NARloy-A, and NARloy-Z. The last three alloys show significant increases in their strengths following aging. Since the microhardness and electrical resistivity results indicate that the Cu-Cr-Nb alloys undergo considerable precipitation during aging, the comparison with solution heat treated materials is considered to be reasonable.

In the as-melt spun condition, the Cu-Cr-Nb alloys all have yield strengths much higher than Cu and Cu-0.6 w/o Cr. 2/1 Nb has a yield strength slightly higher than NARloy-A and slightly less than NARloy-Z. The remaining alloys all have yield strengths much greater than the conventional alloys. Ultimate tensile strengths for all except the 2/1 Nb alloy are greater than the ultimate tensile strengths of the four conventional alloys. Tearing of the samples as discussed earlier (Section 5.6.4) limits the ductility of the samples and promotes early failure of the samples. As such, the reported values are best taken as lower limit bounds to the actual ultimate tensile strengths of the materials in the as-melt spun condition.

Figures 47b and 47c show the strengths of the consolidated 2/1 Nb and 8/4 Nb as a function of temperature between room temperature and 850°C. Figure 47a shows the same data for Cu processed in the same manner as the Cu-Cr-Nb alloys. Figure 63 shows the dependency of strength on temperature for Cu-Cr, Cu-Cr-Zr, NARloy-Z, GLIDCOP, and thoria dispersion strengthened Cu as well as the ultimate tensile strength for the 2/1 Nb alloy for comparison.

Comparison between the figures indicates that the Cu-Cr-Nb alloys enjoy much greater strengths at temperatures above 600°C compared to all the alloys except the thoria dispersion strengthened Cu alloy. Even GLIDCOP does not have a significant advantage in strength. Problems associated with the consolidation processing detailed earlier may in fact cause a considerable lowering of the ultimate tensile strengths of the Cu-Cr-Nb alloys. Under these conditions, the strengths of the Cu-Cr-Nb alloys should be viewed as better than NARloy-Z, the current alloy used in rocket nozzles. Cu-Cr-Nb alloys are inferior to Cu-Cr and Cu-Cr-Zr at low temperatures but much better at temperatures above 500°C (932°F) and 600°C (1112°F) respectively. GLIDCOP has a slight advantage in strength up to 500°C, but has essentially the same strength up to 750°C. The thoria dispersion Cu alloy possesses the best high temperature strengths by far.

Based on this result, the goal of a better tensile strength at 500°C than NARloy-Z has been achieved. The values are some of the highest for the Cu-based alloys in the temperature range of 500°C to 750°C.

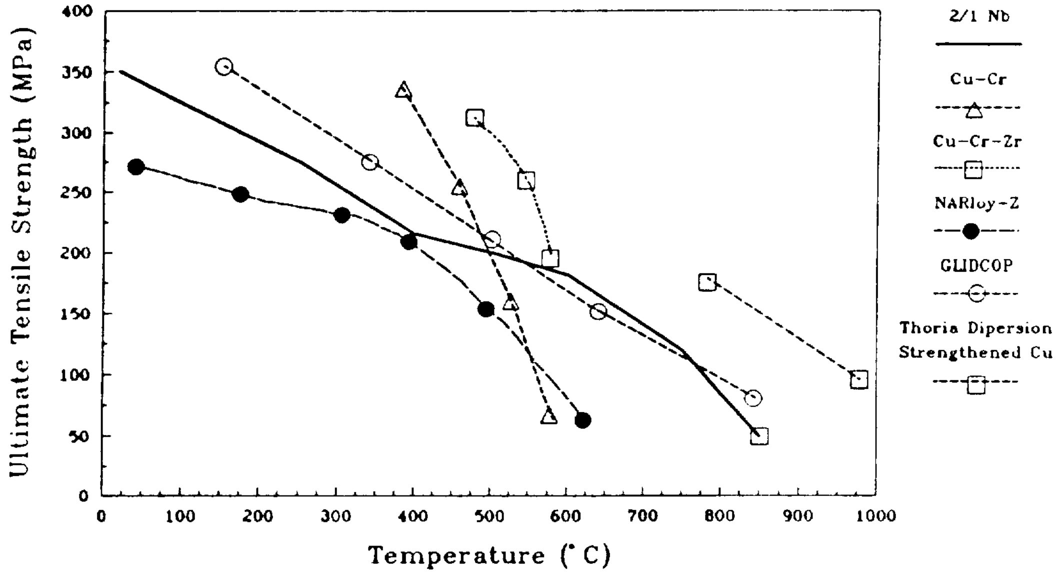

Figure 63 - Comparison of Ultimate Tensile Strength of 2/1 Nb to the Ultimate Tensile Strength of Several Cu-Based Alloys over the Temperature Range of 20°C to 1000°C. Cu-Based Alloy Values From References (86)

5.7 Thermal Conductivity of Cu-Cr-Nb Alloys

Since one of the primary objectives of this study is to develop a material with high thermal conductivity, it is important to understand the methods used to determine the thermal conductivities and the factors influencing the measurement and actual values of thermal conductivity.

5.7.1 Electrical Resistivity Measurements

The accurate measurement of the resistivity of highly conductive materials is difficult since all resistance measurements are based on a voltage drop across a section of the material. If the voltage drop is small as in the case of Cu and other conductive materials, considerable error can be introduced in the measurements.

To minimize this error, a large current can be supplied to produce a large voltage drop. Power dissipation in the sample was kept to less than 0.5 W to insure that the sample did not undergo resistance heating during testing.

Thermal gradients in the sample can induce small currents as electrons flow through the material from hot regions to cooler regions. These thermal currents also induce small voltage drops. By utilizing the larger currents, the error introduced in the measurements by these currents becomes insignificant. The error introduced by the thermally induced current is less than 0.2%.

The primary source of error in the measurement of the resistivity of the materials was variation in cross-sectional area due to irregularities in the free surface and the width of the ribbon. The variation in width was minimized by cutting the samples to a reasonably uniform width. To minimize the error introduced by this variation, short lengths of material were tested. The variation in thickness over these short lengths was typically 5% though values of 25% or more could occur in local regions. The overall effect on the cross-sectional area could not be accurately quantified, but the belief is that the error would be in the range of 5% to 10%.

For the relative changes in the resistivity of a sample, a ratio of the value to some base value of the sample would be very accurate. This is because taking the ratio of two values the ratio would cancel out the errors in the measurements of the dimensions of the samples. This method was not used since the literature tends to report absolute values of the resistivities and changes in resistivities. The reported changes in resistivity with temperature reflect this, and the accuracy of the values are limited by the accuracy in measuring the samples.

Even with the problems associated in accurately measuring the samples, it was possible to accurately reproduce the values for Cu listed in the literature for the melt spun Cu ribbons. For the Cu-Cr-Nb alloys where no literature is available for comparison. The values of the resistivity of the alloys increases at a rate slightly greater than linear. The values are greater than the resistivity for Cu, but fall in the range for many precipitation strengthened alloys such as Cu-Cr. From these observations the values are assumed to accurately reflect the resistivities of the alloys within the limits of error in the measurements with two exceptions.

The values for the 2/1 Nb ribbon are not representative of the actual resistivities of the alloys. In the case of the 2/1 Nb, the ribbon had a considerable amount of topography on the free side. The average of several values for the thickness was used to calculate the cross-sectional area of the ribbon. Given the deviation towards a much lower resistivity than Cu, the conclusion was drawn that the sample had a larger cross-sectional area than calculated. This would decrease the calculated electrical resistivity and increase the calculated thermal conductivity. The values for the consolidated 2/1 Nb following aging where the cross-sectional area is well known are more representative of the actual resistivity of this alloy.

For the 6/3 Nb alloy, the resistivity of the alloy is much higher than the other Cu-Cr-Nb alloys. From the observation of the Cu lattice parameter and the anomalous results for other portions of the study, the belief is that there has been contamination of the alloy by an undetected element or elements. This element would increase the resistivity of the material if it was in solid solution. This appears to be what has occurred.

5.7.2 Applicability of Wiedmann-Franz Law

Since the values actually desired were the thermal conductivities of the materials, it was necessary to convert the values of the measured resistivities. This was accomplished utilizing the Wiedmann-Franz Law.

The primary criterion for application of the Wiedmann-Franz Law is that the material must derive both its electrical conductivity and thermal conductivity from the movement of electrons through the material. Only under this condition can the measured values of the electrical resistivity be converted to meaningful thermal conductivities. Since Cu is the prime charge and thermal carrier, this criterion is obviously fulfilled. The next condition that must be met is knowledge of value of the Lorentz number.

The actual value of the Lorentz number for Cu-Cr-Nb alloys could not be determined since no thermal conductivity measurements could be made. The values for the Lorentz number for Cu and Cu-based alloys calculated from the literature (161) range from 1.30 X 10^{-8} watt-ohm/deg^2 for fully precipitation hardened Cu-0.6 Cr to 3.51 X 10^{-8} watt-ohm/deg^2 for a Cu-3 Si-1 Mn silicon bronze. Assuming that the Lorentz number for these alloys falls in this range, the maximum error for the thermal conductivities would be between -42% and +55%. Most of the alloys in the literature fall in a much narrower range from 2.2 to 2.6 X 10^{-8} watt-ohm/deg^2. This would give a error between -2.6% and +15%. The large deviations from the Lorentz number for Cu, especially for Cu-Cr and other dispersion or precipitation strengthened alloys, does make the value used somewhat suspect.

If one used the value for fully precipitation hardened Cu-0.6 Cr, the thermal conductivity of an alloy originally calculated to be 300 W/mK at 500° C would be only 174 W/mK. While this is still a large number compared to stainless steels, it is very low for Cu-based alloys. This value should be considered a lower bound.

If one looks at other precipitation strengthened alloys such as the Cu-Be-Co alloys, the deviation from the Lorentz number is in the positive direction. In example, fully hardened Cu-1.85 Be-0.25 Co has a Lorentz number of 2.60 X 10^{-8} watt-ohm/deg^2. If one uses this value for the Lorentz number, the thermal conductivity would increase from 300 W/mK to 345 W/mK.

Based on this analysis the Lorentz number plays a major role in the conversion from electrical resistivity measurements to thermal conductivities. The lack of good consolidated material prevented the testing of the material to determine the thermal conductivity and hence the Lorentz number for the alloys.

5.7.3 Effect of Excess Cr and Nb on Conductivity

While three of the alloys; 4/2 Nb, 6/3 Nb, and 8/4 Nb; had Cr to Nb ratios close to the ideal value of 2, the 2/1 Nb had a significant amount of excess Cr and the 10/5 Nb had a considerable amount of excess Nb. These two alloys allow for an examination of the effect of excess Cr and Nb on the electrical resistivity of these alloys.

The expectation from Matthiessen's Law (Section 2.6.3) is that the presence of excess Cr and Nb in the alloys would increase the resistivity of the alloys if these elements were in solution. Nb which has a much greater atomic radius than Cu (169) can be expected to be particularly harmful. The low solubility of these elements in solid Cu as indicated by the phase diagrams indicates that there should be a strong driving force for the precipitation of these elements from the Cu. If the Cr and Nb are present as discrete precipitates, the effect of excess Cr and Nb on the electrical resistivities would be much less.

Examination of the electrical resistivities of the ribbons show that, with the exception of the 6/3 Nb and 2/1 Nb samples, the electrical resistivities of the alloys at 500°C fall in a narrow band with the value being approximately equal to the value for pure Cu. The much lower value for the 2/1 Nb sample was explained by the much greater topography of the sample (See Section 5.7.1). Also as noted previously, the values for the 6/3 Nb alloy were anomalous and are therefore not considered here.

The results for the 10/5 Nb alloy indicates that excess Nb does not significantly affect the electrical resistivity of Cu-Cr-Nb alloys. Most probably the Nb precipitated from the Cu in either the solid or liquid and therefore does not decrease the electrical conductivity of the Cu matrix.

The results for the consolidated materials show a clear detrimental effect of Cr on the electrical conductivity of these alloys. The 2/1 Nb shows a higher than expected electrical resistivity initially. Upon heating, the resistivity increases with temperature until about 450°C. At this point the electrical resistivity decreases. Upon cooling the electrical resistivity decreases linearly along a straight line. Subsequent heating follows the same curve as the cooling curve.

Several observations lead to the conclusion that the excess Cr in each of the alloys was dissolved back into the Cu matrix and then precipitated again during subsequent heat treatments. The hot working temperature of the materials was at least 920°C. At this temperature there is a reasonably high solubility of Cr in solid Cu. Few if any Cr precipitates were observed in the consolidated material when they were examined in the TEM. The temperature at which the drop in resistivity occurred is near the lower temperature nose of the Cu-Cr TTT curve (175). The observed behavior of the alloys can thus be explained by the presence of Cr in solid solution increasing the electrical resistivity of the alloys. Subsequent precipitation decreases the electrical resistivities and eliminates this problem.

The results for the change in resistivity with temperature indicates that the 10/5 Nb is superior to the other four alloys. The presence of excess Nb in the alloy is probably a major contributor to this behavior. The excess Nb ties up the Cr as Cr_2Nb. The Cr can not dissolve into the matrix and increase the resistivity of the alloys. The solubility of Nb is so low at these temperatures that the amount of Nb that does dissolve into the Cu matrix is so slight that it does not significantly increase the resistivity. From this observation it might prove beneficial to the conductivity of the Cu-Cr-Nb alloys to have a Cr to Nb ratio slightly less than 2 to ensure complete reaction with the Cr.

5.7.4 Comparison of Conductivities of Cu-Cr-Nb Alloys to Other Cu Alloys

A graphical comparison of the electrical resistivities of several elements and alloys at room temperature and 500°C to the fully aged Cu-Cr-Nb alloys is presented in Figure 64.

The results show that the Cu-Cr-Nb alloys produced in this study have significantly lower resistivities than most elements and alloys. Only Ag, Au, and other Cu-based alloys come close. The values for the worst Cu-Cr-Nb alloy, 6/3 Nb, were still near 50% the thermal conductivity of pure Cu at 500°C. In comparison, most elements and alloys have less than 15% the thermal conductivity of pure Cu.

The best alloys tested have electrical conductivities in excess of 90% of the conductivity of pure Cu at 500° C. There are only a few alloys that are even close to this value.

At room temperatures the conductivities of the alloys are considerably lower than the value for pure Cu. This is consistent with the observations for other precipitation strengthened Cu-based alloys (86). At lower temperatures solute atoms, vacancies, dislocations, and very fine precipitates become the dominant factor in determining the thermal conductivity of the materials. For the precipitation strengthened alloys containing large amounts of solute, these factors greatly lower the thermal conductivities of the materials.

The Cu-Cr-Nb alloys produced by melt spinning enjoy a significant advantage in electrical conductivity over most materials and are comparable to the best electrical conductivity alloys at 500° C. The comparison between thermal conductivities is more ambiguous given the unknown value for the Lorentz number. The thermal conductivities are definitely much lower at room temperature than pure Cu and is probably comparable at elevated temperatures above 200° C (392° F).

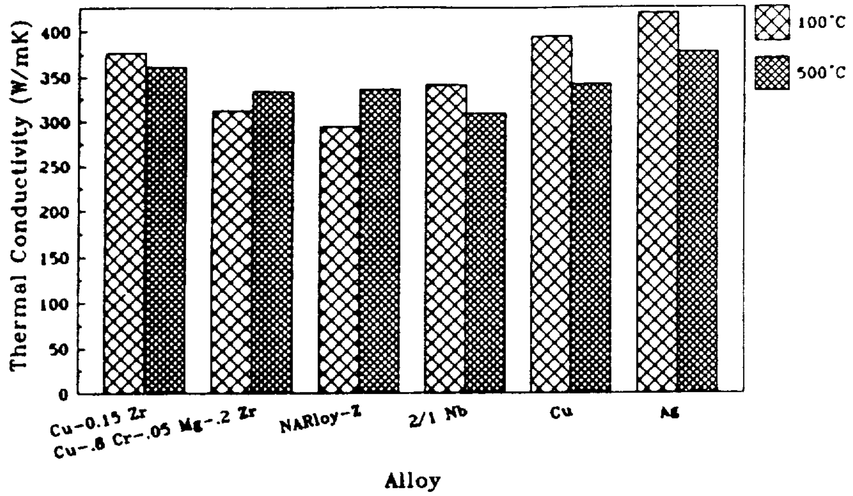

Figure 64 - Comparison of Thermal Conductivity of Consolidated 2/1 Nb to Other Elements and Alloys
From references (8), (86), and (161)

5.8 Consolidation of Material

Consolidation processing was done by a combination of hot pressing and hot rolling. The results were less than satisfactory. The materials showed considerable internal oxidation and cracking. The processing technique also lead to substantial coarsening of the Cr_2Nb precipitates. The microstructural and mechanical properties of the materials do indicate that the Cu-Cr-Nb alloys show considerable promise if a better processing method can be developed.

The first problem encountered in the consolidation processing was the non-uniform density of the samples following processing. The overall density of the materials was lower than desired, only about 85%. More importantly, the densities were readily seen to vary greatly from the center to edge. The problems associated with the low densities near the edges manifested themselves during the hot rolling step.

The initial hot rolling of the alloys was done with the samples in a stainless steel can with a He atmosphere. The materials were decanned after a 30%

reduction in the gap between the rolling mill rolls. The material was observed to be bright and shiny. Internal oxidation was minimal at this stage. Unfortunately metallographic samples taken from these materials following the 30% reduction showed considerable interconnecting porosity in the form of unclosed gaps between the flakes. During subsequent hot rolling in air these pores were oxidized prior to closure to develop the observed internal oxides.

Severe cracking of the material in the low density portions of the hot pressed samples was also observed. The pores acted as stress concentrators and sites for crack initiation. Once the cracks started, they easily propagated along the porous regions. The density differences are also suspected of causing considerable differences in the deformation of the sample. Since the denser central region is deformed by metal flow whereas the edges can deform by closure of the pores, a considerable stress gradient can be produced in the sample. The gradient would place the edges of the sample in tension and promote cracking.

Following decanning, the edges of the samples were trimmed to eliminate most of the cracks. Some cracks were left in the material since a more severe cut would have produced material lacking sufficient width for the tensile test samples. These cracks were observed during the rolling process. In general, the cracks were observed to increase in width in the rolling direction, but did not significantly propagate. Even with a 70% reduction in thickness, the cracks could not propagate across a 50 mm (2 inch) sample.

The last result may prove to be significant. Thermal fatigue is currently considered the prime problem facing the service life of rocket nozzles (6). Since thermal fatigue failure is caused by the propagation of a crack through the material, the inability of a crack to propagate to failure under the rolling conditions indicates the possibility of good thermal fatigue resistance.

6 Further Work

Most of the objectives of this study were reached. Cu-Cr-Nb alloys with very good high temperature strengths and conductivities were produced through chill block melt spinning. The results do indicate that there is still a considerable amount of work needed to produce a rocket nozzle though.

The specific recommendations for further work on the Cu-Cr-Nb system are as follows:

1. The current chill block melt spinning facilities are not designed for the production of large quantities of materials. Limits during this study were approximately 11 cm^3 or 100 grams for Cu-based alloys. To adequately evaluate the properties of the materials and allow experimentation in the consolidation of the materials, much greater volumes of materials are required. Current work is in progress to increase the volume of material to approximately 75 cm^3 or 700 grams. This amount of material is sufficient for one extrusion or the evaluation of several processing techniques or schedules on identical starting materials.
2. Consolidation processing of the material must be optimized to minimize precipitate coarsening and eliminate cracks and internal oxide. It is strongly suggested that extrusion or another consolidation technique that introduces large amounts of work into the flakes be attempted. The processing technique should also seek to minimize the time at temperature to minimize precipitate coarsening. The consolidation temperature should probably be above 800°C (1472°F), preferably 850°C (1562°F). Retesting of the consolidated material should then be carried out.

3. Aging of consolidated material should be carried out to determine the effects of aging on the Cr_2Nb precipitate size and Cu grain size. The high temperature properties of the materials following an aging treatment that promotes grain growth should be re-examined to see if the elimination of grain boundaries increases the high temperature strength.
4. The creep properties of the consolidated materials should be tested to determine if the grain boundaries increase the creep rate of the materials in the temperature/stress regime experienced by a rocket nozzle.
5. The thermal conductivities of the alloys should be tested directly to determine the Lorentz number of the alloys and the actual thermal conductivity values. One test for each alloy would be desirable, but a single test on one of the alloys other than 6/3 Nb should be sufficient to establish all the necessary values. While the value of the Lorentz number is not expected to be exceptionally different that the value for pure Cu, the large difference between the Lorentz numbers for Cu and Cu-0.6 w/o Cr is a concern since it indicates the possibility that the thermal conductivities of the alloys are lower than the calculated values.
6. The kinetics of the coarsening of the Cr_2Nb precipitates should be studied to better optimize processing and allow accurate prediction of the response of the materials to extended exposure at temperature.
7. A more careful analysis of the effects of Cr and Nb on the lattice parameter of the Cu matrix should be done to determine if there are any significant changes that would indicate microstructural changes occurring in the alloys.

7 Conclusions

The objective of this study was to investigate the possibility of strengthening Cu with the intermetallic compound Cr_2Nb. The end use of the material is to be rocket nozzles for the shuttle main engine and OTV. These uses required a material with high strength, good thermal conductivity, and good long term stability of the microstructure and mechanical properties. Chill block melt spinning was selected as the means best able to produce alloys with high volume fractions of very fine precipitates.

The results indicate that the Cu-Cr-Nb alloys can be produced through chill block melt spinning. Unfortunately the large driving force for the formation of Cr_2Nb made it impossible to produce a Cu-Cr-Nb solid solution. Instead most of the Cr and Nb was present as Cr_2Nb formed in the liquid during the melt spinning process.

The mechanical properties of the alloys are very good, especially at high temperatures. Compared to NARloy-Z, the current alloy used in rocket nozzles, the Cu-Cr-Nb alloys have approximately 100% higher yield strengths at 500°C. Or, if the strength of NARloy-Z at 500°C an acceptable value, the use temperature of the Cu-Cr-Nb alloys is nearly 750°C, an increase of 250°C. Increasing the operating temperature could lead to increased thrust-to-weight ratios for the engines.

The electrical resistivity measurements of the samples indicates that, like the other dispersion and precipitation strengthened Cu-based alloys, the room temperature electrical conductivity of the alloys is much lower than pure Cu. As the temperature increases though, the resistivity of Cu increases at a greater rate until the electrical conductivity of the better Cu-Cr-Nb alloys is greater than 90% the electrical conductivity of pure Cu at 500°C. The Wiedmann-Franz Law allows for the translation of these electrical conductivity values into thermal conductivities, the desired parameter. Unfortunately the conversion requires knowledge of the Lorentz number, a material specific number. While the value of pure Cu was used to approximate the value for the Cu-Cr-Nb alloys, the wide range of values for Cu-based alloys makes errors introduced in the conversions somewhat ambiguous.

Microstructural and property stability are required for the envisioned uses of these alloys. The Cu grains of the matrix did not undergo significant coarsening even under the influence of very high temperature and large amounts of work associated with the consolidation process. It was shown that the strong driving force for the precipitation of Cr_2Nb resulted in the materials overaging within approximately 1 hour at 500°C. Degradation of mechanical properties was not significant during subsequent aging at 500°C up to 100 hours. Consolidation of the materials required much higher temperatures. The result was precipitates approximately an order of magnitude greater that the precipitates in the melt spun ribbons. Again, the results indicate that the mechanical properties were most acceptable, and the overaging was not considered a major problem. The results do indicate that better consolidation processing techniques that minimize the coarsening of the precipitates may offer significant increases in mechanical properties.

The goal of this study was to produce a material with high strength, high conductivity, and good long term stability of mechanical properties and microstructure. These goals have been accomplished.

8 References

(1) A.V. Nadkarni, "Dispersion Strengthened Copper Properties and Applications", **High Conductivity Copper and Aluminum Alloys**, Eds. E. Ling and P.W. Taubenblat, TMS/AIME, Warrendale, PA, (1984), p. 77

(2) P.W. Taubenblat, W.E. Smith, and A.R. Graviano, "Properties and Applications of High Strength, High Conductivity Coppers and Copper Alloys", **High Conductivity Copper and Aluminum Alloys**, Eds. E. Ling and P.W. Taubenblat, TMS/AIME, Warrendale, PA, (1984), p. 19

(3) L.G. Peterson, D.W. Seaver, and A. Ritter, "Investigation of a P/M MZC Copper Alloy for Water-Cooled Gas Turbine Applications", Final Report, INCRA Project No. 337, International Copper Research Association, Inc., New York, NY, (Oct. 1983)

(4) N.J. Grant, A. Lee, and M. Lou, "Multiple Hardening Mechanisms for High Strength, High Temperature, High Conductivity Copper Base Alloys", **High Conductivity Copper and Aluminum Alloys**, Eds. E. Ling and P.W. Taubenblat, TMS/AIME, Warrendale, PA, (1984), p. 103

(5) T. Kameek, "Introduction - Thrust Chamber Material Development", **OTV Engine Technology Review**, Pratt & Whitney Engineering Div., West Palm Beach, FL, (March 1986)

(6) R. Dreshfield, NASA Lewis Research Center, private communications

(7) **Metals Handbook, Desk Edition**, H.E. Boyer and T.L. Gall, Eds., ASM International, Metals Park, OH, (Nov. 1984), pp. 16·5-16·15

(8) **Smithells Metals Reference Book, Sixth Edition**, "14.1 The Physical Properties of Pure Metals," E.A. Brandes, Ed., Butterworths, London, (1983), pp. 14-1 to 14-5

(9) **Smithells Metals Reference Book, Sixth Edition**, "14.3 The Physical Properties of Aluminum and Aluminum Alloys," E.A. Brandes, Ed., Butterworths, London, (1983), pp. 14-14 to 14-17

(10) **Smithells Metals Reference Book, Sixth Edition**, "22.2 Mechanical Properties of Copper and Copper Alloys," E.A. Brandes, Ed., Butterworths, London, (1983), pp. 22-22 to 22-51

(11) E. Shapiro and J. Crane, "Optimizing Conductivity, Formability, and Relaxation Resistance in Copper Alloys", **High Conductivity Copper and Aluminum Alloys**, Eds. E. Ling and P.W. Taubenblat, TMS/AIME, Warrendale, PA, (1984), p. 53

(12) L. Guillet, Rev. Met., (1906), p. 3

(13) G. Hindrichs, Z. Anorg. U. Allgem. Chem., (1908), p. 59

(14) M.A. Hunter and F.M. Sebast, J. Amer. Inst. Metals, (1917-1918), p. 115

(15) F.R. Hensel and E.I. Larsen, "Chromium in Copper Alloys", Chromium, Vol. II, Ed. M.J. Udy, American Chemical Society, Reinhold Publishing Company, New York, (1956), pp. 315-318

(16) D.J. Chakrabati and D.E. Laughlin, Bulletin of Alloy Phase Diagrams, Vol. 5, No. 1, 1984

(17) R.P. Elliott, Armour Research Foundation, Chicago, Ill., Technical Report 1, OSR Technical Note OSR-TN-247, (August 1954), p. 19

(18) I.A. Popov and N.V. Shiryaeva, Zh. Neorg. Khim., Vol. 10, No. 6, (1961), pp. 2334-2340 in Russian. Translated as Russ. J. Inorg. Chem., Vol. 10, No. 6, (1961), pp. 1184-1187

(19) J.D. Verhoeven and E.D. Gibson, "The Monotectic Reaction In Cu-Nb Alloys", Journal of Materials Science, 13, (1978), pp. 1576-1582

(20) V.T. Petrensko, M.A. Tikhonovskii, A.P. Berdnik, A.I. Somov, M.M. Oleeksienko and V.M. Arzhavitin, Vopr. At. Nauki Tekh., Ser. Obshch. Yad. Fiz., 9, (1979), pp. 20-24. In Russian.

(21) D.J. Chakrabati and D.E. Laughlin, Bulletin of Alloy Phase Diagrams, Vol. 2, No. 4, 1982

(22) O. Kubaschewwski and A. Schneider, "Measurements on the Oxidation-Resistance of High-Melting Point-Alloys", J. Ins. Metals, Vol. 75, (1948), p. 410

(23) V.N. Eremko, G.V. Zudilova, and L.A. Gaevskaya, Voprosy poroshkovoi metallurgi i prochnosti metallov (Problems of Powder Metallurgy and the Strength of Metals), Moskva, Izd. AN SSSR, (1958), p. 376

(24) H.J. Goldschidt and J.A. Brand, J. Less-Common Metals, Vol. 3, No. 1, (1948), p. 44

(25) P. Duwez and H. Marten, "Crystal Structure of $TaCr_2$ and $CbCr_2$", J. Of Metals, Vol. 4, (Jan. 1952), pp. 72-74

(26) R.M. Paine, A.J. Stonehouse, and W.W. Beaver, "An Investigation of Intermetallic Compounds for Very High Temperature Applications", Technical Report Tr 33 (616)-56-12, Wright Air Development Division, (Jan. 1960), pp. 91-95

(27) K. Kuo, "Ternary Laves and Sigma-Phases of Transition Metals", Acta Metall., Vol. 1, (Nov. 1953), pp. 720-724

(28) D.J. Lloyd, "Precipitation Strengthening", Strength of Metals and Alloys (ICSMA7), Vol. 3 (Proc. Conf.), Pergamon Press, Headington Hill Hall, Oxford, UK (1985), pp. 1745-1778

(29) J.C. Williams and A.W. Thompson, "Strengthening of Metals and Alloys," Metallurgical Treatises, J.K. Tien and J.F. Elliot, Eds., TMS/AIME, Warrendale, PA, (1981), pp. 487-504

(30) J. Friedel, "Les Dislocations", Gauthier-Villars, Paris, France, (1956)

(31) L.M. Brown and R.K. Ham, "Strengthening Methods In Crystals", A. Kelly and R.B. Nicholson eds., Halsted Press Div., John Wiley and Sons, New York (1971)

(32) S.D. Harkness and J.J. Hren, Metall. Trans., Vol. 1, (1970), p. 43

(33) V. Gerold, "Dislocations In Solids", F.R. Nabarro, Ed., North Holland, The Netherlands, (1979)

(34) V. Gerold and K. Hartmann, Trans. Japan Inst. Metals, Vol. 9 (Supplement), (1968), p. 509

(35) I. Kovacs, J. Lendvai, T. Ungar, T. Turmezey, and G. Groma, Acta Metall., Vol. 25, (1977), p. 673

(36) G. Knowles and P.M. Kelly, "Effect of Second-Phase Particles On The Mechanical Properties Of Steel", The Iron and Steel Institute, London, England, (1971), p. 9

(37) A. Mellander and P.A. Persson, Acta Metall., Vol. 26, (1972), p. 969

(38) K. Hanson and J.W. Morris, Jr., J. Appl. Phys., Vol. 46, (1975), p. 983

(39) T. Ungar, J. Lendvai, I. Kovacs, G. Groma, and F. Kovacs-Csetenyi, Z. Metallk., Vol. 67, (1973), p. 683

(40) B. Noble, S.J. Harris, and K. Dinsdale, Metl. Sci., Vol. 16, (1982), p. 425

(41) V. Gerold and H. Haberkorn, Phys. Stat. Sol., Vol. 16, (1966), p. 675

(42) H. Gleiter, Z. Agnew. Physik, Vol. 23, (1967), p. 108

(43) M. Witt and V. Gerold, Scripta Met., Vol. 3, (1969), p. 321

(44) J.M. Oblak, D.F. Paulonis, and D.S. Duvall, Metal. Trans., Vol. 5, (1974), p. 143

(45) J.M. Oblak, D.S. Duvall, and D.F. Paulonis, Mater. Sci. and Eng., Vol. 13, (1974), p. 51

(46) M.C. Chaturvedi and D.W. Chung, Metal. Trans., Vol. 12A, (1981), p. 77

(47) D.J. Bacon, S.J. Harris, and K, Dinsdale, Matl. Sci., Vol. 16, (1982), p. 425

(48) N. Hansen, Acta Metall., Vol. 18, (1970), p. 137

(49) M.F. Ashby, Oxide Dispersion Strengthening, AIME Conference Proceedings, New York, NY, (1966), p. 143

(50) U.F. Kocks, Phil. Mag., Vol. 13, (1966), p. 541

(51) T.J. Koppenaal and D. Kuhlmaan-Wilsdorf, Appl. Phys. Letters, Vol. 4, (1964), p. 59

(52) N. Bultner and E. Nembach, "Deformation of Multi-Phase and Particle Containing Materials", Proc. 4th Risφ. Sympo., Risφ National Labs., Roskilde, Denmark, (1983), p. 189

(53) G. Neite, M. Sieve, M. Mrotzek, and E. Nembach, "Deformation of Multi-Phase and Particle Containing Materials", Proc. 4th Risφ. Sympo., Risφ National Labs., Roskilde, Denmark, (1983), p. 447

(54) A.J.E. Foreman and M.J. Makin, Phil. Mag., Vol. 14, (1966), p. 911

(55) R.E. Reed-Hill, Physical Metallurgy Principles, Second Edition, D. Van Nostrand Co., (1973), p. 368

(56) R.E. Reed-Hill, Physical Metallurgy Principles, Second Edition, D. Van Nostrand Co., (1973), p. 499

(57) I.M. Lifshitz and V.V. Slyozov, "The Kinetics of Precipitation from Supersaturated Solid Solutions," J. of Physics and Chem. of Solids, Vol. 19, (1961), pp. 35-50

(58) J.W. Christian, The Theory of Transformations in Metals and Alloys, 2nd Edition of Part I, Pergamon Press, Oxford, (1975)

(59) Smithells Metals Reference Book, Sixth Edition, "13 Diffusion in Metals," E.A. Brandes, Ed., Butterworths, London, (1983), pp. 13-1 to 13-8

(60) D.R. Gaskell, Introduction to Metallurgical Thermodynamics, Second Edition, McGraw-Hill Books, New York, NY, (1981), pp. 409-521

(61) CRC Handbook of Chemistry and Physics, 65th Edition, R.C. Weast, Ed., CRC Press, Boca Raton, FL, (1984), pp. F-20 to F-35

(62) Wrought Beryllium Copper, Brush Wellman Engineered Material, Cleveland, OH (May 1984), p. 16

(63) S. Rolle and H.M. Schleicher, "Some Oxygen Free Coppers", Metals & Alloys, Mar 1940, p. 82

(64) R.C. Crosby and D.H. Desy, "Dispersion Strengthening in Copper-Alumina and Copper-Yttria Alloys," Bureau of Mines, R.I. 7266, June 1969, (E4854)

(65) K.R. Karasek and J. Bevk, "High Temperature Strength of *In Situ* Formed Cu-Nb Multifilamentary Composites", Scripta Met., 13, (1979), pp. 259-262

(66) "GlidCop, A Commercially Available Dispersion Strengthened Copper," Glidden Metals, Div. of SCM Corp.

(67) M.A. Morris, E. Batawi, and D.G. Morris, "Mechanical Properties of Rapidly Solidified Copper Alloys: Dependence on Composition and Microstructure," Matl. Sci. and Eng., Vol. 98, (1988), pp. 479-482

(68) M.A. Morris and D.G. Morris, "Microstructure and Mechanical Properties of Rapidly Solidified Cu-Cr Alloys," Act Met., Vol. 35, No. 10, (1987), pp. 2511-2522

(69) P.W. Taubenblat, V.J. Marina, and R. Batra, "High Strength High Conductivity AMZIRC Copper & AMAX-MZC Alloy," Wire Journal, (Sept. 1979), p. 114

(70) M. Appelo and P. Fenici, "Solution Heat Treatment of Cu-Cr-Zr Alloy," Matls. Sci. and Eng. A, Vol. 102, (1988), pp. 69-75

(71) E. Batawi, M.A. Morris, and D.G. Morris, "Microstructural Stability of Rapidly-solidified Cu-B Alloys," Matls. Sci. and Eng., Vol. 98, (1988), pp. 161-164

(72) Materials Properties Manual, 4th Ed, Rockwell International, Rocketdyne Division, (Oct. 1987)

(73) H. Suzuki, M. Kanno, and I. Kawakatsu, "The Strength of Copper-Zirconium-Chromium Alloy in Relation to Its Aged Structure," Nippon Kinzoku Gakkai-shi, Vol. 33, No. 5, (1969), pp. 628-633. NASA Technical Translation N74-15171.

(74) R.W. Knights and P. Wilkes, "Precipitation of Chromium in Copper and Copper-Nickel Base Alloys," Met. Trans., Vol. 4, (Oct. 1973), pp. 2389-2393

(75) R.D. Williams, Trans. ASM, Vol. 52, (1960), p. 530

(76) W. Gruhl and R. Fischer, Z. Metallk, Vol. 46, (1955), p. 742

(77) B. Lynch, Ph. D. Thesis, Aston University, U.K.

(78) G.C. Weatherly, P. Humble, and D. Borland, Acta Metall., Vol. 27, (1979, p. 1815

(79) M.G. Hall and H.I. Aaronson, Acta Metall., Vol. 34, (1986), p. 1409

(80) M.J. Witcomb, U. Dahmen, and K.H. Westmacott, "The Coprecipitation of Cr_3P and Cr in Cu," Proc. of the 46th Annual Meeting of EMSA, G.W. Bailey, Ed., San Francisco Press, Inc., San Francisco, CA, (1988), pp. 764-765

(81) T. Kamijo, T. Furukawa, and M. Watanabe, "Homogeneous Nucleation of Coherent Precipitation in Copper-Chromium Alloys," Acta Metall., Vol. 36, No. 7, (1988), pp. 1763-1769

(82) D.R. Clarke and W.M. Stobbs, "The Crystallography of Interfaces in the Unidirectionally Solidified Cu-Cr Eutectic Alloy," Metal Sci., Vol. 8, (Aug. 1974), pp. 242-246

(83) M.J. Tenwick and H.A. Davies, "Enhanced Strength in High Conductivity Copper Alloys," Matls. Sci and Eng., Vol. 98, (1988), pp. 543-546

(84) D.D. Horn and H.F. Lewis, "Property Investigation of Copper Base Alloys at Ambient and Elevated Temperatures," AEDC-TR-66-72, (July 1965)

(85) D.B. Butrymowicz, J.R. Manning, and M.E. Read, Diffusion Rate Data and Mass Transport Phenomena for Copper Systems, Diffusion in Metals Data Center, Metallurgy Division, Institute for Materials Research, National Bureau of Standards, Washington, D.C., (July 1977)

(86) P.A. Wycliffe, "Literature Search on High Conductivity Copper-Based Alloys," Final Report IDWA No. 6458-2, (March 1984)

(87) N. Fuschillo and M.L. Gimpi, "Electrical Conductivity and Tensile Strength of Dispersion-Strengthened Copper," J. Appl. Phys., Vol. 42, No. 13, (Dec. 1971), pp. 5513-5516

(88) Rocketdyne Material Properties Manual, 3rd Ed., (1977)

(89) Amax Copper Inc., Preliminary Data, "AMAX-MZC" (2 page leaflet, not dated)

(90) Amax Copper Inc., Interim Publication, "AMCROM"

(91) Glidcop Product Brochure, (March 1983)

(92) V.K. Sarin and N.J. Grant, "the Effect of TMTs on PM Cu-Zr and Cu-Zr-Cr Alloys," Powder Metal. Inst., Vol. 11, No. 4, (1979) p. 153

(93) J.D. Verhoeven, "*In Situ* Composites Prepared by Solidification and Mechanical Techniques", In Situ Composites IV, F.D. Lemkey, H.E. Cline, and M. McLean, Eds., Elsevier Science Publishing Co., Inc., (1982), pp. 267-276

(94) J.P. Harbison and J. Bevk, "Superconducting and Mechanical Properties of *In Situ* Formed Multifilamentary Cu-Nb_3Sn Composites", J. Appl. Physics, Vol. 48, No. 12, (Dec. 1977), pp. 5180-5187

(95) C.R. Spencer, E. Adam, E. Gregory, W. Marancik, and C.Z. Rosen, "Production of Nb_3Sn by the *In Situ* Process", IEEE Transactions on Magnetics, Vol. MAG-17, No. 1, (Jan. 1981), pp. 257-260

(96) J. Bevk, J.P. Harbison, and J.L. Bell, "Anomolous Increase in Strength of *In Situ* Formed Cu-Nb Multifilamentary Composites", J. Appl. Phys., Vol. 49, No. 12, (Dec. 1978), pp. 6031-6038

(97) W.A. Spitzig, A.R. Pelton, and F.C. Laabs, "Characterization of the Strength and Microstructure of Heavily Cold Worked Cu-Nb Composites", Submitted to Acta Metall., 10/88

(98) W.A. Heinemann, "Rapid Solidification - Process Technology for New Materials and Products," Rapidly Quenched Metals, S. Steeb and H. Warlimont, Eds., Elsevier Science Publishers, B.V., (1985), pp. 27-34

(99) A. Lawley, "Atomization of Specialty Alloy Powder," J. of Metals, Vol. 38, (Aug 1986), p. 15

(100) S.M.L. Sastry, T.C. Peng, P.J. Meschter, and J.E. O'Neal, "Rapid Solidification Processing of Titanium Alloys," J. of Metals, Vol. 35, (Sept. 1983), p. 21

(101) J.M. Wentzell, "Metal Powder Production by Vacuum Atomization," J. Vac. Sci. and Tech., Vol. 11, (1974), p. 1035

(102) B.H. Kear, J. Mayer, J.M. Poate, and P.R. Strutt, "Surface Treatments Using Laser, Electron, and Ion Beam Processing Methods", Metallurgical Treatises, J.K. Tien and J.F. Elliott, Eds., TMS/AIME, Warrendale , PA, (1981), pp 321-343

(103) R.E. Anderson, A.R. Cox, T.D. Tillman, and E.C. Van Reuth, "Use of RSR Alloys for High Performance Turbine Foils," Rapid Solidification Processing: Principles and Technologies II, R. Mehrabain, B.H. Kear, and M. Cohen, Eds., Claitor's Publishing Div., Baton Rouge, LA, (1980), p. 273

(104) R.V. Raman, A.N. Patel, And R.S. Carbonara, "Rapidly Solidified Powders Produced by a New Atomization Process," Progress in Powder Met., Vol. 38, (1982), p. 99

(105) C. Gelingas, R. Angers, and S. Pelletier, "Production of Metal Powder from Rapidly Solidified Ductile Ribbons," Matls. Let., Vol. 6, No. 10, (June 1988), pp. 359-361

(106) R.E Maringer and C.E. Mobley, "Casting of Metallic Filaments and Fibers," J. Vac. Sci and Tech., Vol. 11, (1974), p. 1067

(107) M.R. Jackson, J.R. Rairden, J.S. Smith, and R.W. Smith, "Production of Metallurgical Structures by Rapid Solidification Plasma Deposition," J. of Met., Vol. 33, (1981), p. 23

(108) S.J. Savage and F.H. Froes, "Production of Rapidly Solidified Metals and Alloys," J. of Metals, Vol. 36, (April 1984), p. 20

(109) V. Anared, A.J. Kaufman, and N.J. Grant, "Rapid Solidification of Modified 7075 Aluminum Alloy by Ultrasonic Gas Atomization," Rapid Solidification Processing: Principles and Technologies II, R. Mehrabain, B.H. Kear, and M. Cohen, Eds., Claitor's Publishing Div., Baton Rouge, LA, (1980), p. 273

(110) G. Rai, E. Lavernia, and N.J. Grant, "Powder Size Distribution in Ultrasonic Gas Atomization," J. of Met., Vol. 35, (Aug. 1985), p. 21

(111) A. Lawley, "An Overview of Powder Atomization Processes and Fundamentals," Int. J. of Powder Met., Vol. 13, (1977), p. 169

(112) J.K. Beddon, The Production of Metal Powders, Heydon and Sons Pub., London, U.K., (1978)

(113) Powder Metallurgy, Volume 7, Metals Handbook, 9th Edition, ASM International, Metals Park, OH, (1988)

(114) G. Friedman, "Production of Titanium Powder by the Rotating Electrode Process," Advanced Fabrication Techniques in Powder Metallurgy and Their Economic Implications, AGARD Conf. Proc. No. 200, (1976), Paper P.1.

(115) P.R. Holiday, A.R. Cox, and R.J. Peterson, "Rapid Solidification Effects on Alloy Structures," Rapid Solidification Processing: Principles and Technologies II, R. Mehrabain, B.H. Kear, and M. Cohen, Eds., Claitor's Publishing Div., Baton Rouge, LA, (1980), p. 246

(116) A.R.E. Singer, A.D. Roche, and L. Day, "Atomization of Liquid Metals Using Twin Roller Technique," Powder Met., Vol. 23, (1980), p. 81

(117) H. Ishii, M. Naka, and T. Masumoto, "Amorphous Metallic Powder Prepared by Roller Atomization," Rapidly Quenched Metals IV, T. Masumoto and K. Suzuki, Eds., The Japan Institute for Metals, Sendai, Japan, (1982), p. 33

(118) J. Perel, J.F. Mahoney, B.E. Kaleusher, and R. Mehrabain, "Electrohydodynamic Techniques in Metals Processing," Advances in Metals Processing, J.J. Burke, R. Mehrabain, and V. Weiss, Eds., Plenum Pub. Co., New York, NY, (1981), p. 79

(119) S.F. Cogan, J.E. Rockwell, F.H. Cocks, and M.L. Shepard, "Preparation of Metallic and Intermetallic Powders by Spark Erosion," J. Phys. E.: Sci. Instrum., Vol. 11, (1978), p. 174

(120) R.W. Jech, T.J. Moore, T.K. Glasgow, and N.W. Orth, "Rapid Solidification Via Melt Spinning: Equipment and Techniques," J. of Met., Vol. 36, (April 1984), p. 41

(121) R.B. Pond, R.E. Maringer, and C.E. Mobley, "High Rate Continuous Casting of Metallic Fibers and Filaments," New Trends in Materials Fabrication, ASM Seminar Series, ASM International, Metals Park, OH, (1976), p. 128

(122) P.G. Boswell, and G.A. Chadwick, "A Casting Device for Producing Rapidly Solidified Metallic Strips," J. Phys. E.: Sci. Instrum., Vol. 9, (1976), p. 523

(123) S. Chaklanobis and D.C. Agrawal, "Effect of Process Parameters on the Dimensions of Ribbons Melt Spunb Usinge Slotted Nozzles," J. of Matls. Sci Let., Vol. 5, (1986), pp. 10-12

(124) H.J. Güntherodt, "Introduction to Rapidly Solidified Materials," Rapidly Quenched Metals, S. Steeb and H. Warlimont, Eds., Elsevier Science Publishers, B.V. (1985), pp. 1591-1598

(125) R.E Maringer and C.E. Mobley, "Advances in Melt Extraction," Rapidly Quenched Metals III, Vol. I, B. Cantor, Ed., The Metals Society, London, U.K., (1978), p. 49

(126) L.E. Hackmann and T. Gaspar, "Producing Strip by Melt Overflow Process," Industrial Heating, (Jan. 1986), p. 36

(127) J. Hubert, F. Mollard, and B. Lux, "Manufacture of Metallic Fibers and Wires by the Melt Spin and Melt Drag Process," Z. Metallk., Vol. 64, (1973), p. 835

(128) R.E. Maringer, C.E. Mobley, and E.W. Collings, "An Experimental Method for the Production of Rapidly Quenched Filaments and Fibers," Rapidly Quenched Metals, N.J. Grant and B.C. Giessen, Eds., M.I. T. Press, Cambridge, Mass., (1976), p. 29

(129) I. Ohnaka, T. Fukusako, T. Ahmichi, T. Masumoto, A. Inoue, and M. Hagiwara, "Production of Amorphous Filaments by In-Rotating-Liquid-Spinning," Rapidly Quenched Metals IV, T. Masumoto and K. Suzuki, Eds., The Japan Institute of Metals, Sendai, Japan, (1982), p. 31

(130) T. Masumoto, I. Ohnaka, A. Inoue, and M. Hagiwara, "Production of Pd-Cu-Si Amorphous Wires by Melt Spinning Method Using Rotating Water," Scripta Met., Vol. 15, (1981), p. 293

(131) P. Piethowsky, "Novel Mechanical Device for Producing Rapidly Cooled Metals and Alloys of Uniform Thickness," Appl. Phys. Letters, Vol. 34, (1963), p. 445

(132) R.W. Cahn, K.D. Krishnanand, M. Laridjani, M. Greenholtz, and R. Hill, "Novel Splat Quenching Techniques and Methods for Assessing Their Performance," Mater. Sci. Eng., Vol. 23, (1976), p. 83

(133) H. Jones, "Some Developments in Techniques for Rapid Solidification," Processing of Structural Metals by Rapid Solidification, F.H. Froes and S.J. Savage, Eds., ASM International, Metals Park, OH, (Oct. 1986), pp. 77-93

(134) M.C. Flemings, "Segregationa dn Structure in Rapidly Solidified Cast Materials", Metallurgical Treatises, J.K. Tien and J.F. Elliott, Eds., TMS/AIME, Warrendale , PA, (1981), pp 291-300

(135) R.D. McIntyre, Mater. Eng., Vol. 94, (1981), p. 42

(136) E.A. Starke Jr., T.H. Sanders Jr., and I.G. Palmer, J. Metals, (1981) p. 24

(137) J.R. Pickens and E.A. Starke Jr., Advances in Powder Technology, G.Y. Chin Ed., ASM, (1981), p. 150

(138) K.K. Sankara, J.E. Oneal, and S.M.L. Sastry, Met. Trans. 14A, (1983), p. 2174

(139) A.I. Taub, "Mechanical Properties and Potential Applications of Rapidly Solidified Alloys," Rapidly Quenched Metals, S. Steeb and H. Warlimont Eds., Elsevier Science Publishers, B.V., (1985), pp. 1611-1618

(140) S.H. Lo , W.M. Gibbon, and R.S. Hollingshead, "Consolidation of Rapidly Solidified Cu-Ni Powders", Materials Sci. and Eng., Vol. 98, (1988), pp. 411-414

(141) G.H. Geiger and D.R. Poirier, Transport Phenomena in Metallurgy, Addison-Wesley Publishing Company, Reading Massachussetts, (1973), p. 191

(142) M.C.I. Siu, W.L. Carroll, and T.W. Watson, "Thermal Conductivity and Electrical Resistivity of Six Copper-Base Alloys", NBSIR 76-1003, (March 1976)

(143) D. Halliday and R. Resnick, Physics, Part 2, J. Wiley and Sons, New York, NY, (1960), pp. 682-687

(144) A. Matthiessen and C. Vogt, Ann. Phys. Leibz., Vol. 122, (1864), p. 19

(145) J. Bass, Advances in Physics, 21, (1972), p. 431

(146) E.R. Andrews, Proc. Phys. Soc., A 62, (1949), p. 77

(147) J.W. Rutter and J. Reekie, Phys. Rev., Vol. 78, (1950), p. 70

(148) C.H. Johannsson and J.O. Linde, Ann. Phys., 25, (1936), p. 1

(149) N.F. Mott and H. Jones, The Theory of the Properties of Metals and Alloys, Dover Public, NY, (1958)

(150) K. Schroder, "Experimental Aspects of Electrical and Thermal Properties of Metals", High Conductivity Copper and Aluminum Alloys, E. Ling and P.W. Taubenblat, Eds., TMS/AIME, Warrendale, PA, (1984), pp. 1-17

(151) D.D. Pollock, Electrical Conduction in Solids: An Introduction, ASM International, Metals Park, OH, (1985). pp. 121-172

(152) F. Bloch, Z. Physik, Vol. 52, (1928), p. 555

(153) F. Bloch, Z. Physik, Vol. 59, (1930), p. 208

(154) E. Grüneisen, Ann. Physik, Vol. 16, (1933), p. 530

(155) M. Kohler, Z. Physik, Vol. 124, (1948), p. 772

(156) M. Kohler, Z. Physik, Vol. 125, (1949), p. 679

(157) E.H. Sondheimer, Proc. Royal Soc. A, Vol. 203, (1950), p. 75

(158) J.M. Ziman, Electrons and Phonons, Clarendon, Oxford, U.K., (1960)

(159) G. Grimvall, Thermophysical Properties of Materials, North Holland Physics Publishing, Amsterdam, The Netherlands, (1986), p. 224

(160) S. Nishikawa, K. Nagata, and S. Kobayashi, "Reversion Phenomena of Cu-Cr Alloys", Nippon Kinzoka Gakkaishi, Vol. 30, No. 8, (1966) pp. 760-765. NASA Technical Translation TM-77780.

(161) H. Suzuki, H. Kitano, and M. Kanno, "On Reversion Phenomena in Cu Cr-Zr Alloys", Nippon Kinzoka Gakkaishi, Vol. 33, No. 3, 1969, pp. 334-338. NASA Technical Translation TM-77791.

(162) Smithells Metals Reference Book, Sixth Edition, "14.4 The Physical Properties of Cu and Cu Alloys," E.A. Brandes, Ed., Butterworths, London, (1983), pp. 14-16 to 14-17

(163) Supercon Inc., "CuNb Microcomposite Conductor," (Undated 2 page brochure)

(164) Smithells Metals Reference Book, Sixth Edition, "14.8 The Physical Properties of Steels," E.A. Brandes, Ed., Butterworths, London, (1983), pp. 14-23 to 14-39

(165) N. Orth, I. Locci, and M. Hebsur, personal communications

(166) T. Bloom, Ph.D. Dissertation, Illinois Institute of Technology, to be published

(167) C. Zener, Trans. Am. Inst. Min. Eng., Vol. 175, (1948), p. 47

(168) J.I. Goldstein, Introduction to Electron Microscopy, J.J. Hren, J.I. Goldstein, and D.C. Joy, Eds., Plenum, NY, (1979)

(169) R.E. Reed-Hill, Physical Metallurgy Principles, Second Edition, D. Van Nostrand Co., (1973), p. 255

(170) M.J. Tenwick and H.A. Davies, "The Mechanism of Ribbon Formation in Melt-Spun Copper and Copper-Zirconium," Rapidly Quenched Metals, S. Steeb abd H. Warlimont, Eds., Elsevier Publishers, B.V., (1985), pp. 67-70

(171) Smithells Metals Reference Book, Sixth Edition, "14.2 The Physical Properties of Liquid Metals," E.A. Brandes, Ed., Butterworths, London, (1983), p. 14-7

(172) M. Hansen, Constitution of Binary Alloys, 2nd Ed., McGraw-Hill, New York, (1958)

(173) Elements of X-ray Diffraction, Second Edition, B.D. Cullity, Addison-Wesley, Reading, Mass., (1978), p. 376

(174) Smithells Metals Reference Book, Sixth Edition, "4.5.1 Atomic and Ionic Radii," E.A. Brandes, Ed., Butterworths, London, (1983), pp. 4-25 to 4-27

(175) H. Suzuki and M. Kanno, "The T-T-T Curve in Cu-Cr Alloy," Nippon Kinzuki Gakkaishi, Vol. 35, No. 5, (1981), pp. 434-439. NASA Technical Translation TT-20167.

9 Symbols List

A	Aspect ratio
$\alpha_{tr}F(\omega)$	Transport electron-phonon coupling function
B	Complex parameter for stacking fault energy strengthening dependent on $\Delta\sigma$, T, and r_s
b	Burgers vector
ΔC_B	Solute concentration gradient between two precipitates
C	Velocity of sound in the metal
C_B	Average Concentration of B in the matrix
$C_{V,el}$	Electronic heat capacity
c_x	Concentration of element x
c_1	Constant specific to a metal
c_2	Constant specific to a metal
D_B	Diffusivity of solute in the matrix
D_{Cr}	Diffusivity of Cr in solid Cu
D_{Nb}	Diffusivity of Nb in solid Cu
$\bar{D}_x$	Average diffusivity of element x in solid Cu during melt spinning
ϵ	Misfit parameter between matrix and precipitate
η	Draw ratio
η_F	Fermi energy of the metal
f	Volume fraction of the precipitates
F	Obstacle strength
ΔG	Difference between the matrix and precipitate shear modulus
G_M	Shear modulus of the matrix
γ_{CS}	Interfacial energy Surface energy

h	Long axis radius of an elliptical precipitate Planck's constant
$\hbar Cq$	Long-wavelength phonon energy
$\hbar$	$\frac{h}{2\pi}$
I	Current
J_5	Debye integral of order 5
k	Constant for coherency strengthening dependent on averaging technique
k_B	Boltzmann's constant
κ_B	Boltzmann's constant
L	Effective particle spacing Friedel spacing
L_S	Spacing between particles
l	Mean free path Distance between probes for four point resistance measurements
m_e	Mass of an electron
μ_P	Difference in chemical potential near a precipitate and in the bulk alloy
n_e	Number of free electrons per cm^3
n_s	Number of precipitates per unit area in the glide plane
N_S	Total number of particles in the system
N_{S1}	Number of type 1 particles
N_{S2}	Number of type 2 particles
ν	Poisson's ratio
ω	Angular velocity
ϕ	Angle between dislocation and force acting on dislocation at a precipitate
σ	Electrical conductivity
ϕ_C	Critical angle for a dislocation in equilibrium with a precipitate

q	Phonon wave number
q_D	Debye phonon wave number
R	Radius of curvature Resistance
$\overline{R}$	Average radius of curvature for grains
r	Short axis radius of an elliptical precipitate
r_o	Inner cutoff radius of a dislocation, normally taken to be equal to b
r_s	Average planar particle radius in dislocation glide plane
ρ	Electrical resistivity
ρ_{BG}	Electrical resistivity calculated from Bloch-Grüneisen Formula
ρ_I	Residual resistivity
ρ_L	Electron-phonon resistivity
ρ_x	Resistivity of phase x
σ	Yield strength of the material
σ_{APB}	Antiphase boundary energy
σ_{APB}	Thermal conductivity
$\Delta\sigma$	Difference in stacking fault energies of the precipitate and matrix
T	Temperature Absolute temperature Dislocation line tension
t	Time Thickness of sample in four point resistance measurements
τ	Flow stress necessary to overcome an obstacle
τ_{AO}	Flow stress for Ashby-Orowan model
τ_{APB}	Flow stress for antiphase boundary strengthening
τ_{CoS}	Flow stress for coherency strengthening
τ_{CS}	Flow stress for chemical strengthening
τ_G	Flow stress for modulus strengthening

τ_O	Flow stress for Orowan strengthening
τ_{SF}	Flow stress for stacking fault energy strengthening
θ_D	Debye temperature of a material
V	Volume of precipitate Voltage drop Atomic volume
$\overline{V}$	Average velocity of component transferring heat
$\overline{V}_F$	Average velocity of the electrons in a metal
V_f	Volume fraction of precipitates
w	Width of sample in four point resistance measurements
x	Mean planar intercept diameter of the precipitates
X_B	Equilibrium concentration of B in β for β in equilibrium with α
X_x	Volume fraction of phase x
X_1	Number fraction of type 1 particles
X_2	Number fraction of type 2 particles
ΔX	Concentration difference between the alloy and the equilibrium solubility of B in α
ξ	Angle between Burgers vector and the direction of the dislocation line tension
z	Distance from glide plane of dislocation to center of precipitate

National Aeronautics and Space Administration

Report Documentation Page

1. Report No. NASA CR-185144	2. Government Accession No.	3. Recipient's Catalog No.

4. Title and Subtitle

Precipitation Strengthened High Strength, High Conductivity
Cu-Cr-Nb Alloys Produced by Chill Block Melt Spinning

5. Report Date

September 1989

6. Performing Organization Code

7. Author(s)

David L. Ellis and Gary M. Michal

8. Performing Organization Report No.

None

10. Work Unit No.

553-13-00

9. Performing Organization Name and Address

Case Western Reserve University
Department of Materials Science and Engineering
Cleveland, Ohio 44106

11. Contract or Grant No.

NGT-50087

13. Type of Report and Period Covered

Contractor Report
Final

12. Sponsoring Agency Name and Address

National Aeronautics and Space Administration
Lewis Research Center
Cleveland, Ohio 44135-3191

14. Sponsoring Agency Code

15. Supplementary Notes

Project Manager, Robert L. Dreshfield, Materials Division, NASA Lewis Research Center. This report was a thesis submitted by David L. Ellis in partial fulfillment of the requirements for the Degree of Doctor of Philosophy to Case Western Reserve University in August 1989.

16. Abstract

There are many potential applications for materials that possess a combination of high strength, high conductivity, and good long term stability at elevated temperatures. In an effort to achieve this combination of properties a series of Cu-based alloys containing 2 to 10 a/o Cr and 1 to 5 a/o Nb were produced by chill block melt spinning (CBMS). The melt spun ribbons were consolidated and hot rolled to sheet for testing. The desire was to produce a supersaturated Cu-Cr-Nb solid solution from which the high melting point intermetallic compound Cr_2Nb could be preferentially precipitated to precipitation strengthen the Cu matrix. By using the intermetallic phase, it was hoped that the precipitates would not coarsen readily and lose their strength as with Cu-Cr alloys do when exposed to elevated temperatures, particularly above 500 °C. The results show that the materials possess electrical conductivities in excess of 90 percent that of pure Cu at 200 °C and above. This implies that the thermal conductivities of these alloys are near that of pure Cu at temperatures above 200 °C. The strengths of the Cu-Cr-Nb alloys were much greater than Cu, Cu-0.6 Cr, NARloy-A, and NARloy-Z in the as-melt spun condition. The strengths of the consolidated materials were less than Cu-Cr and Cu-Cr-Zr below 500 °C and 600 °C respectively, but were significantly better above these temperatures. The strengths of the consolidated materials were greater than conventional wrought NARloy-Z, the material currently used in rocket nozzles, at all temperatures. GLIDCOP possessed similar strength levels up to 750 °C when the strength of the Cu-Cr-Nb alloys begins to degrade. The long term stability of the Cu-Cr-Nb alloys was measured by the microhardness of aged samples and the growth of precipitates. The microhardness measurements indicate that the alloys overage rapidly, but do not suffer much loss in strength between 10 and 100 hours which confirms the results of the electrical resistivity measurements taken during the aging of the alloys at 500 °C. The loss in strength from peak strength levels is significant, but the strength remains exceptionally good. TEM of the as-melt spun samples revealed that the Cr_2Nb precipitates formed in the liquid Cu during the chill block melt spinning, indicating a very strong driving force for the formation of the precipitates. TEM of the aged and consolidated materials indicates that the precipitates do coarsen considerably, but remain in the submicron size range.

17. Key Words (Suggested by Author(s)) Copper-based alloys; Rapid solidification; Thermal conductivity; Electrical resistivity; Mechanical properties	18. Distribution Statement Unclassified – Unlimited Subject Category 26

19. Security Classif. (of this report)	20. Security Classif. (of this page)	21. No of pages	22. Price*
Unclassified	Unclassified	230	A11

NASA FORM 1626 OCT 86

*For sale by the National Technical Information Service, Springfield, Virginia 22161